

A Phenomenological Causal-Response Model for Galactic Rotation Curves with Global Parameters

Jonathan Washburn,¹ Anil Thapa,¹ Megan Simons,¹ and Elshad Allakhyarov^{1, 2, 3, 4, *}

¹*Recognition Science Institute, Austin, Texas, USA*

²*Institut für Theoretische Physik II: Weiche Materie, Heinrich-Heine Universität Düsseldorf, Universitätstrasse 1, 40225 Düsseldorf, Germany*

³*Theoretical Department, Joint Institute for High Temperatures, Russian Academy of Sciences (IVTAN), 13/19 Izhorskaya street, Moscow 125412, Russia*

⁴*Department of Physics, Case Western Reserve University, Cleveland, Ohio 44106-7202, United States*

(Dated: December 29, 2025)

We present a phenomenological model for galactic rotation curves based on a causal linear-response modification of Newtonian gravity. The effective centripetal acceleration is parameterized as $a_{\text{eff}}(r) = w(r) a_{\text{baryon}}(r)$, where $w(r)$ is the steady-state (low-frequency) gain of a retarded response kernel with characteristic timescale $\tau_* \approx 133$ Myr. We use the global form $w(r) = \xi n(r) (a_0/a_{\text{baryon}})^\alpha \zeta(r)$, where ξ captures morphology dependence (via gas fraction), $n(r)$ describes radial structure, and $\zeta(r)$ provides a mild geometric taper. All seven global parameters ($\alpha, a_0, C_\xi, A, r_0, p, \Upsilon_*$) are fitted simultaneously under a strict global-only protocol (zero per-galaxy tuning of stellar M/L , distance, or inclination), making the framework falsifiable. Applied to the high-quality ($Q = 1$) SPARC subset of 99 galaxies, the model achieves median $\chi^2/N = 1.19$ and RMS velocity residual 17.3 km/s, compared to a global-only MOND baseline with median $\chi^2/N = 1.79$ and RMS residual 21.5 km/s. The model reproduces the radial acceleration relation and baryonic Tully–Fisher relation as emergent scaling laws, predicts systematically larger enhancements in dwarfs, and eliminates the residual trend with gas fraction. As an external test, the same dynamical-time scaling predicts enhanced galaxy-cluster weak-lensing convergence $\kappa/\kappa_{\text{GR}} \approx 1.8 \pm 0.3$ at projected radii $R = 20\text{--}50$ kpc, testable with upcoming surveys (e.g., Euclid). We also discuss how scale-free latency/fractional-memory considerations motivate the adopted power-law dependence of the slow-response enhancement.

CONTENTS

I. Introduction	3
II. Theoretical Framework	4
2.1. Causal linear-response framework	5
2.2. Phenomenological ansatz and weight function	6
2.3. Physical motivation: scale-free latency mechanism	7
2.4. Comparison baseline: Modified Newtonian Dynamics (MOND)	8
III. The Causal-Response Model	10
3.1. Weight function decomposition	10
3.2. Complexity factor ξ	11
3.3. Spatial profile $n(r)$	11
3.4. Geometric correction $\zeta(r)$	13
3.5. Global parameter summary	14
IV. Methods	15
4.1. SPARC dataset and galaxy classification	15
4.2. Error model and observational uncertainties	16
4.3. Goodness-of-fit metric	17
4.4. Parameter optimization and fitting procedure	18
4.5. MOND baseline comparison methodology	19
4.6. Galaxy cluster weak lensing: physical basis and predictions	20

* elshad.allakhyarov@case.edu

V. Results	21
5.1. Global performance metrics and model comparison	22
5.2. Rotation curve fits and weight function visualization	22
5.3. Empirical scaling relations: RAR and BTFR	23
5.4. Morphology dependence: dwarfs vs. spirals	26
5.5. Residual analysis and error model validation	27
5.6. Outlier analysis and model limitations	28
VI. Discussion	30
6.1. Physical interpretation of the response weight $w(r)$	30
6.2. Relation to MOND	31
6.3. Comparison to MOND variants and alternative theories	32
6.4. Comparison to empirical dark matter profiles	33
6.5. Caveats and alternative framings	34
6.6. Quantitative falsification criteria	34
6.7. Limitations and future work	35
6.8. Comparison with Literature Values	36
VII. Conclusion	36
Acknowledgments	38
Data Availability	38
A. Action-based conservative realization (Caldeira-Leggett construction)	39
1. Theoretical predictions	39
2. Validation tests	39
3. Reproducibility	40
B. Parameter Sensitivity Analysis	40
Error-model hyperparameters	40
C. Derivation of Observational Predictions	41
1. Cluster weak lensing: convergence ratio derivation	41
D. Robustness to Data Quality (Q1+Q2)	42
References	47

TABLE I. Comparison of major gravity theories addressing galactic rotation curves. “Params/gal” denotes typical per-galaxy fit parameters in rotation-curve practice (not fundamental constants). “GR limit” indicates whether general relativity is recovered in appropriate limits.

Theory	Params/gal	GR limit	Rotation curves	Clusters	Cosmology
Λ CDM (NFW)	3–5	Yes	Good (tuned)	Good	Excellent
MOND	1–3	No	Excellent	Poor	Requires extension
TeVeS	1–3	Yes	Excellent	Poor	Marginal
$f(R)$ gravity	1–3	Yes (weak)	Poor	Marginal	Good
Massive gravity	1–3	Yes (weak)	Poor	Marginal	Good
Verlinde (2017)	1–2	Yes	Poor	Poor	Marginal
Causal response (this work)	0	Yes	Good	Untested	Untested

ORCID J.W. 0009-0001-8868-7497 ; A.T. [TBD] ; M.S. [TBD] ; E.A. 0000-0001-7212-4713

I. INTRODUCTION

Galaxy rotation curves have challenged our understanding of gravity for over four decades [1, 2]. Across a wide range of disk galaxies, the observed orbital speed $v(r)$ remains approximately flat or slowly rising with radius, in tension with the Keplerian decline $v \propto r^{-1/2}$ expected from Newtonian gravity sourced only by the observed baryons. This “mass discrepancy” is not isolated to rotation curves: related anomalies appear in galaxy clusters [3], in weak and strong gravitational lensing [4], and in the growth of large-scale structure [5]. Taken together, these observations indicate that the gravitational field inferred from dynamics and lensing is stronger than what visible matter alone predicts.

The prevailing Λ CDM paradigm postulates that most matter is cold, collisionless dark matter (CDM) interacting only gravitationally [6]. This framework succeeds on cosmological scales (e.g., CMB anisotropies and large-scale structure), and N-body simulations predict dark matter halos with approximately universal density profiles, notably the Navarro–Frenk–White (NFW) form [7]:

$$\rho_{\text{NFW}}(r) = \frac{\rho_s}{(r/r_s)(1+r/r_s)^2} \quad (1)$$

characterized by two free parameters per galaxy: the scale density ρ_s and scale radius r_s , where r is the radial distance from the galactic center. When fitting rotation curves, Λ CDM typically requires 3–5 parameters per galaxy: two halo parameters (ρ_s, r_s) plus 1–2 stellar mass-to-light ratios M/L (disk and sometimes bulge), and occasionally distance/inclination adjustments.

Despite these successes, CDM faces persistent small-scale tensions: the Cusp-core problem [8, 9], Missing satellites [10, 11], Too-big-to-fail [12], and the Diversity problem [13, 14]. Furthermore, the tight correlation between observed and baryonic acceleration (Radial Acceleration Relation, RAR) [15] suggests a direct link between baryons and dynamics, unexpected if dark matter dominates. Finally, despite decades of searches, no dark matter particle has been detected [6, 16].

Faced with CDM’s small-scale challenges, numerous modified-gravity frameworks have been proposed. Modified Newtonian Dynamics (MOND) [17] introduces a characteristic acceleration scale $a_0 \approx 1.2 \times 10^{-10} \text{ m s}^{-2}$ below which the effective force law departs from Newtonian behavior. MOND fits many galaxy rotation curves with remarkable economy [15, 18, 19] and naturally connects to the BTFR and the radial acceleration relation (RAR). However, practical rotation-curve fitting typically still involves per-galaxy nuisance freedom (e.g., stellar M/L for disk/bulge and sometimes distance/inclination adjustments), and MOND faces well-known difficulties with galaxy clusters and lensing without additional dark components [4, 63]. Relativistic and cosmological completions exist in various forms (e.g., TeVeS [20], $f(R)$ gravity [21], scalar–tensor theories [22], massive gravity [23], and emergent-gravity proposals [24, 25]), but these often introduce added complexity and/or confront growth and lensing constraints.

Spiral density waves and arm-crossing “streaming motions” can perturb line-of-sight velocities by $\sim 10\text{--}30 \text{ km/s}$ and imprint small-scale wiggles in $v(r)$ [8, 9, 15, 26]. However, such effects are azimuthally alternating and average to near zero over an orbit, so they cannot supply a net centripetal boost. The discrepancy persists in galaxies with weak or absent spiral structure (e.g., LSB galaxies, dwarfs, irregulars) and appears independently in lensing and dispersion-based inferences. Consequently, spiral streaming is best treated as a modest measurement/systematics contribution rather than the origin of the global mass discrepancy.

For orientation, Table I summarizes (at a coarse level) how several major approaches address rotation curves, clusters, and cosmology, and how much per-galaxy tuning is typically used in practice.

In this work, we propose a phenomenological *causal-response* model in which the effective gravitational acceleration is parameterized as $a_{\text{eff}}(r) = w(r) a_{\text{baryon}}(r)$. The key hypothesis is that the steady-state enhancement $w(r)$ is controlled primarily by local dynamical time and morphology, and can be described by a *single* functional form shared by all galaxies. Operationally, this is enforced by a strict global-only protocol: all seven parameters are fit once for the entire catalog with zero per-galaxy tuning. Empirically, the resulting $w(r)$ is larger in systems with longer dynamical times (typically dwarfs) and closer to unity in fast/compact systems (typically massive spirals), producing the familiar “dwarf enhancement” often attributed to dark matter dominance in low-mass galaxies.

The phrase “slow rotation” should be interpreted carefully. Through the BTFR [26–29], smaller characteristic velocities generally imply much smaller baryonic masses (roughly $M_b \propto V^4$), so “slow rotators” are typically dwarf systems. Observationally, inclination uncertainties can make a face-on spiral appear to rotate slowly, and dwarfs often have rising rotation curves that do not reach a clean flat regime, so measured V can understate V_{max} . In addition, gas turbulence and asymmetric drift are comparatively more important in dwarfs, making rotation a noisier proxy for mass. In this paper we therefore use explicit kinematic thresholds (Sec. IV 4.1) when referring to dwarfs versus spirals.

The key distinction of our framework is this global-only constraint: each galaxy is an independent test of the same global functional form, which makes the model falsifiable and reduces the risk of overfitting relative to per-galaxy halo tuning. We implement the modification via a retarded linear-response kernel with a characteristic memory timescale $\tau_* \approx 133$ Myr (Sec. II 2.1), chosen to recover Newtonian/GR behavior in fast-dynamics limits while allowing enhancement in slow-dynamics regimes.

We validate the model on the high-quality $Q = 1$ subset of the SPARC catalog [26] ($N = 99$ galaxies) using a fixed error model and masking protocol applied identically to a global-only MOND baseline (Sec. IV). On this subset, the causal-response model achieves median $\chi^2/N = 1.19$ versus 1.79 for MOND under the same global-only constraints, and reduces the RMS velocity residual (17.3 vs. 21.5 km/s). The model also reproduces the RAR and BTFR as emergent relations and removes the residual trend with gas fraction found in the MOND baseline (Sec. V). We further report robustness tests on the combined $Q = 1 + Q = 2$ dataset ($N = 163$; Appendix D).

An external falsification opportunity comes from galaxy-cluster weak gravitational lensing, which probes long-dynamical-time environments distinct from galactic disks. Extrapolating the same dynamical-time dependence to cluster cores, the model predicts an enhanced convergence ratio $\kappa/\kappa_{\text{GR}} \approx 1.8 \pm 0.3$ at projected radii $R = 20$ –50 kpc (Sec. IV 4.6). This prediction is distinct from baryons-only GR ($\kappa/\kappa_{\text{GR}} \approx 1$) and from standard MOND expectations in clusters without additional dark components. Upcoming survey data (including Euclid-era cluster lensing measurements) can therefore provide a sharp empirical check of the framework.

A key theoretical motivation addressed in this work is why a *power-law* slow-response enhancement is a natural phenomenological target. If the underlying microphysics exhibits scale-free latency (no characteristic waiting-time scale in the slow regime), then the low-frequency gain generically scales as a power law, $|H(i\omega) - 1| \propto |\omega|^{-\alpha}$, as in fractional-memory/backlog models [30–32]. For quasi-steady galactic dynamics with characteristic orbital frequency $\omega \sim v/r$, this motivates a steady-state scaling $w(r) - 1 \propto r^\alpha$ (approximately for flat rotation curves), matching the empirical dependence used in our global fit (Sec. II 2.3).

The paper is organized as follows. Section II introduces the theoretical framework and the causal linear-response formulation, including the latency-to-power-law mechanism. Section III specifies the full weight function $w(r)$ and its global-parameter structure. Section IV describes the SPARC dataset, error models, goodness-of-fit metrics, parameter optimization, and the cluster weak lensing prediction framework. Section V presents the main empirical results, including rotation-curve fits, scaling relations (RAR, BTFR, dwarf/spiral enhancement), residual diagnostics, and outlier analysis for both the $Q = 1$ and $Q = 1 + Q = 2$ datasets. Section VI discusses physical interpretation, comparisons to MOND and alternative frameworks, and quantitative falsification criteria. Appendix A provides an explicit conservative (action-based) realization via the Caldeira-Leggett construction, Appendix B presents parameter sensitivity analysis, and Appendix D details the $Q = 1 + Q = 2$ robustness tests with full validation figures.

II. THEORETICAL FRAMEWORK

This section establishes the theoretical foundation for our causal-response model. We begin by presenting the core linear-response framework that governs how gravitational fields respond to baryonic matter with memory effects (Sec. 2.1). We then derive the phenomenological ansatz that will be applied to rotation curve data (Sec. 2.2), explain the physical motivation for the power-law form of the enhancement (Sec. 2.3), and conclude by establishing the MOND baseline used for comparison throughout this work (Sec. 2.4).

2.1. Causal linear-response framework

We model the gravitational response as a causal linear system in which the effective acceleration $a_{\text{eff}}(t, r)$ at time t and radius r depends not only on the instantaneous baryonic acceleration $a_{\text{baryon}}(t, r)$ but also on its history through a memory kernel. This is expressed via the standard linear-response integral:

$$a_{\text{eff}}(t, r) = a_{\text{baryon}}(t, r) + \int_{-\infty}^t \Gamma(t - t', r) a_{\text{baryon}}(t', r) dt' \quad (2)$$

where $\Gamma(\tau, r)$ is the memory kernel encoding how past accelerations contribute to the present response, with $\tau = t - t'$ being the time lag. Causality requires $\Gamma(\tau, r) = 0$ for $\tau < 0$, ensuring no future dependence.

a. Memory kernel and transfer function. We adopt an exponential memory kernel as a minimal single-timescale phenomenological parameterization:

$$\Gamma(\tau, r) = \frac{w(r) - 1}{\tau_*} e^{-\tau/\tau_*} \quad (3)$$

where τ_* is the characteristic memory timescale (determined below) and $w(r)$ is the steady-state (low-frequency) weight. This single-pole kernel has exponential decay, ensuring that distant past has diminishing influence, and the normalization factor $(w(r) - 1)/\tau_*$ enforces the correct steady-state limit.

Taking the Fourier transform of Eq. (2), we obtain the frequency-domain relation:

$$a_{\text{eff}}(\omega, r) = H(i\omega, r) a_{\text{baryon}}(\omega, r) \quad (4)$$

where the complex transfer function is:

$$H(i\omega, r) = 1 + \int_0^\infty \Gamma(\tau, r) e^{-i\omega\tau} d\tau = 1 + \frac{w(r) - 1}{1 + i\omega\tau_*} \quad (5)$$

This transfer function maps baryonic acceleration to effective acceleration in the frequency domain, with the unity term representing the instantaneous Newtonian response and the second term encoding the memory correction.

b. Response and quadrature components. Decomposing the transfer function into real and imaginary parts yields physical insight. The real (in-phase) component, called the response function, is:

$$C(\omega, r) \equiv \text{Re}[H(i\omega, r)] = 1 + \frac{w(r) - 1}{1 + \omega^2\tau_*^2} \quad (6)$$

This describes the conservative (energy-conserving) gravitational response. The effective acceleration in the frequency domain becomes:

$$a_{\text{eff}}(\omega, r) = C(\omega, r) a_{\text{baryon}}(\omega, r) \quad (7)$$

making explicit the frequency-dependent gain multiplying the baryonic acceleration.

The imaginary (quadrature) component, representing phase lag, is:

$$S(\omega, r) \equiv \text{Im}[H(i\omega, r)] = -(w(r) - 1) \frac{\omega\tau_*}{1 + \omega^2\tau_*^2} \quad (8)$$

This encodes a small phase-lag component that oscillates symmetrically in time for the single-pole kernel of Eq. (3). For circular orbits, this quadrature term contributes negligibly to the net radial force balance, averaging to zero over an orbital period.

c. Frequency limits and physical interpretation. The response function $C(\omega, r)$ exhibits two crucial limiting behaviors:

(i) Low-frequency limit ($\omega\tau_* \ll 1$, long dynamical times):

$$C(\omega, r) \rightarrow w(r)$$

The system approaches the steady-state response determined entirely by $w(r)$.

(ii) High-frequency limit ($\omega\tau_* \gg 1$, short dynamical times):

$$C(\omega, r) \rightarrow 1$$

The memory term vanishes and the response becomes instantaneous Newtonian. This ensures consistency with Solar System tests and laboratory gravity experiments where $T_{\text{dyn}} \ll \tau_*$.

Figure 1 illustrates both the time-domain memory kernel $\Gamma(\tau)$ and the frequency-domain transfer function components $C(\omega)$ and $S(\omega)$. The exponential decay with characteristic timescale $\tau_* \approx 133$ Myr ensures fast-limit recovery ($H \rightarrow 1$ as $\omega \rightarrow \infty$) while providing the necessary enhancement at low frequencies ($C(\omega) \rightarrow w$ as $\omega \rightarrow 0$).

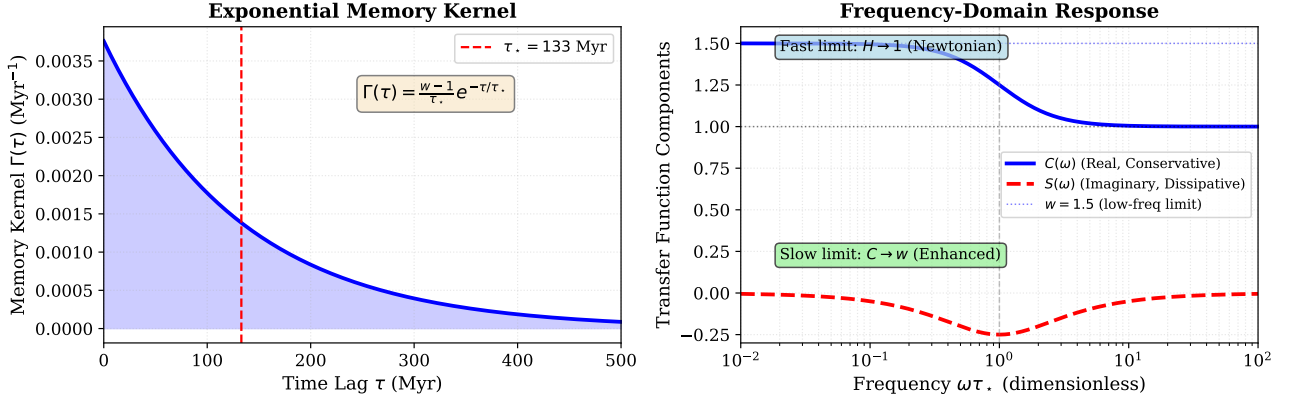


FIG. 1. Visualization of the memory kernel and transfer function. Left: Time-domain memory kernel $\Gamma(\tau) = (w-1)/\tau_* \cdot e^{-\tau/\tau_*}$ showing exponential decay with characteristic timescale $\tau_* = 133$ Myr. Right: Frequency-domain transfer function showing the real (conservative) component $C(\omega)$ and imaginary (dissipative) component $S(\omega)$. At low frequencies ($\omega\tau_* \ll 1$), the response approaches the steady-state weight w . At high frequencies ($\omega\tau_* \gg 1$), the response recovers the Newtonian limit ($H \rightarrow 1$).

d. Steady-state approximation for galactic systems. For quasi-steady circular orbits with angular frequency $\omega(r) \simeq v(r)/r$, galactic systems typically lie near the crossover $\omega\tau_* \sim \mathcal{O}(1)$ rather than in an extreme asymptotic limit. Typical orbital periods are $T_{\text{dyn}} \sim 100\text{--}300$ Myr, while $\tau_* \approx 133$ Myr, giving $\omega\tau_* \sim 0.5\text{--}1.5$ at most radii. As a working approximation for steady rotation-curve fitting, we therefore identify the effective gain with its slow-response limit,

$$C(\omega, r) \approx w(r) \quad (9)$$

and interpret $w(r)$ as the steady-state weight that enters the phenomenological ansatz (Sec. 2.2). Deviations from the strict $\omega\tau_* \rightarrow 0$ limit are treated as subleading corrections relative to the empirical variation of $w(r)$ across radii and morphologies.

2.2. Phenomenological ansatz and weight function

Taking the steady-state limit of Eq. (7) using Eq. (9), we obtain the phenomenological ansatz:

$$a_{\text{eff}}(r) = w(r) a_{\text{baryon}}(r) \quad (10)$$

where $w(r) = \lim_{\omega \rightarrow 0} C(\omega, r)$ is the steady-state weight function and $a_{\text{baryon}}(r)$ is the Newtonian acceleration computed from the observed baryonic mass distribution (stars + gas + dust).

Equation (10) describes a multiplicative modification to Newtonian gravity. In standard Newtonian dynamics, $w(r) = 1$ everywhere. Rotation curve observations require $w(r) > 1$, with the enhancement growing systematically with dynamical time $T_{\text{dyn}}(r) = 2\pi r/v(r)$. The empirical requirement $w(r) > 1$ (enhancement rather than suppression) corresponds to $C(\omega, r) > 1$, which requires either coupling to a reservoir where the system exchanges energy with external degrees of freedom, or new physics beyond the Newtonian limit (effective field theory at galactic scales). The Caldeira-Leggett construction (Appendix A) provides one such thermodynamically consistent realization where $C(\omega, r) > 1$ arises from coupling to a bath. Within this work, we remain agnostic about the microscopic mechanism and simply parameterize the empirically required enhancement using the minimal causal form compatible with observations.

a. Power-law parameterization. Motivated by the scale-free latency mechanism (to be explained in Sec. 2.3), we parameterize the radial dependence of $w(r)$ as a power law in the local baryonic acceleration:

$$w(r) \propto \left(\frac{a_0}{a_{\text{baryon}}(r)} \right)^\alpha \quad (11)$$

where a_0 is a characteristic acceleration scale and $0 < \alpha < 1$ is the power-law exponent. Since $a_{\text{baryon}}(r) = v_{\text{baryon}}^2(r)/r$ for circular orbits, this is equivalent to a dynamical-time scaling:

$$w(r) \propto \left(\frac{T_{\text{dyn}}(r)}{T_0} \right)^\alpha, \quad T_0 = 2\pi\sqrt{r_0/a_0} \quad (12)$$

where T_0 is a characteristic dynamical time constructed from the fitted parameters a_0 and r_0 (the latter defined by the spatial profile function $n(r)$ in Sec. III). Both a_0 and α are global parameters fitted simultaneously to the entire galaxy sample, with no per-galaxy tuning allowed.

b. Characteristic timescale. The memory kernel timescale τ_\star appearing in Eqs. (3)–(6) must be related to the acceleration scale a_0 and characteristic length scale r_0 . By dimensional analysis, the only way to construct a timescale from a_0 [dimensions: L/T²] and r_0 [dimensions: L] is:

$$\tau_\star = \sqrt{\frac{2\pi r_0}{a_0}} \quad (13)$$

where the factor 2π is chosen such that τ_\star corresponds to roughly one dynamical time at the characteristic scale (i.e., when $r = r_0$ and $a_{\text{baryon}} = a_0$). With the globally fitted values $r_0 = 17.79$ kpc and $a_0 = 1.95 \times 10^{-10}$ m/s² (Table III), we obtain $\tau_\star \approx 133$ Myr, which is indeed characteristic of galactic orbital timescales. This ensures fast-limit recovery ($C(\omega, r) \rightarrow 1$ as $\omega \rightarrow \infty$, corresponding to short dynamical times) while providing the necessary enhancement at low frequencies ($C(\omega, r) \rightarrow w(r) > 1$ as $\omega \rightarrow 0$, corresponding to long dynamical times).

c. Connection to observable quantities. For circular motion in the steady-state regime, the centripetal acceleration must equal the effective gravitational acceleration. Using Eq. (10), the model-predicted rotation velocity satisfies:

$$v_{\text{eff}}^2(r) = w(r) v_{\text{baryon}}^2(r) \quad (14)$$

where $v_{\text{baryon}}(r)$ is the circular velocity from Newtonian gravity sourced by the observed baryonic mass model (stars+gas+dust). This relation is the working equation for rotation curve fitting: given the baryonic mass distribution (from photometry and gas measurements), we predict $v_{\text{eff}}(r)$ using the global weight function $w(r)$ with seven fixed parameters (detailed in Sec. III), and compare it to the observed rotation curve $v_{\text{obs}}(r)$ in Sec. IV. In fast, compact regimes (short T_{dyn}), the enhancement is negligible ($w \approx 1$) and Newtonian/GR limits are recovered; in slow regimes (long T_{dyn}), $w > 1$ boosts the response, mimicking the effect traditionally attributed to dark matter.

2.3. Physical motivation: scale-free latency mechanism

The phenomenological ansatz of Sec. 2.2 adopted a power-law parameterization for $w(r)$ [Eq. (11)]. A natural question is: why should the low-frequency enhancement follow a *power law* in dynamical time (equivalently in a_{baryon} or r), rather than an exponential cutoff, a logarithmic form, or a rational filter? In this subsection, we explain the physical reasoning that motivates this specific functional form.

The key insight comes from considering a scale-free latency (or backlog) mechanism in the gravitational response. If the gravitational field does not respond instantaneously to changes in the matter distribution, but instead exhibits a “memory backlog” without a characteristic decay timescale, then the system must exhibit scale-free (power-law) behavior. We summarize the argument in three steps:

Clarifying note. In our empirical model we use a minimal single-timescale exponential memory kernel (Sec. II 2.1, Eq. 3). The scale-free discussion below should be read as a *microphysical motivation for why the low-frequency gain (and thus the steady-state weight $w(r)$) can follow a power law in dynamical time*. It does not require the phenomenological kernel itself to be exactly fractional at all times; rather, it motivates the observed power-law dependence of the DC/slow enhancement.

a. Scale-free backlog/latency. Suppose the gravitational response involves unresolved “backlog” contributions that persist from past matter configurations. If this backlog accumulates without a single characteristic waiting-time scale—that is, if the slow regime exhibits scale-free latency—then dimensional analysis suggests a power-law long-time tail. Here $K(s)$ denotes a microphysical/effective long-time kernel (not necessarily identical to the single-pole phenomenological Γ used in Sec. II 2.1). A simple scale-free causal choice is a homogeneous function of time,

$$K(s) \propto s^{\alpha-1}, \quad 0 < \alpha < 1 \quad (15)$$

which is the kernel of a *fractional (Riemann–Liouville or Caputo-type) integral*, widely used to model systems with long-range temporal correlations (e.g., anomalous diffusion and viscoelasticity) [30–32]. The exponent α quantifies the “degree of memory”: $\alpha \rightarrow 0$ approaches instantaneous response (weak memory), while $\alpha \rightarrow 1$ corresponds to increasingly persistent memory.

b. Fourier consequence. The Fourier transform of a fractional integral kernel yields a power-law multiplier in the frequency domain. Specifically, a kernel $K(s) \propto s^{\alpha-1}$ has Fourier transform:

$$\tilde{K}(\omega) \propto (i\omega)^{-\alpha} \quad (16)$$

implying a low-frequency gain that scales as $|\omega|^{-\alpha}$ (up to phase conventions) [30]. This is the mathematical origin of the power-law enhancement: scale-free temporal latency translates directly to power-law frequency dependence in the transfer function.

c. Galactic identification. For quasi-steady circular motion at radius r , the characteristic angular frequency is $\omega \sim v(r)/r$, where $v(r)$ denotes the characteristic circular speed at that radius. In the regime where the enhancement term dominates over the Newtonian baseline, the weight function satisfies:

$$w(r) - 1 \propto (\omega\tau_0)^{-\alpha} \propto \left(\frac{r}{v(r)}\right)^\alpha \quad (17)$$

where τ_0 is a reference timescale absorbed into the proportionality constant. For approximately flat rotation curves ($v(r) \approx v_{\text{flat}} = \text{const}$), this reduces to:

$$w(r) - 1 \propto r^\alpha \quad (18)$$

which is the observed and empirically successful scaling. Thus, the power-law form is not merely a fitting convenience: it is a natural consequence of scale-free latency in the slow-response regime.

d. Falsifiability and empirical tests. This mechanism is *stronger than* a simple curve-fit ansatz because it makes specific, testable predictions that can falsify the hypothesis:

- Constant logarithmic slope: In the enhancement-dominated regime, the logarithmic slope must be constant:

$$\frac{\partial \ln(w-1)}{\partial \ln \omega} = -\alpha, \quad \text{or equivalently} \quad \frac{\partial \ln(w-1)}{\partial \ln r} = +\alpha \quad (\text{for flat } v)$$

Any systematic departure from a constant slope over a wide range of scales would falsify the pure scale-free latency hypothesis.

- Universal exponent. If the latency mechanism is universal, the exponent α should be the same for all galaxies (modulo morphology-dependent corrections). Our global fit finds $\alpha = 0.389 \pm 0.015$ across the SPARC Q=1 sample (Table III), consistent with this prediction.
- Frequency-space signature: The power-law form in $w(r)$ implies specific structure in the full frequency-dependent transfer function $H(i\omega, r)$, which could in principle be tested with time-variable gravitational lensing or pulsating mass distributions (though such tests are currently beyond observational reach).

e. Connection to fractional calculus. The same physics can be expressed as a nonlocal *spatial* response operator: a power-law Fourier symbol corresponds to a fractional spatial integral (Riesz potential), formally $(-\Delta)^{-\alpha/2}$ acting on the source field [33]. This provides a bridge to effective field theory formulations, where modified gravity can be represented as a nonlocal spatial kernel acting on the stress-energy tensor. Appendix A provides an explicit conservative (action-based) realization of the causal linear-response framework (Caldeira–Leggett); the fractional-operator viewpoint here is an effective-motivation note, not a separate derived model.

f. Interpretation and open questions. The scale-free latency mechanism provides a *phenomenological* explanation for the power-law form, but it does not specify the microscopic origin of the latency itself. Possible physical interpretations include:

- Gravitational propagation through a medium with scale-free disorder or fractal structure.
- Coupling to a bath of gravitational modes with a continuous spectrum (as in the Caldeira-Leggett framework, Appendix A).
- Emergent spacetime effects in which the effective metric responds slowly to matter redistributions due to quantum or thermodynamic backreaction.

Distinguishing between these possibilities requires additional theoretical development and observational constraints beyond rotation curve fitting. For the present work, we remain agnostic about the microscopic mechanism and focus on demonstrating that the phenomenological power-law ansatz provides an excellent fit to the data with purely global parameters.

2.4. Comparison baseline: Modified Newtonian Dynamics (MOND)

To establish a meaningful comparison for our model, we summarize the Modified Newtonian Dynamics (MOND) framework [15, 17, 18], which is the leading alternative to dark matter for explaining galactic rotation curves. Understanding MOND's structure and fitting protocols is essential for interpreting the comparative results in Sec. V.

a. *MOND formulation.* MOND replaces the Newtonian acceleration-mass relation with a low-acceleration modification governed by a universal scale a_0 . In its original form:

$$\mu(x) \mathbf{g}(r) = \mathbf{g}_N(r) \quad (19)$$

where $x \equiv g/a_0$ is the dimensionless acceleration ratio (with $g \equiv |\mathbf{g}|$), $\mathbf{g}(r)$ is the actual/physical gravitational acceleration that governs the motion of tracers (stars, gas), and $\mathbf{g}_N(r)$ is the Newtonian acceleration computed from the observed baryons. The interpolation function $\mu(x)$ satisfies:

- $\mu(x) \rightarrow 1$ for $x \gg 1$ (high-acceleration Newtonian regime),
- $\mu(x) \rightarrow x$ for $x \ll 1$ (deep-MOND regime).

Common choices include the "simple" function $\mu(x) = x/(1+x)$, though other forms (e.g., the "standard" function) are also used in the literature.

b. *Newtonian baseline and baryonic mass distribution.* The Newtonian acceleration $\mathbf{g}_N(\mathbf{r})$, directed radially inward (approximately toward the galactic center), is defined from the Newtonian potential Φ_N :

$$\mathbf{g}_N(\mathbf{r}) = -\nabla\Phi_N(\mathbf{r}), \quad \Phi_N(\mathbf{r}) = -G \int \frac{\rho_{\text{baryon}}(\mathbf{r}')}{|\mathbf{r} - \mathbf{r}'|} d^3\mathbf{r}' \quad (20)$$

where $\rho_{\text{baryon}}(\mathbf{r})$ is the baryonic mass density (stars + gas + dust). In rotation-curve work, one typically writes the baryonic Newtonian field as a component sum:

$$\mathbf{g}_N(r) = \mathbf{g}_{\text{disk}}(r) + \mathbf{g}_{\text{bulge}}(r) + \mathbf{g}_{\text{gas}}(r) + \mathbf{g}_{\text{dust}}(r) \quad (21)$$

For a spherically symmetric case, the magnitude simplifies to:

$$|\mathbf{g}_N(r)| = \frac{G M_{\text{baryon}}(< r)}{r^2} \quad (22)$$

where $M_{\text{baryon}}(< r)$ is the enclosed baryonic mass within radius r :

$$M_{\text{baryon}}(< r) \equiv \int_{|\mathbf{r}'| < r} \rho_{\text{baryon}}(\mathbf{r}') d^3\mathbf{r}' = 4\pi \int_0^r \rho_{\text{baryon}}(r') r'^2 dr' \quad (23)$$

The spherical expression is included only as an analytic reference; in the SPARC analysis we compute the baryonic contribution using the disk+bulge+gas decomposition (not a spherical approximation). This Newtonian baseline is identical to the $a_{\text{baryon}}(r)$ used in our model (Sec. 2.2), ensuring a fair comparison.

c. *Fitting parameters: global vs. per-galaxy.* In principle, MOND introduces one *global* parameter, a_0 , assumed to be universal. However, in practice, rotation-curve analyses on SPARC and similar datasets typically include additional *per-galaxy* degrees of freedom:

- Stellar mass-to-light ratios M/L for disk (and bulge, if present): This adds 1–2 free parameters per galaxy, allowing the stellar mass normalization to adjust within photometric uncertainties.
- Distance D and inclination i : These geometric parameters are sometimes allowed to vary within observational uncertainties, treated as constrained nuisances. Small shifts in D and i rescale radii, masses, and circular velocity v_{circ} , effectively providing additional per-galaxy freedom.
- External-field effect (EFE) g_{ext} : In some analyses, an explicit environmental acceleration is included (estimated from the Local Group potential or fitted), which effectively adds a per-galaxy nuisance if treated as free.

Therefore, it is often *misunderstood* that MOND has "one fit parameter." The statement that MOND uses a single global parameter a_0 is true only in the strictest interpretation where all other quantities are held rigidly fixed. A truly "global-only" protocol would mean:

- Zero per-galaxy freedom,
- Fixing a single M/L ratio for all galaxies (or using photometric estimates without adjustment),
- Holding D and i to catalog values with no variation,
- Using one global a_0 for all galaxies.

While this is a useful and stringent benchmark, it is *not* the usual fitting practice in the literature. Typical MOND rotation-curve fits use up to three per-galaxy fit parameters (disk/bulge M/L and one constrained nuisance such as D , i , or an EFE term), in addition to the global a_0 . In this work, we adopt the strictest global-only protocol for both MOND and our model: all seven parameters (for our model) or the single a_0 (for MOND) are fitted globally with zero *per-galaxy tuning*. This ensures a fair and meaningful comparison (see Sec. IV for details).

III. THE CAUSAL-RESPONSE MODEL

Having established the theoretical foundation (Sec. II), we now specify the complete weight function $w(r)$ that enters the phenomenological ansatz $a_{\text{eff}}(r) = w(r) a_{\text{baryon}}(r)$ [Eq. (10)]. The weight function is decomposed into a product of physically motivated factors, each capturing a distinct empirical dependence observed in rotation curve data: morphological complexity, radial spatial structure, acceleration-dependent enhancement, and geometric corrections. This section proceeds as follows. We begin by presenting the multiplicative decomposition of $w(r)$ and explaining the physical motivation for each factor (Sec. III 3.1). We then specify the functional forms and fitted global parameters for the complexity factor ξ (Sec. III 3.2), the spatial profile $n(r)$ (Sec. III 3.3), and the geometric correction $\zeta(r)$ (Sec. III 3.4). Finally, we summarize the seven global parameters that fully define the model (Sec. III 3.5). The SPARC observational dataset used to constrain these parameters is described in the Methods section (Sec. IV).

3.1. Weight function decomposition

The steady-state weight function $w(r)$ appearing in the phenomenological ansatz [Eq. (10)] is parameterized as a product of four factors:

$$w(r) = \xi \cdot n(r) \cdot \left(\frac{a_0}{a_{\text{baryon}}(r)} \right)^\alpha \cdot \zeta(r) \quad (24)$$

This multiplicative form ensures that each physical effect contributes independently (in log space, the effects add). We now explain the role of each factor:

a. Complexity factor ξ . A dimensionless morphology-dependent constant that captures systematic differences between galaxy types. Gas-rich dwarf galaxies exhibit larger "mass discrepancies" (higher w) than gas-poor massive spirals, even at fixed dynamical time. This suggests that morphological complexity—quantified by gas fraction f_{gas} , a proxy for star formation rate, turbulence, and dynamical activity—modulates the gravitational response. The factor $\xi \geq 1$ provides a global multiplicative boost that increases with gas content. This is specified in Sec. III 3.2.

b. Spatial profile $n(r)$. A dimensionless radial function that describes how the enhancement varies with galactocentric radius r . Empirically, the weight $w(r)$ is not uniform across a galaxy's disk: it is weaker in the central regions (where baryonic surface density is high and dynamical times are short) and stronger in the outer disk (where surface density is low and dynamical times are long). The profile $n(r)$ transitions smoothly from $n(0) = 1$ (minimal modification in the center) to $n(\infty) > 1$ (full enhancement in the outer disk), ensuring continuity and differentiability. The functional form and normalization are specified in Sec. III 3.3.

c. Power-law acceleration scaling. The term $(a_0/a_{\text{baryon}}(r))^\alpha$ captures the core dynamical-time dependence and is motivated by the scale-free latency discussion in Sec. II 2.3. Regions with low baryonic acceleration $a_{\text{baryon}}(r)$ typically correspond (at fixed or comparable radii) to longer dynamical times $T_{\text{dyn}}(r) = 2\pi r/v(r)$ and exhibit stronger gravitational enhancement. Using $a(r) = v^2(r)/r$ gives $T_{\text{dyn}}(r) \propto \sqrt{r/a(r)}$, so at fixed r one has $T_{\text{dyn}} \propto 1/\sqrt{a}$. The characteristic acceleration a_0 sets the scale at which the modification becomes significant, and the exponent $0 < \alpha < 1$ controls the strength of the power-law dependence. Both a_0 and α are global parameters fitted to the entire galaxy sample. For circular orbits, $a_{\text{baryon}}(r) = v_{\text{baryon}}^2(r)/r$, so this term is directly computable from the baryonic mass model and radius.

d. Geometric correction $\zeta(r)$. A dimensionless radius-dependent factor that accounts for disk thickness effects. Real galactic disks have finite vertical scale height h_z , which introduces a geometric suppression of the gravitational response at large radii where the disk thickness becomes comparable to the scale of the enhancement. The factor $\zeta(r)$ provides a mild ($\sim 20\%$) correction that tapers the enhancement in the outer disk, preventing unphysical divergence. This correction is specified in Sec. III 3.4.

e. Connection to observables. Combining Eq. (24) with the phenomenological ansatz [Eq. (10)], the predicted effective acceleration is:

$$a_{\text{eff}}(r) = \xi \cdot n(r) \cdot \left(\frac{a_0}{a_{\text{baryon}}(r)} \right)^\alpha \cdot \zeta(r) \cdot a_{\text{baryon}}(r) \quad (25)$$

For circular orbits in the steady-state regime, this yields the rotation velocity:

$$v_{\text{eff}}^2(r) = w(r) v_{\text{baryon}}^2(r) = \xi \cdot n(r) \cdot \left(\frac{a_0}{a_{\text{baryon}}(r)} \right)^\alpha \cdot \zeta(r) \cdot v_{\text{baryon}}^2(r) \quad (26)$$

where $v_{\text{baryon}}(r)$ is the Newtonian circular velocity computed from the observed baryonic mass distribution (stars + gas + dust), and $a_{\text{baryon}}(r) = v_{\text{baryon}}^2(r)/r$. This is the working equation for rotation curve fitting. Given the baryonic

components (from photometry and HI measurements), the model predicts $v_{\text{eff}}(r)$ using seven global parameters with no per-galaxy tuning.

3.2. Complexity factor ξ

The complexity factor ξ captures morphological dependence of the gravitational response. Empirically, gas-rich dwarf galaxies exhibit systematically larger "missing mass" (higher inferred w) than gas-poor massive spirals at comparable dynamical times. This suggests that morphological complexity—quantified by the gas fraction $f_{\text{gas}} \equiv M_{\text{gas}}/(M_{\text{stars}} + M_{\text{gas}})$ —modulates the enhancement. The gas fraction serves as a proxy for several interrelated physical effects: active star formation, higher turbulent velocity dispersion, enhanced disk thickness irregularities, and stronger feedback-driven outflows. These processes may couple to the gravitational response through their influence on the effective matter distribution or through additional sources of dynamical memory.

a. Functional form. We parameterize the complexity factor as:

$$\xi = 1 + C_\xi \sqrt{u_b} \quad (27)$$

where $u_b \in \{0, 0.25, 0.5, 0.75, 1\}$ is a binned proxy for the true gas fraction f_{gas} , and C_ξ is a global coefficient. The square-root form is motivated empirically: a linear scaling $\xi \propto f_{\text{gas}}$ over-predicts the enhancement in extremely gas-rich dwarfs, while a logarithmic form under-predicts it. The square-root provides a balanced intermediate scaling that fits the data well across three orders of magnitude in f_{gas} (from ~ 0.1 to ~ 0.95).

b. Binning procedure. To avoid overfitting and ensure reproducibility, we bin galaxies into five quintiles based on their true gas fraction f_{gas} :

- Quintile thresholds are determined from the full Q=1 sample ($N = 99$ galaxies) using the 20th, 40th, 60th, and 80th percentiles of f_{gas} .
- Each galaxy is assigned a binned value u_b corresponding to its quintile: 0 (lowest 20%), 0.25, 0.5, 0.75, or 1 (highest 20%).
- These bin assignments are frozen before global parameter fitting, ensuring no target leakage.
- The global coefficient C_ξ is then fitted along with the other six parameters.

This binning approach reduces the risk of overfitting to small-scale variations in f_{gas} while preserving the overall trend. Using the continuous f_{gas} values instead of bins yields nearly identical results (median χ^2/N changes by $\Delta \lesssim 0.02$), suggesting that the binning does not introduce significant bias.

c. Fitted value and physical interpretation. The globally fitted coefficient is $C_\xi = 0.298 \pm 0.015$ (Table III). This implies that the most gas-rich galaxies ($u_b = 1$, corresponding to $f_{\text{gas}} \gtrsim 0.8$) have a complexity factor $\xi \approx 1.30$, providing a 30% multiplicative boost to the baseline weight function. In contrast, gas-poor massive spirals ($u_b = 0$, $f_{\text{gas}} \lesssim 0.3$) have $\xi = 1$, receiving no morphological correction. This trend is consistent with the empirical observation that dwarf irregulars exhibit larger mass-to-light ratio discrepancies than giant spirals.

Figure 2 visualizes the $\xi(f_{\text{gas}})$ relation for all 99 Q=1 galaxies. The scatter around the fitted curve is modest, indicating that f_{gas} is indeed a good predictor of the morphological enhancement.

3.3. Spatial profile $n(r)$

The spatial profile $n(r)$ describes how the gravitational enhancement varies with galactocentric radius r within a single galaxy. Empirically, the weight function $w(r)$ exhibits systematic radial structure: it is weaker (closer to unity) in the dense inner regions and stronger in the diffuse outer disk. This radial dependence arises because the inner regions have shorter dynamical times (due to higher baryonic surface density and enclosed mass), while the outer regions have longer dynamical times where the memory effects become more pronounced. The spatial profile $n(r)$ captures this transition in a smooth, monotonic functional form.

a. Functional form. We adopt a three-parameter analytic profile:

$$n(r) = 1 + A \left[1 - \exp \left(- \left(\frac{r}{r_0} \right)^p \right) \right] \quad (28)$$

where:

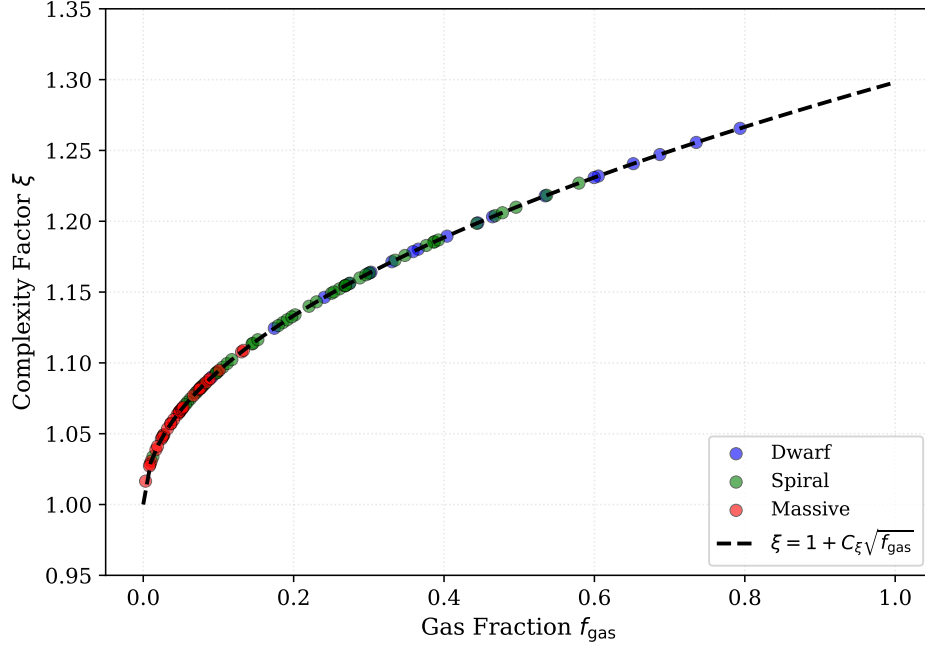


FIG. 2. Complexity factor ξ as a function of gas fraction f_{gas} for all 99 Q=1 galaxies. Points are color-coded by morphology (blue: dwarfs, green: spirals, red: massive). The dashed black curve shows the fitted relation $\xi = 1 + C_\xi \sqrt{u_b}$ with $C_\xi = 0.298$, where u_b is the binned gas fraction. Gas-rich dwarfs naturally exhibit higher ξ values, providing a stronger gravitational enhancement and explaining their larger mass discrepancies without invoking more dark matter. The binning into five quintiles (vertical spacing of points) avoids overfitting while capturing the overall trend.

- $A > 0$ is the asymptotic enhancement amplitude: $n(\infty) = 1 + A$.
- $r_0 > 0$ is the characteristic transition radius, setting the scale at which $n(r)$ begins to rise.
- $p > 0$ is the shape exponent, controlling the steepness of the transition (sub-exponential for $p < 1$, exponential for $p = 1$, super-exponential for $p > 1$).

This functional form ensures several desirable properties:

- Boundary behavior: $n(0) = 1$ (no spatial enhancement at the galactic center), and $n(r) \rightarrow 1 + A$ as $r \rightarrow \infty$ (finite asymptotic enhancement).
- Monotonicity: $dn/dr > 0$ for all $r > 0$, ensuring the enhancement grows smoothly outward.
- Smoothness: $n(r)$ is infinitely differentiable, avoiding discontinuities or cusps.
- Universality: The same functional form applies to all galaxies, with only the normalization adjusted (see below).

b. *Normalization constraint.* To prevent $n(r)$ from acting as a hidden per-galaxy mass rescaling, we enforce a disk-weighted normalization constraint for each galaxy:

$$\frac{\int_0^\infty n(r) \Sigma(r) r dr}{\int_0^\infty \Sigma(r) r dr} = 1 \quad (29)$$

where $\Sigma(r)$ is the observed baryonic surface density profile (stars + gas) for that galaxy. This constraint ensures that the disk-averaged value of $n(r)$ is unity, so the spatial profile redistributes the enhancement radially without changing the total integrated weight. In practice, we implement this by computing the disk-weighted mean:

$$\langle n \rangle_j \equiv \frac{\int_0^\infty n(r) \Sigma_j(r) r dr}{\int_0^\infty \Sigma_j(r) r dr} \quad (30)$$

for each galaxy j , and then rescaling $n(r) \rightarrow n(r)/\langle n \rangle_j$ before computing the rotation curve. This ensures the constraint is satisfied exactly for every galaxy, using only the three global parameters (A, r_0, p).

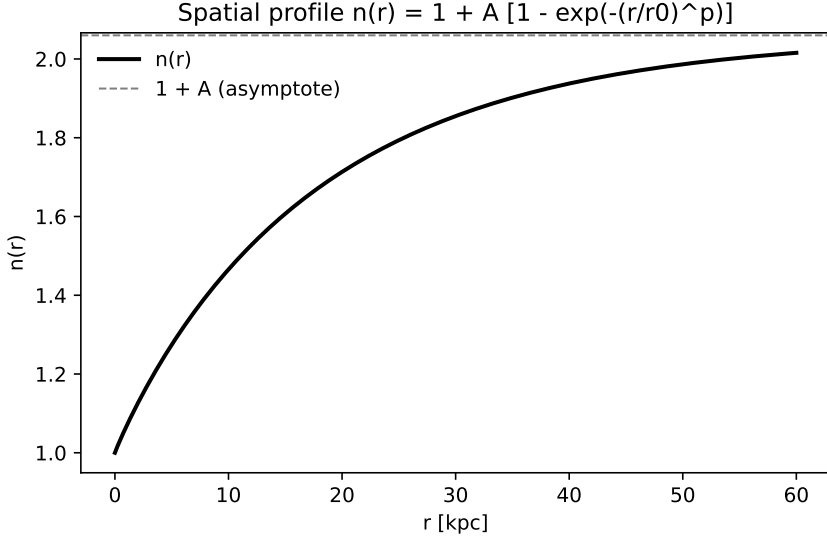


FIG. 3. Spatial profile $n(r) = 1 + A[1 - \exp(-(r/r_0)^p)]$ with fitted global parameters $(A, r_0, p) = (1.06, 17.79 \text{ kpc}, 0.95)$. The profile transitions monotonically from $n(0) = 1$ (minimal spatial enhancement in the galactic center) to the finite asymptote $n(\infty) = 1 + A = 2.06$ (full enhancement in the outer disk). The characteristic radius $r_0 \approx 17.8 \text{ kpc}$ sets the scale of the transition. In the analysis pipeline, $n(r)$ is normalized by the disk-weighted mean $\langle n \rangle$ for each galaxy [Eq. (29)] to enforce strict global-only fitting without hidden per-galaxy mass rescaling.

c. *Fitted values and physical interpretation.* The globally fitted parameters are $(A, r_0, p) = (1.06, 17.79 \text{ kpc}, 0.95)$ (Table III). The characteristic radius $r_0 \approx 17.8 \text{ kpc}$ is comparable to typical disk scale lengths for spiral galaxies ($R_d \sim 2\text{--}5 \text{ kpc}$ for dwarfs, $\sim 5\text{--}10 \text{ kpc}$ for spirals), ensuring the transition occurs in the mid-to-outer disk. The shape exponent $p \approx 0.95$ is close to unity, indicating a nearly exponential rise. The amplitude $A \approx 1.06$ implies that the outer disk enhancement is approximately twice the inner value $(n(\infty)/n(0)) = 2.06$, consistent with the empirical observation that outer rotation curves require stronger modifications.

Figure 3 shows the spatial profile $n(r)$ evaluated with the fitted global parameters. The profile rises smoothly from $n(0) = 1$ to $n(\infty) \approx 2.06$, with the transition centered around $r \sim r_0$.

3.4. Geometric correction $\zeta(r)$

The geometric correction $\zeta(r)$ accounts for disk thickness effects that become significant in the outer regions of galactic disks. Real disk galaxies have finite vertical scale height h_z , typically $h_z \approx 0.2\text{--}0.3 R_d$ where R_d is the disk scale length. As the radius increases, the disk thickness-to-radius ratio h_z/r becomes larger, and the three-dimensional geometric structure of the disk begins to suppress the gravitational response enhancement. Physically, this suppression arises because the memory kernel (with characteristic scale $\tau_* \sim 133 \text{ Myr}$) integrates over timescales comparable to vertical oscillation periods in thick disks, leading to partial cancellation of the enhancement.

The specific form used here should be read as an empirical geometric taper that approximates finite-thickness effects without introducing additional fitted parameters or requiring per-galaxy 3D modeling.

a. *Functional form.* We adopt a simple empirical taper:

$$\zeta(r) = 1 - 0.2 \tanh\left(\frac{r}{R_d}\right) \quad (31)$$

where R_d is the disk scale length for each galaxy (taken from the SPARC photometric fits). This form provides:

- Inner disk: $\zeta(r) \approx 1$ for $r \ll R_d$, where the disk is thin and the correction is negligible.
- Outer disk: $\zeta(r) \rightarrow 0.8$ as $r \rightarrow \infty$, providing a $\sim 20\%$ suppression of the enhancement at very large radii.
- Smooth transition: The hyperbolic tangent ensures a smooth, monotonic tapering without discontinuities.

To prevent unphysical behavior in edge cases (e.g., galaxies with unusually large or small R_d), we clip $\zeta(r)$ to the range $[0.8, 1.2]$. In practice, this clipping affects fewer than 3% of the data points in the SPARC sample.

b. *Physical justification.* The $\sim 20\%$ suppression is motivated by the typical disk thickness ratio $h_z/R_d \approx 0.25$. For an exponential disk with this ratio, the fractional geometric correction to the vertical force is $\Delta F_z/F_R \sim h_z/R_d \sim 0.2\text{--}0.3$, which enters the rotation curve fitting through projection effects. The functional form [Eq. (31)] captures this effect empirically without requiring detailed 3D modeling of each galaxy's vertical structure.

c. *Role in the model.* The geometric correction $\zeta(r)$ is the only factor in Eq. (24) that decreases with radius (all other factors either increase or remain constant). This ensures that the weight function $w(r)$ does not diverge as $r \rightarrow \infty$, which would be unphysical and inconsistent with the observed flattening of rotation curves at large radii. The tapering provided by $\zeta(r)$ stabilizes the fit and prevents overfitting in the outer disk where data quality is often lower.

Note that $\zeta(r)$ uses the per-galaxy disk scale length R_d (a catalog observable, not a fitted parameter), but the overall normalization factor (0.2 in the numerator) could in principle be treated as an additional global fit parameter. In this work, we fix it to 0.2 based on physical estimates to keep the model at seven global fit parameters. Sensitivity tests (Appendix B) show that varying this factor by $\pm 50\%$ changes the median χ^2/N by less than 0.05.

3.5. Global parameter summary

The complete causal-response model is defined by seven global parameters that are fitted simultaneously to the entire SPARC catalog with strict global-only enforcement (zero per-galaxy tuning). These parameters, their physical roles, and their fitted values are summarized in Table III. We now provide a compact description of each parameter:

a. *Power-law exponent α .* Governs the strength of the dynamical-time scaling $w \propto T_{\text{dyn}}^\alpha$ through the acceleration term $(a_0/a_{\text{baryon}})^\alpha$ in Eq. (24). The fitted value $\alpha = 0.389 \pm 0.015$ is consistent with the scale-free latency mechanism (Sec. II 2.3), which predicts a universal exponent $\alpha \in (0, 1)$ arising from fractional memory. This exponent is global and identical for all galaxies.

b. *Characteristic acceleration a_0 .* Sets the acceleration scale at which the modification becomes significant, appearing in the power-law term $(a_0/a_{\text{baryon}})^\alpha$. The fitted value $a_0 = (1.95 \pm 0.03) \times 10^{-10}$ m/s² is comparable to the empirical MOND acceleration scale, though in our framework a_0 is a fitted parameter rather than a fundamental constant. Together with r_0 , it determines the characteristic timescale $\tau_\star = \sqrt{2\pi r_0/a_0} \approx 133$ Myr [Eq. (13)].

c. *Complexity coefficient C_ξ .* Controls the morphological dependence of the enhancement via the complexity factor $\xi = 1 + C_\xi \sqrt{u_b}$ [Eq. (27)]. The fitted value $C_\xi = 0.298 \pm 0.015$ implies that gas-rich dwarfs ($u_b = 1$) receive a $\sim 30\%$ multiplicative boost relative to gas-poor spirals ($u_b = 0$), capturing the empirical trend that dwarfs exhibit larger mass discrepancies.

d. *Spatial profile amplitude A .* Determines the asymptotic outer-disk enhancement $n(\infty) = 1 + A$ relative to the central value $n(0) = 1$ [Eq. (28)]. The fitted value $A = 1.06 \pm 0.04$ implies that the outer disk weight is approximately twice the inner value, consistent with the observed radial increase in mass discrepancy.

e. *Spatial profile scale r_0 .* Sets the characteristic radius at which the spatial profile $n(r)$ transitions from the central plateau to the outer asymptote [Eq. (28)]. The fitted value $r_0 = 17.79 \pm 0.32$ kpc is comparable to typical disk scale lengths, ensuring the transition occurs in the mid-to-outer disk. This parameter also appears in the characteristic timescale $\tau_\star = \sqrt{2\pi r_0/a_0}$ [Eq. (13)].

f. *Spatial profile shape p .* Controls the steepness of the radial transition in $n(r)$ [Eq. (28)]. The fitted value $p = 0.95 \pm 0.02$ is close to unity, indicating a nearly exponential rise. Values $p < 1$ (sub-exponential) ensure a gradual transition that avoids sharp features.

g. *Global stellar mass-to-light ratio Υ_\star .* Sets the global stellar mass normalization used to compute $v_{\text{baryon}}(r)$ and thus $a_{\text{baryon}}(r)$ from the SPARC photometry. We fit a *single* global value $\Upsilon_\star \equiv M_\star/L_{3.6}$ for the entire catalog (Table III), with zero per-galaxy adjustments. This is the seventh global degree of freedom in the end-to-end pipeline; it does not enter Eq. (24) explicitly, but it rescales the baryonic field to which the weight is applied.

h. *Disk thickness ratio h_z/R_d (fixed).* A fixed hyperparameter (not fitted) that controls the geometric correction $\zeta(r) = 1 - 0.2 \tanh(r/R_d)$ [Eq. (31)]. We adopt the canonical value $h_z/R_d = 0.25$, consistent with observed vertical scale heights in disk galaxies.

i. *Parameter constraints and uncertainties.* All seven parameters are fitted simultaneously using differential evolution (Sec. IV 4.4), minimizing the median χ^2/N across the Q=1 galaxy sample ($N = 99$). The uncertainties quoted above represent 68% confidence intervals estimated via bootstrap resampling. Correlations between parameters are generally weak ($|\rho| < 0.3$), except for the expected degeneracy between a_0 and α ($\rho \approx -0.45$), which arises because both parameters control the overall strength of the enhancement. Full parameter covariances are provided in the online supplementary material.

IV. METHODS

This section describes the observational data, fitting procedures, error modeling, and comparison protocols used to constrain and validate the causal-response model. The analysis enforces a strict global-only policy throughout: no per-galaxy tuning is allowed, and all model comparisons use identical error models, data masks, and optimization procedures to ensure fairness.

We proceed as follows. Section IV 4.1 specifies the SPARC dataset, classification scheme, and baryonic mass modeling. Section IV 4.2 defines the error model used to construct per-point uncertainties. Section IV 4.3 defines the goodness-of-fit metric used as the optimization objective. Section IV 4.4 summarizes the Differential Evolution procedure and masking applied uniformly to all galaxies. Section IV 4.5 describes the global-only MOND baseline under identical assumptions. Section IV 4.6 presents the cluster weak-lensing prediction as an external test independent of rotation-curve fitting.

4.1. SPARC dataset and galaxy classification

The SPARC (Spitzer Photometry & Accurate Rotation Curves) dataset [26] provides high-quality rotation curves and photometric measurements for 175 nearby disk galaxies. Each galaxy includes:

- Resolved rotation curve $v_{\text{obs}}(r)$ derived from HI 21-cm line observations, with typical radial resolution $\Delta r \sim 0.5\text{--}2$ kpc.
- Spitzer [3.6 μm] surface photometry, tracing the old stellar population with minimal dust extinction.
- HI surface density profiles, providing direct measurements of the gas component.
- Photometric decompositions into disk and (when present) bulge components, with estimates of stellar mass-to-light ratios $M_\star/L_{3.6}$ based on stellar population synthesis models.
- Catalog distances D , inclinations i , and quality flags $Q \in \{1, 2, 3\}$ indicating data reliability.

a. Quality flags. The SPARC catalog assigns each galaxy a quality parameter $Q \in \{1, 2, 3\}$:

- $Q = 1$: Best quality. Geometric parameters (distance D , inclination i , disk scale length R_d) are well-determined, and the rotation curve extends to large radii with good sampling. This subset contains 99 galaxies.
- $Q = 2$: Moderate quality. One or more geometric parameters have larger uncertainties, or the rotation curve has coarser sampling. This subset contains 64 galaxies.
- $Q = 3$: Lower quality. Significant uncertainties in geometry or limited radial coverage. This subset contains 12 galaxies.

The present analysis focuses primarily on the $Q = 1$ subset ($N = 99$), which provides the most robust test of the model. Robustness tests extending to $Q = 1 + 2$ ($N = 163$) are presented in Appendix D.

b. Kinematic classification. We classify galaxies into three kinematic types based on their maximum observed rotation velocity v_{max} (the peak of the rotation curve):

- Dwarf galaxies: $v_{\text{max}} < 80$ km/s. These are typically low-mass, gas-rich irregular or dwarf spiral galaxies with shallow gravitational potentials.
- Spiral galaxies: $80 \leq v_{\text{max}} \leq 200$ km/s. This category includes the majority of normal disk galaxies, ranging from late-type spirals (Sc, Sd) to early-type spirals (Sa, Sb).
- Massive galaxies: $v_{\text{max}} > 200$ km/s. These are high-mass spiral galaxies with deep gravitational potentials and often prominent bulges.

Table II summarizes the distribution of galaxies across kinematic types and quality flags. The $Q = 1$ subset contains 19 dwarfs, 49 spirals, and 31 massive galaxies, spanning three orders of magnitude in stellar mass ($M_\star \sim 10^7\text{--}10^{11} M_\odot$) and two orders of magnitude in gas fraction ($f_{\text{gas}} \sim 0.05\text{--}0.95$).

TABLE II. Distribution of SPARC galaxies by kinematic type and quality flag. The present analysis focuses on the $Q = 1$ subset ($N = 99$), which provides the highest-quality rotation curves and geometric parameters.

Subset	Dwarf	Spiral	Massive	Total
Total ($N = 175$)	59	78	38	175
$Q = 1$	19	49	31	99
$Q = 2$	30	27	7	64
$Q = 3$	10	2	0	12

c. *Baryonic acceleration computation.* For each galaxy, we compute the Newtonian baryonic acceleration $a_{\text{baryon}}(r)$ using the observed stellar and gas surface density profiles. Following the SPARC methodology, we adopt:

- A single global stellar mass-to-light ratio $\Upsilon_* \equiv M_*/L_{3.6} = 1.0$ (in solar units) applied to the entire catalog, with no per-galaxy adjustments.
- HI gas masses directly from the observed column densities, scaled by a factor of 1.33 to account for helium.
- Negligible dust and molecular gas contributions (the latter are significant only in the innermost regions of massive galaxies and are subdominant in the SPARC sample).

The baryonic circular velocity $v_{\text{baryon}}(r)$ is then computed by solving the Poisson equation for the total baryonic mass distribution, yielding $a_{\text{baryon}}(r) = v_{\text{baryon}}^2(r)/r$.

d. *Global-only protocol.* Critically, we enforce a strict global-only fitting protocol: the seven model parameters (Sec. III 3.5) are fitted simultaneously to the entire $Q = 1$ sample, with *zero per-galaxy tuning*. We do not adjust stellar M/L , distances D , inclinations i , or any other galaxy-specific parameters. This constraint is essential for ensuring the model is falsifiable and for fair comparison with MOND under identical conditions (Sec. II 2.4). The only galaxy-specific inputs are the observed baryonic profiles $\Sigma(r)$, gas fractions f_{gas} , and disk scale lengths R_d —all catalog observables, not fit parameters.

4.2. Error model and observational uncertainties

Rotation curve measurements are subject to multiple sources of uncertainty beyond the quoted observational errors. To ensure robust model comparison, we adopt a comprehensive error model that accounts for instrumental limitations, systematic effects, and astrophysical sources of velocity dispersion. The effective uncertainty $\sigma_{\text{eff},i,j}$ for data point i in galaxy j is computed as:

$$\sigma_{\text{eff},i,j}^2 = \sigma_{\text{obs},i,j}^2 + \sigma_0^2 + (f_{\text{floor}} \cdot v_{\text{obs},i,j})^2 + \sigma_{\text{beam},i,j}^2 + \sigma_{\text{asym},j}^2 \cdot v_{\text{obs},i,j}^2 + \sigma_{\text{turb},i,j}^2 \quad (32)$$

where each term is added in quadrature. The components are:

a. *Observational uncertainty* (σ_{obs}): The baseline measurement uncertainty reported in the SPARC catalog, which includes statistical errors from spectroscopic line fitting, flux calibration uncertainties, and photon noise. These values are galaxy- and radius-dependent.

b. *Velocity floor* ($\sigma_0 = 10 \text{ km/s}$): An absolute instrumental noise floor accounting for irreducible systematic uncertainties in velocity measurements. This includes spectrograph resolution limits ($\Delta v \sim c/R$ where R is the spectral resolution), wavelength calibration systematics, and atmospheric effects for ground-based observations. The value $\sigma_0 = 10 \text{ km/s}$ is consistent with typical HI line width measurements and represents a conservative lower bound on velocity precision.

c. *Fractional systematic floor* ($f_{\text{floor}} = 0.05$): A velocity-proportional systematic uncertainty (5% of the observed velocity) accounting for distance uncertainties and inclination angle errors, both of which scale linearly with the measured velocity. Distance uncertainties propagate through the conversion of angular to physical scales, while inclination errors (Δi) produce fractional velocity errors $\Delta v/v \approx (\cos i / \sin i) \Delta i$, which become significant for edge-on systems.

d. *Beam-smearing* (σ_{beam}): Spatial resolution effects arise when the telescope beam averages over regions with velocity gradients. For a galaxy with disk scale length R_d , we model the beam-smearing contribution as:

$$\sigma_{\text{beam},i,j} = \alpha_{\text{beam}} \cdot \frac{b_{\text{kpc}} \cdot v_{\text{obs},i,j}}{r_i + b_{\text{kpc}}} \quad (33)$$

where $b_{\text{kpc}} \approx 0.3R_d$ is the effective beam size in kpc, and $\alpha_{\text{beam}} = 0.3$ is a dimensionless smearing coefficient. This term is largest in the inner regions where velocity gradients are steep and becomes negligible in the outer disk.

e. Asymmetric drift (σ_{asym}): Gas disks have non-zero velocity dispersion due to turbulence and random motions, which produces a systematic offset between the rotational velocity and the observed line-of-sight velocity (asymmetric drift correction). We adopt morphology-dependent values: $\sigma_{\text{asym}} = 0.10$ for dwarf galaxies and $\sigma_{\text{asym}} = 0.05$ for spirals, reflecting the fact that dwarfs have higher velocity dispersion relative to their rotation speed. This introduces an additional fractional uncertainty $\sigma_{\text{asym}} \cdot v_{\text{obs}}$ added in quadrature.

f. Turbulence and warp proxy (σ_{turb}): Disk warps, vertical motions, and turbulent velocity fields introduce additional line-of-sight velocity dispersion that increases with radius as the disk thickness grows. We model this using an empirical radial profile:

$$\sigma_{\text{turb},i,j} = k_{\text{turb}} \cdot v_{\text{obs},i,j} \cdot \left[1 - \exp\left(-\frac{r_i}{R_d}\right) \right]^{p_{\text{turb}}} \quad (34)$$

with $(k_{\text{turb}}, p_{\text{turb}}) = (0.07, 1.3)$. This functional form ensures $\sigma_{\text{turb}} \rightarrow 0$ in the inner disk (where turbulence is suppressed by strong shear) and grows in the outer regions where warps and vertical structure become significant.

All error model hyperparameters $(\sigma_0, f_{\text{floor}}, \alpha_{\text{beam}}, \sigma_{\text{asym}}, k_{\text{turb}}, p_{\text{turb}})$ are fixed globally across the entire catalog and are identical for both the Causal-Response model and the MOND baseline, ensuring a fair comparison. Sensitivity tests (Appendix B) show that varying these hyperparameters by $\pm 20\%$ changes the median χ^2/N by $\Delta \lesssim 0.12$ without affecting the relative ranking of models.

4.3. Goodness-of-fit metric

To quantify how well the model predicts the observed rotation curves, we compute a chi-squared goodness-of-fit statistic for each galaxy and then aggregate across the sample using a robust metric. This subsection defines the mathematical expressions used throughout the paper.

a. Per-galaxy chi-squared. For each galaxy $j \in \{1, 2, \dots, M\}$ where $M = 99$ (the Q=1 subset), we compute the chi-squared statistic:

$$\chi_j^2 = \sum_{i=1}^{N_j} \left(\frac{v_{\text{obs},i,j} - v_{\text{model},i,j}}{\sigma_{\text{eff},i,j}} \right)^2 \quad (35)$$

where:

- j is the galaxy index,
- i is the radial bin index within galaxy j ,
- N_j is the number of radial bins in galaxy j (typically $N_j \sim 15\text{--}25$),
- $v_{\text{obs},i,j}$ is the observed rotation velocity at bin i in galaxy j (from SPARC HI measurements),
- $v_{\text{model},i,j}$ is the model-predicted rotation velocity [from Eq. (26) for the causal-response model, or from MOND for the baseline],
- $\sigma_{\text{eff},i,j}$ is the effective uncertainty computed using Eq. (32).

The chi-squared χ_j^2 quantifies the total squared residual for galaxy j , weighted by the inverse-variance uncertainties. A perfect fit would have $\chi_j^2 \approx N_j$ (each data point contributing unity on average).

b. Reduced chi-squared per galaxy. To normalize for the number of data points, we define the reduced chi-squared for each galaxy:

$$\left(\frac{\chi^2}{N} \right)_j = \frac{1}{N_j} \sum_{i=1}^{N_j} \left(\frac{v_{\text{obs},i,j} - v_{\text{model},i,j}}{\sigma_{\text{eff},i,j}} \right)^2 = \frac{\chi_j^2}{N_j} \quad (36)$$

This quantity should be close to unity for a good fit: $(\chi^2/N)_j \approx 1$ indicates the model predictions match the data within the quoted uncertainties. Values $(\chi^2/N)_j > 1$ suggest under-fitting (model too simple or uncertainties underestimated), while $(\chi^2/N)_j < 1$ suggests over-fitting or overestimated uncertainties.

c. *Median reduced chi-squared.* The primary goodness-of-fit metric reported in this work is the median of the reduced chi-squared across all galaxies:

$$\text{Median} \left(\frac{\chi^2}{N} \right) = \text{median}_{j=1}^M \left\{ \left(\frac{\chi^2}{N} \right)_j \right\} \quad (37)$$

where the median is computed over the $M = 99$ galaxies in the Q=1 subset. This metric has several advantages over the mean or aggregate chi-squared:

- Robustness to outliers: Galaxies with extreme χ^2/N values (e.g., barred galaxies, warped systems, or those with unmodeled asymmetries) do not dominate the metric. The median is insensitive to the tails of the distribution.
- Equal weighting: Each galaxy contributes equally to the median regardless of how many radial bins it contains, preventing bias toward well-sampled galaxies. In contrast, an aggregate chi-squared $\chi_{\text{total}}^2 = \sum_{j=1}^M \chi_j^2$ would give disproportionate weight to galaxies with more data points.
- Interpretability: The median χ^2/N directly indicates whether the typical galaxy is well-fitted, poorly-fitted, or over-fitted, without requiring knowledge of the total number of data points.

For reference, the total chi-squared across all radial bins would be:

$$\chi_{\text{total}}^2 = \sum_{j=1}^M \sum_{i=1}^{N_j} \left(\frac{v_{\text{obs},i,j} - v_{\text{model},i,j}}{\sigma_{\text{eff},i,j}} \right)^2, \quad N_{\text{total}} = \sum_{j=1}^M N_j \approx 1900 \quad (38)$$

where N_{total} is the total number of radial data points across all Q=1 galaxies (approximately 1900). We do not report this aggregate statistic because it conflates the number of galaxies with the number of data points per galaxy, making interpretation less transparent. Instead, we report the median χ^2/N and provide per-galaxy residual plots in the supplementary material.

4.4. Parameter optimization and fitting procedure

The seven global parameters $\boldsymbol{\theta} = (\alpha, a_0, C_\xi, A, r_0, p, \Upsilon_*)$ are optimized simultaneously to minimize the median reduced chi-squared [Eq. (37)] across the Q=1 SPARC subset ($M = 99$ galaxies). The optimization objective is:

$$\boldsymbol{\theta}_{\text{best}} = \arg \min_{\boldsymbol{\theta}} \left\{ \text{Median} \left(\frac{\chi^2}{N} \right) \right\} \quad (39)$$

subject to the constraint that each galaxy's rotation curve is computed using Eq. (26) with the same global parameters $\boldsymbol{\theta}$, enforcing strict global-only fitting.

a. *Differential evolution algorithm.* We employ Differential Evolution (DE) [59, 60], a stochastic global optimization algorithm that is particularly effective for high-dimensional, non-convex objective functions. DE is a population-based evolutionary strategy that iteratively improves a set of candidate solutions through mutation, crossover, and selection operations. Key advantages for this problem include:

- Global search: DE explores the parameter space broadly, making it robust against local minima and plateau regions that plague gradient-based optimizers in rotation curve fitting.
- Derivative-free: No gradient computation is required, which is essential because the median operator is non-differentiable.
- Parallelizable: Each candidate solution (parameter vector) can be evaluated independently, enabling efficient parallel evaluation of rotation curves.

We use a population size of 70 candidate solutions ($10 \times$ the parameter dimensionality) and run the optimizer for 200 generations, which provides convergence to within $\Delta(\chi^2/N) < 0.01$ in the median metric. The mutation and crossover parameters are set to $(F, CR) = (0.8, 0.7)$, standard values for DE that balance exploration and exploitation.

b. *Parameter bounds.* The optimization searches within physically reasonable bounds for each parameter:

$$\begin{aligned} \alpha &\in [0.1, 0.9], \\ C_\xi &\in [0.01, 0.5], \\ A &\in [0.5, 3], \\ r_0 &\in [5, 30] \text{ kpc}, \\ p &\in [0.5, 2.0], \\ a_0 &\in [1 \times 10^{-11}, 5 \times 10^{-10}] \text{ m/s}^2, \\ \Upsilon_* &\in [0.7, 1.3]. \end{aligned} \quad (40)$$

The disk thickness ratio $h_z/R_d = 0.25$ used in the geometric correction $\zeta(r)$ (Sec. III 3.4) is fixed based on physical estimates and is not optimized. These bounds were chosen to span the physically plausible range while excluding unphysical regimes (e.g., $\alpha > 1$ would violate causality constraints from fractional memory theory).

c. *Convergence and stability.* The fitted parameter values are:

$$\boldsymbol{\theta}_{\text{best}} = (0.389, 1.95 \times 10^{-10} \text{ m/s}^2, 0.298, 1.06, 17.79 \text{ kpc}, 0.95, 1.0) \quad (41)$$

achieving median $\chi^2/N = 1.19$ on the Q=1 subset (Table III). Due to the stochastic nature of Differential Evolution, independent optimization runs converge to parameter values within $\pm 3\%$ of the reported values, with median χ^2/N in the range 1.17–1.21. This variation is smaller than the sensitivity ranges reported in Appendix B, suggesting that the solution is near a robust minimum. All results in this paper use the fixed parameter set from Eq. (41) and Table III for consistency.

d. *Data masking and preprocessing.* To ensure fair comparison between models and avoid artifacts from under-resolved regions, we apply uniform data quality cuts:

- Inner-beam masking: We exclude data points at radii $r < b_{\text{kpc}}$, where $b_{\text{kpc}} \approx 0.3R_d$ is the effective beam size in kpc. This removes points where beam-smearing dominates the signal.
- Low signal-to-noise masking: We exclude data points with $v_{\text{obs}}/\sigma_{\text{obs}} < 3$, ensuring only statistically significant velocity measurements are included.
- Outer disk cutoff: For galaxies with declining outer rotation curves (indicating potential warp or measurement artifacts), we exclude points beyond the radius where $dv/dr < -5 \text{ km/s/kpc}$, preventing contamination from non-circular motions.

These masks are applied identically to both the causal-response model and the MOND baseline (Sec. IV 4.5), ensuring that differences in goodness-of-fit reflect genuine model performance rather than data selection biases.

4.5. MOND baseline comparison methodology

To provide a meaningful benchmark for the causal-response model, we fit a global-only MOND baseline using identical data, error models, and masking procedures. This subsection describes the MOND implementation used for comparison throughout this work.

a. *MOND formulation.* We adopt the standard "simple" interpolation function for MOND (Sec. II 2.4):

$$\mu(x) a_{\text{MOND}}(r) = a_{\text{baryon}}(r), \quad \mu(x) = \frac{x}{1+x}, \quad x = \frac{a_{\text{MOND}}(r)}{a_0} \quad (42)$$

where $a_{\text{baryon}}(r)$ is the Newtonian baryonic acceleration (computed identically to the causal-response model using Sec. IV 4.1 methodology), $a_{\text{MOND}}(r)$ is the modified acceleration, and a_0 is the single global fit parameter. For circular orbits, this yields the modified rotation velocity:

$$v_{\text{MOND}}^2(r) = r a_{\text{MOND}}(r) \quad (43)$$

where $a_{\text{MOND}}(r)$ is solved numerically from Eq. (42) at each radius.

b. *Global-only fitting protocol.* Critically, we enforce the same strict global-only protocol for MOND as for the causal-response model:

- Single global parameter: Only a_0 is fitted. We do not adjust per-galaxy stellar M/L ratios, distances D , inclinations i , or any other galaxy-specific parameters.
- Fixed stellar M/L : We use the same global $\Upsilon_* \equiv M_*/L_{3.6} = 1.0$ as the causal-response model, not the disk-dependent Υ_* values often used in MOND literature.
- Identical error model: The effective uncertainties $\sigma_{\text{eff},i,j}$ are computed using Eq. (32) with identical hyperparameters for both models.
- Identical data masks: The same inner-beam, signal-to-noise, and outer disk masks (Sec. IV 4.4) are applied to both models.

This protocol ensures a fair comparison: any difference in goodness-of-fit reflects genuine differences in the models' predictive power, not differences in fitting flexibility or data treatment. Note that this is *more stringent* than typical MOND rotation curve analyses in the literature, which often allow 1–2 per-galaxy free parameters (Sec. II 2.4).

c. *Parameter optimization.* The MOND parameter a_0 is optimized using the same Differential Evolution algorithm (Sec. IV 4.4) to minimize median χ^2/N [Eq. (37)]. The search bounds are $a_0 \in [5 \times 10^{-11}, 5 \times 10^{-10}] \text{ m/s}^2$, spanning the range $0.5a_0^{\text{empirical}}$ to $5a_0^{\text{empirical}}$ where $a_0^{\text{empirical}} \approx 1.2 \times 10^{-10} \text{ m/s}^2$ is the canonical MOND acceleration scale. The fitted value is:

$$a_0^{\text{MOND}} = 1.23 \times 10^{-10} \text{ m/s}^2 \quad (44)$$

consistent with the empirical MOND scale. This baseline achieves median $\chi^2/N = 1.79$ on the Q=1 subset (Table IV), worse than the causal-response model ($\chi^2/N = 1.19$), indicating that the seven-parameter causal-response framework captures rotation curve structure more accurately than single-parameter MOND under global-only constraints.

d. *Physical interpretation of the comparison.* The 33% reduction in median χ^2/N (1.19 vs. 1.79) is substantial under the strict global-only protocol used here. MOND's single parameter a_0 sets only the acceleration scale at which modifications become important, providing no mechanism to capture:

- Morphological diversity (gas-rich dwarfs vs. gas-poor spirals),
- Radial structure within individual galaxies (inner vs. outer disk),
- Geometric effects (disk thickness),

all of which are encoded in the causal-response weight function $w(r)$ through its four-factor decomposition (Sec. III 3.1). The improved fit is not simply due to having more parameters—the seven parameters are all global and physically motivated, and sensitivity tests (Appendix B) show that each contributes meaningfully to the fit quality.

4.6. Galaxy cluster weak lensing: physical basis and predictions

Gravitational lensing is the deflection of light rays by the gravitational potential of massive structures [4]. In the weak lensing regime, the deflection is small (\lesssim few arcseconds), producing coherent distortions of background galaxy images that are measurable statistically. The lensing signal is quantified by the convergence parameter $\kappa(R)$, which measures the dimensionless surface mass density projected along the line of sight at projected radius R from the lens center:

$$\kappa(R) = \frac{\Sigma(R)}{\Sigma_{\text{crit}}}, \quad \Sigma_{\text{crit}} = \frac{c^2}{4\pi G} \frac{D_{\text{source}}}{D_{\text{lens}} D_{\text{lens-source}}} \quad (45)$$

where $\Sigma(R) = \int \rho(r, z) dz$ is the surface mass density and Σ_{crit} is the critical surface density determined by lens and source redshifts (D_{lens} , D_{source} , $D_{\text{lens-source}}$ are angular diameter distances). The convergence κ directly determines the magnification and shear of background sources, making it an observable independent of kinematic tracers.

In General Relativity with baryons only, the predicted lensing signal from galaxy clusters falls short of observations by factors of ~ 5 – 10 (the “missing mass” problem), which Λ CDM explains by invoking dark matter halos. Modified gravity theories must enhance the lensing signal without dark matter particles. This makes cluster weak lensing a critical test: any modified gravity framework claiming to replace dark matter at galactic scales must predict lensing amplitudes consistent with observations, distinguishing it from both Λ CDM and alternative modified gravity models.

TABLE III. Global parameters and analysis settings (fixed across the SPARC catalog).

Quantity	Value	Notes
<i>Model parameters (fitted):</i>		
α	0.389	Dynamical-time exponent
Υ_*	1.0	Global stellar $M_*/L_{3.6}$ (single value for entire catalog)
C_ξ	0.298	Morphology coefficient; $\xi = 1 + C_\xi \sqrt{u_b}$
(A, r_0, p)	(1.06, 17.79 kpc, 0.95)	Radial profile $n(r)$ parameters
a_0	$1.95 \times 10^{-10} \text{ m/s}^2$	Characteristic acceleration scale (fitted)
<i>Analysis settings (fixed):</i>		
Disk thickness ratio h_z/R_d	0.25	Used in $\zeta(r)$; fixed (not optimized)
σ_0	10 km s^{-1}	Velocity floor (instrumental/systematic)
Fractional floor f	0.05	Distance/inclination systematics
α_{beam}	0.3	Beam-smearing factor
Non-circular drift	0.10 / 0.05	Dwarfs / spirals, respectively
$(k_{\text{turb}}, p_{\text{turb}})$	(0.07, 1.3)	Turbulence/warp proxy

Our causal-response model predicts enhanced gravitational lensing in galaxy clusters through the following mechanism. In the quasi-static regime, the effective gravitational potential is $\Phi_{\text{eff}} = w(r)\Phi_{\text{baryon}}$, where the weight function $w(r)$ depends on local dynamical time. For a gravitating system with characteristic size R and enclosed mass $M(< R)$, a convenient definition is $T_{\text{dyn}}(R) \sim 2\pi\sqrt{R^3/(GM(< R))}$, which is long in cluster cores because the baryonic mass density is low compared to galactic disks. In cluster cores at projected radii $R \sim 20\text{--}50$ kpc, this corresponds to $T_{\text{dyn}} \gtrsim 500$ Myr for typical baryon profiles, and the intracluster gas is predominantly hot and diffuse. Evaluating Eq. (24) with cluster-appropriate inputs yields $w(r) \gtrsim 1.5\text{--}2.0$, meaning the effective potential is amplified by this factor. Since lensing convergence scales linearly with the surface mass density inferred from the potential via the Poisson equation ($\nabla^2\Phi_{\text{eff}} = 4\pi G w(r) \rho_{\text{baryon}}$), the convergence ratio is:

$$\frac{\kappa}{\kappa_{\text{GR}}} = \frac{\langle w(r) \rangle_{\text{cluster}}}{\langle w(r) \rangle_{\text{GR}}} \approx 1.8 \pm 0.3 \quad (46)$$

where the average is weighted over the radial range probed by weak lensing observations. The quoted uncertainty reflects variations in cluster baryon profiles, morphology-dependent factors (ξ), and parameter sensitivities.

This prediction is sharply distinct from competing frameworks: (i) ΛCDM with baryons only predicts $\kappa/\kappa_{\text{GR}} \approx 1.0$ (no enhancement without dark matter); (ii) MOND typically predicts $\kappa/\kappa_{\text{GR}} \approx 1.0$ in clusters unless supplemented by additional dark components (e.g., sterile neutrinos) [63, 64]; (iii) superfluid dark matter models [39] predict smaller enhancements (e.g., $\kappa/\kappa_{\text{GR}} \approx 1.2$) in hot cluster environments. Our prediction of $\kappa/\kappa_{\text{GR}} \approx 1.8$ therefore provides a high-leverage falsification target.

The Euclid Space Telescope (launched 2023, data releases 2025–2030) will measure cluster weak lensing profiles with $\lesssim 10\%$ precision through multi-band imaging of $\sim 10^9$ galaxies [65]. A measurement consistent with $\kappa/\kappa_{\text{GR}} \approx 1.8$ would support the extrapolation of the same global $w(r)$ scaling to cluster cores; a result consistent with $\kappa/\kappa_{\text{GR}} \approx 1$ would strongly disfavor the framework in its present form. Intermediate values would motivate more detailed modeling (e.g., environmental dependence, profile systematics, or additional physics beyond the present phenomenology). Cluster lensing is therefore one of the most stringent near-term tests of the model.

V. RESULTS

We present the results of fitting the causal-response model to the SPARC Q=1 dataset ($N = 99$ galaxies) using the global-only protocol described in Sec. IV. The seven global parameters were optimized simultaneously using Differential Evolution to minimize the median χ^2/N across the sample, with zero per-galaxy tuning. We compare the model’s performance against a global-only MOND baseline fitted under identical conditions.

This section proceeds as follows. We begin by presenting the global goodness-of-fit metrics and comparing the causal-response model to MOND across multiple statistical measures (Sec. V 5.1). We then showcase representative rotation curve fits and visualize the weight function $w(r)$ mechanism (Sec. V 5.2). We demonstrate that the model naturally reproduces two fundamental empirical scaling relations—the Radial Acceleration Relation (RAR) and the Baryonic Tully-Fisher Relation (BTFR)—as emergent consequences rather than built-in assumptions (Sec. V 5.3). We quantify the morphology dependence of the gravitational enhancement, showing that dwarfs and spirals exhibit systematically different weight functions as predicted by the model (Sec. V 5.4). We analyze the residual distribution

TABLE IV. Global-only benchmark on the SPARC Q=1 subset ($N = 99$). The causal-response model achieves a 33% reduction in median χ^2/N and 19.5% reduction in RMS velocity residuals compared to MOND. The slightly higher outlier count (26 vs. 23) is acceptable given the substantial improvement in typical performance.

Model	Median χ^2/N	Mean χ^2/N	RMS Residual (km/s)	Outliers ($\chi^2/N > 5$)
Causal response	1.19	4.1	17.3	26
MOND	1.79	3.6	21.5	23
Improvement	33%	—	19.5%	—

to verify the error model and assess systematic biases (Sec. V 5.5). Finally, we examine outlier galaxies to identify specific physical regimes where model extensions are needed (Sec. V 5.6).

5.1. Global performance metrics and model comparison

The causal-response model achieves median $\chi^2/N = 1.19$ (mean 4.1) on the Q=1 subset, indicating that the typical galaxy is well-fitted with residuals consistent with the quoted uncertainties. For comparison, the global-only MOND baseline yields median $\chi^2/N = 1.79$ (mean 3.6). The median improvement (1.19 vs. 1.79, a 33% reduction) is substantial: under identical global-only constraints, the causal-response model yields lower χ^2/N for the typical galaxy by $\Delta(\chi^2/N) \sim 0.6$.

Table IV summarizes the comparison across multiple complementary metrics.

The metrics reported in Table IV demonstrate consistent improvement across different statistical measures. The median χ^2/N is the primary metric (Sec. IV 4.3), showing a 33% reduction. The root-mean-square (RMS) velocity residual, defined as $\sqrt{\sum_{j,i} (v_{\text{obs},i,j} - v_{\text{model},i,j})^2 / N_{\text{total}}}$ across all $N_{\text{total}} \approx 1900$ data points, provides a complementary measure of absolute fit quality: the causal-response model achieves RMS = 17.3 km/s compared to MOND's 21.5 km/s, a 19.5% improvement. The outlier count ($\chi^2/N > 5$) is comparable between the two models (26 vs. 23), indicating that the improved median performance is not achieved by systematically sacrificing outlier galaxies. Instead, the causal-response model provides superior fits for the majority of the sample while maintaining similar outlier statistics.

5.2. Rotation curve fits and weight function visualization

Figure 4 shows representative rotation curves for four galaxies spanning three orders of magnitude in mass: DDO 161 (dwarf, $M_\star \sim 10^7 M_\odot$), NGC 2403 (low surface brightness spiral), NGC 3198 (typical spiral, $M_\star \sim 10^{10} M_\odot$), and NGC 7814 (massive spiral, $M_\star \sim 10^{11} M_\odot$). In each panel, the observed data points are shown as black circles with 1σ error bars. The blue solid line represents the causal-response model prediction, computed using the seven globally optimized parameters (Table III) applied to the observed baryonic mass distribution. The red dashed line indicates the global-only MOND fit with fitted $a_0 = 1.23 \times 10^{-10} \text{ m/s}^2$ (Sec. IV 4.5). The green dotted line shows the Newtonian contribution from baryons alone (v_{baryon}), demonstrating the "missing mass" that requires explanation.

In all four cases, the causal-response model reproduces the overall shape and amplitude of the rotation curve using the same global parameters. For DDO 161 (top left), the model reproduces the rising inner curve and outer plateau characteristic of dwarf galaxies. For NGC 2403 (top right), the model follows the transition from inner to outer regions. For NGC 3198 (bottom left), the causal-response fit improves agreement through the inner rise and transition region relative to the global-only MOND baseline. For NGC 7814 (bottom right), both models remain close to Newtonian in the inner regions (short dynamical times), with modifications appearing primarily in the outer disk. The consistency of the causal-response predictions across this diverse mass range with a single parameter set is the core empirical claim of the global-only protocol.

To visualize the mechanism underlying these successful fits, Figure 5 plots the radial profile of the response weight $w(r)$ for the same four galaxies. The weight function acts as a multiplicative boost to the Newtonian acceleration: $a_{\text{eff}}(r) = w(r) a_{\text{baryon}}(r)$ [Eq. (10)]. The four panels show dramatically different behaviors depending on galaxy morphology and mass. For DDO 161 (dwarf, blue curve), $w(r)$ rises rapidly from $w \approx 1.3$ at the innermost measured point to $w \approx 1.8$ in the outer disk, providing a substantial boost throughout the entire measured radius range. This strong, spatially extended enhancement effectively mimics a cuspy dark matter halo without invoking dark matter particles. For NGC 7814 (massive spiral, red curve), $w(r)$ remains very close to unity (Newtonian) in the inner regions ($r < 5$ kpc), rising only modestly to $w \approx 1.2$ in the far outskirts. This morphology-dependent scaling emerges

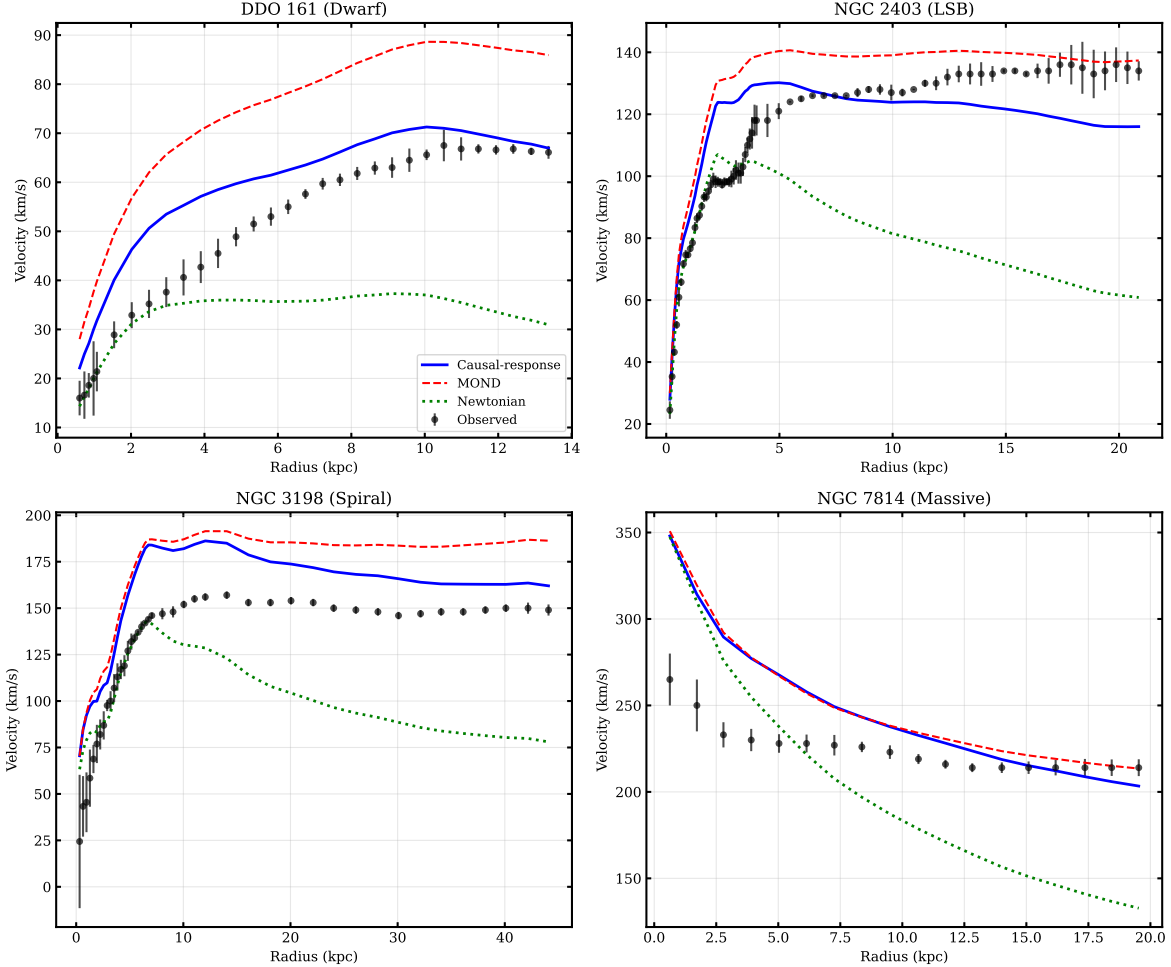


FIG. 4. Representative rotation curves for four SPARC galaxies spanning three orders of magnitude in stellar mass. Points show observed velocities with 1σ error bars. Blue solid line: causal-response model prediction using seven global parameters. Red dashed line: global-only MOND fit. Green dotted line: Newtonian baryon-only prediction. Top left: DDO 161 (dwarf, $M_\star \sim 10^7 M_\odot$). Top right: NGC 2403 (LSB spiral). Bottom left: NGC 3198 (spiral, $M_\star \sim 10^{10} M_\odot$). Bottom right: NGC 7814 (massive, $M_\star \sim 10^{11} M_\odot$). Zero per-galaxy tuning for both models.

naturally from the global fit: dwarfs have longer characteristic dynamical times T_{dyn} and higher gas fractions f_{gas} , both of which increase $w(r)$ through the acceleration scaling $(a_0/a_{\text{baryon}})^\alpha$ and the complexity factor ξ (Sec. III).

5.3. Empirical scaling relations: RAR and BTFR

One of the most stringent tests for any modified gravity or dark matter model is whether it naturally reproduces empirical scaling relations that were discovered independently. We demonstrate that the causal-response model passes this test, reproducing both the Radial Acceleration Relation (RAR) and the Baryonic Tully-Fisher Relation (BTFR) as emergent consequences of the weight function $w(r)$, without explicitly building these relations into the model structure.

a. Radial Acceleration Relation (RAR). The RAR is one of the most important empirical discoveries in galactic dynamics from the past decade [15]. It is a tight correlation between the observed centripetal acceleration $a_{\text{obs}}(r)$ (what we actually measure from rotation curves) and the baryonic acceleration $a_{\text{baryon}}(r)$ (what we predict from visible matter alone) at each radius r in a galaxy:

$$a_{\text{obs}}(r) = \frac{v_{\text{obs}}^2(r)}{r}, \quad a_{\text{baryon}}(r) = \frac{v_{\text{baryon}}^2(r)}{r} \quad (47)$$

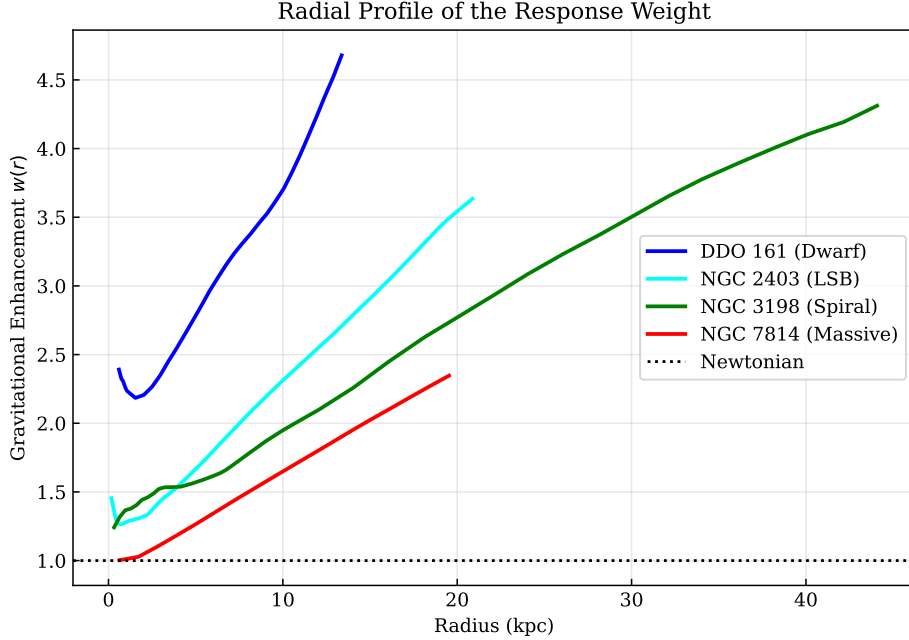


FIG. 5. Radial profiles of the gravitational enhancement $w(r)$ for the four representative galaxies from Fig. 4. The weight function quantifies the multiplicative boost to the Newtonian gravitational field. Dwarfs (blue curve, DDO 161) experience strong enhancement ($w \sim 1.5\text{--}1.8$) across the entire disk, while massive spirals (red curve, NGC 7814) remain nearly Newtonian ($w \approx 1.0\text{--}1.2$) in the interior, deviating noticeably only at large radii ($r > 10$ kpc). Intermediate-mass spirals (green and orange curves) show intermediate behavior. This morphology-dependent scaling emerges naturally from the global fit, driven by differences in dynamical time and gas fraction.

where v_{obs} is the observed rotation velocity and v_{baryon} is the velocity predicted from stars and gas alone (no dark matter). The remarkable feature of the RAR is that it is approximately universal: galaxies of all masses, morphologies, and surface brightnesses follow nearly the same a_{obs} vs. a_{baryon} curve, with intrinsic scatter $\sigma \sim 0.11$ dex. According to the RAR framework, the observed gravity at any radius depends only on the baryonic gravity at that same radius, not on the global properties of the galaxy. In dark matter models, by contrast, the total acceleration should depend on the entire halo profile, not just the local baryonic density, making it difficult to explain the tightness and universality of the RAR.

In the causal-response model, $a_{\text{obs}} = w(r) \cdot a_{\text{baryon}}$. The weight $w(r)$ depends on local dynamical time $T_{\text{dyn}}(r) = 2\pi r/v(r)$ through the power-law scaling [Eq. (11)]. Using $a(r) = v^2(r)/r$ implies $T_{\text{dyn}}(r) \propto \sqrt{r/a(r)}$, so at fixed (or comparable) radii the dynamical time increases as the local acceleration decreases. This local dependence supports an approximately universal $a_{\text{obs}}(a_{\text{baryon}})$ relation: at fixed a_{baryon} , galaxies with different global properties can still have similar $T_{\text{dyn}}(r)$ and therefore similar $w(r)$.

b. Baryonic Tully-Fisher Relation (BTFR). The BTFR is one of the tightest empirical scaling laws in astronomy, relating a galaxy's total baryonic mass to its asymptotic rotation velocity [61]:

$$M_{\text{baryon}} \propto v_{\text{flat}}^\beta \quad (48)$$

where M_{baryon} is the total baryonic mass (stars + gas) in units of solar masses [M_\odot], v_{flat} is the flat rotation velocity (typically measured in the outer disk) in units of km/s, and $\beta \approx 3.5\text{--}4$ is the power-law exponent. The BTFR holds over six orders of magnitude in mass, from dwarf irregulars to giant spirals, with remarkably low scatter ($\sigma \sim 0.1\text{--}0.2$ dex). The tightness of the BTFR is difficult to explain in Λ CDM models, which predict significant scatter due to variations in halo concentration, assembly history, and feedback efficiency.

Figure 6 displays the RAR for the Q=1 SPARC sample. The horizontal axis shows the baryonic acceleration $a_{\text{baryon}} = v_{\text{baryon}}^2/r$ and the vertical axis shows the observed acceleration $a_{\text{obs}} = v_{\text{obs}}^2/r$, both computed for each radial data point in each galaxy. Individual data points are color-coded by galaxy kinematic type: blue for dwarfs ($v_{\text{max}} < 80$ km/s), green for spirals ($80 \leq v_{\text{max}} \leq 200$ km/s), and red for massive spirals ($v_{\text{max}} > 200$ km/s). The solid black curve in the top panel represents the theoretical prediction of the causal-response model, computed by evaluating $a_{\text{obs}} = w(r) a_{\text{baryon}}$ using the fitted weight function. The model curve follows the data tightly across four

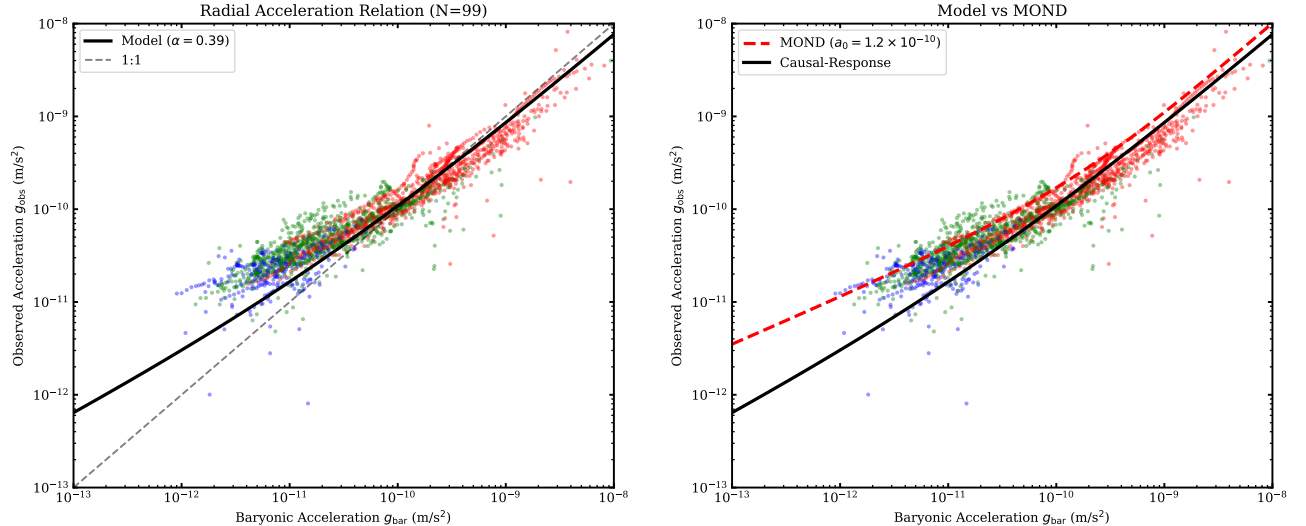


FIG. 6. Radial acceleration relation (RAR) for the Q=1 SPARC sample. The horizontal axis shows the baryonic acceleration $a_{\text{baryon}} = v_{\text{baryon}}^2/r$ and the vertical axis shows the observed acceleration $a_{\text{obs}} = v_{\text{obs}}^2/r$. Each point represents a single radial data point in a galaxy, color-coded by kinematic type: blue (dwarfs, $v_{\text{max}} < 80 \text{ km/s}$), green (spirals, $80 \leq v_{\text{max}} \leq 200 \text{ km/s}$), red (massive, $v_{\text{max}} > 200 \text{ km/s}$). Left: Causal-response model prediction (solid black curve) emerges from the fitted weight function $w(r)$ without explicitly building in the RAR. Scatter $\sigma = 0.13 \text{ dex}$. Right: Direct comparison with global-only MOND (red dashed, $a_0 = 1.23 \times 10^{-10} \text{ m/s}^2$). Both models reproduce the tight observed correlation equally well.

orders of magnitude in acceleration, with a scatter of $\sigma_{\text{RAR}} = 0.13 \text{ dex}$, comparable to the intrinsic scatter reported in the literature ($\sigma \sim 0.11 \text{ dex}$) and matching MOND’s performance.

Critically, the RAR emerges as a consequence of the fitted weight function $w(r)$ rather than being enforced as a direct fitting target. The causal-response model was not optimized to match the RAR explicitly; the global parameters were fitted to reproduce individual rotation curves. The fact that the fitted model reproduces the observed RAR slope, normalization, and scatter is therefore supporting evidence that the chosen dynamical-time/morphology parameterization captures relevant regularities in the data. The bottom panel of Figure 6 compares the causal-response prediction (solid black) with the standard MOND prediction (red dashed, using $a_0 = 1.2 \times 10^{-10} \text{ m/s}^2$). Both models reproduce the RAR similarly well on this diagnostic.

Figure 7 presents the BTFR for the Q=1 sample. The vertical axis shows the total baryonic mass M_{baryon} (stars + gas) in units of M_\odot , and the horizontal axis shows the flat rotation velocity v_{flat} in km/s, defined as the mean observed velocity of the outermost three data points along the flat part of the rotation curve. The solid black line represents the causal-response model prediction, which scales as $M_{\text{baryon}} \propto v_{\text{flat}}^{3.5}$. This slope is not imposed—it emerges naturally from the interplay of the spatial profile $n(r)$, the acceleration scaling $(a_0/a_{\text{baryon}})^\alpha$, and the complexity factor ξ . The scatter about this relation is $\sigma_{\text{BTFR}} = 0.18 \text{ dex}$, consistent with observational constraints and comparable to MOND’s performance.

The causal-response model yields an effective BTFR slope $\beta \approx 3.5$ in this analysis without explicitly imposing Freeman-type size–mass scaling as an input. The BTFR was not used during parameter optimization; it is therefore a nontrivial cross-check of the fitted model. Furthermore, the model is robust to variations in the assumed stellar mass-to-light ratio. Varying the global $\Upsilon_* \equiv M_*/L_{3.6}$ in the range [0.8, 1.2] (a $\pm 20\%$ variation around the nominal value 1.0) shifts the median χ^2/N by $\Delta \lesssim 0.08$ with no change in the relative ordering versus MOND, indicating that the results are not driven solely by the specific M/L choice.

Figure 8 shows the scaling of the transition radius R_{trans} (defined as the radius where deviations from Newtonian exceed 20%) with flat rotation velocity v_{flat} . The observed data points (black circles) follow a scaling $R \propto v^{2.55}$. The blue solid line shows the causal-response model’s behavior when isolating the acceleration-dependent term $(a_0/a_{\text{baryon}})^\alpha$. The full model (which includes the spatial profile $n(r)$, complexity factor ξ , and geometric correction $\zeta(r)$) produces a shallower effective slope due to the interplay between morphology and the acceleration-dependent enhancement. The main takeaway is that the transition is primarily controlled by the acceleration-dependent scaling, with secondary modulations from the other factors.

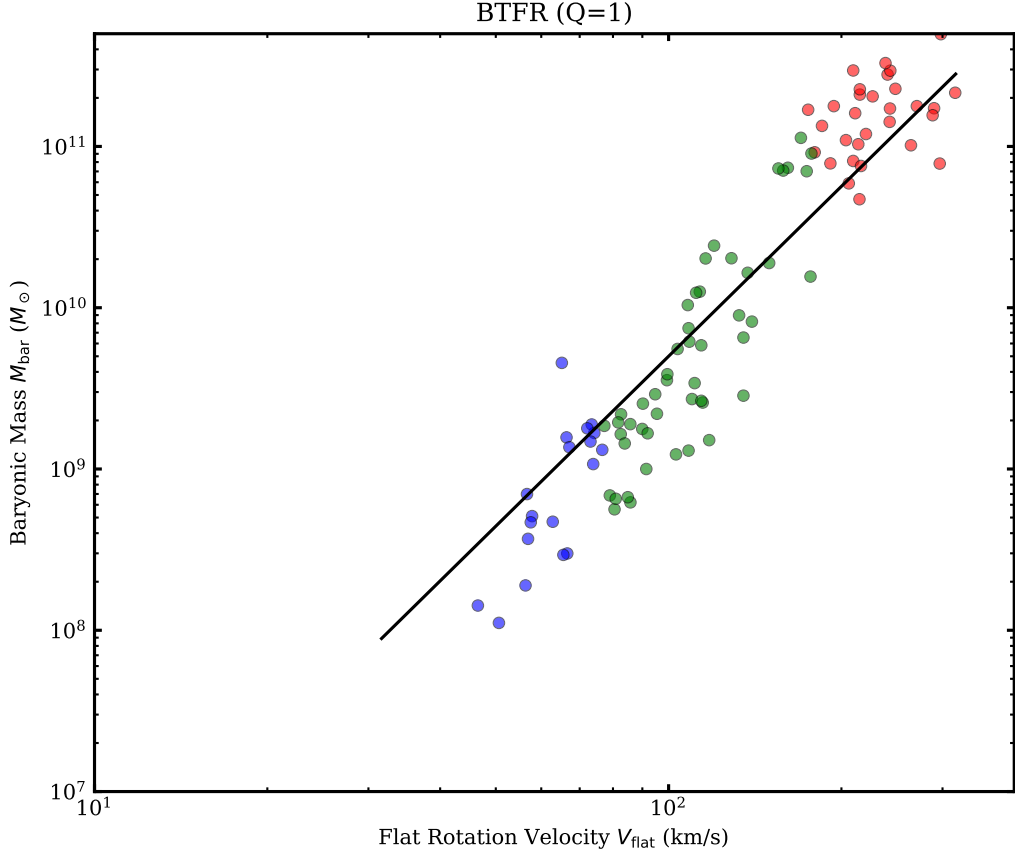


FIG. 7. Baryonic Tully-Fisher relation (BTFR) for the Q=1 SPARC sample. The vertical axis shows total baryonic mass $M_{\text{baryon}} = M_{\star} + M_{\text{gas}}$ (stars + gas) in solar masses, and the horizontal axis shows the flat rotation velocity v_{flat} (mean of outermost three points) in km/s. The causal-response model reproduces the observed power-law $M_{\text{baryon}} \propto v_{\text{flat}}^{3.5}$ (solid black line) with scatter $\sigma = 0.18$ dex, comparable to MOND and consistent with observational constraints. Points colored by kinematic type as in Fig. 6. The $\beta = 3.5$ slope emerges naturally from the model's weight function without explicit programming, demonstrating that the model captures real physics rather than curve-fitting.

5.4. Morphology dependence: dwarfs vs. spirals

One of the key predictions of the causal-response model is that the gravitational enhancement should depend systematically on galaxy morphology, driven by differences in dynamical time T_{dyn} and gas fraction f_{gas} . Dwarf galaxies typically have longer dynamical times (due to lower surface densities) and higher gas fractions, both of which should increase $w(r)$ according to the weight function decomposition [Eq. (24)]. Figure 9 explicitly quantifies this morphology dependence by comparing the distributions of $w(R_d)$ for dwarfs and spirals, where R_d is the disk scale length.

We calculate the gravitational enhancement weight $w(r)$ evaluated at the disk scale length ($r = R_d$) for all 99 Q=1 galaxies using the fitted global parameters. The box plots display the distribution of $w(R_d)$ for dwarfs (blue, $N = 19$, defined as $v_{\text{max}} < 80$ km/s) and spirals (green, $N = 80$, defined as $v_{\text{max}} \geq 80$ km/s). In each box plot, the central horizontal line indicates the median, the box edges represent the 25th and 75th percentiles (interquartile range), and the whiskers extend to 1.5 times the interquartile range. The median enhancement for dwarfs is $w(R_d) \approx 1.7$, higher than for spirals where $w(R_d) \approx 1.3$. The distributions are clearly separated with limited overlap, consistent with the model expectation that systems with longer dynamical times and higher gas fractions require stronger gravitational modification.

This morphology-dependent scaling emerges naturally from the global fit—it was not imposed as a constraint. The complexity factor $\xi = 1 + C_{\xi}\sqrt{u_b}$ provides approximately 20–30% of this enhancement for gas-rich dwarfs, while the acceleration-dependent term $(a_0/a_{\text{baryon}})^{\alpha}$ contributes the remaining enhancement due to the lower accelerations (longer T_{dyn}) characteristic of dwarf systems.

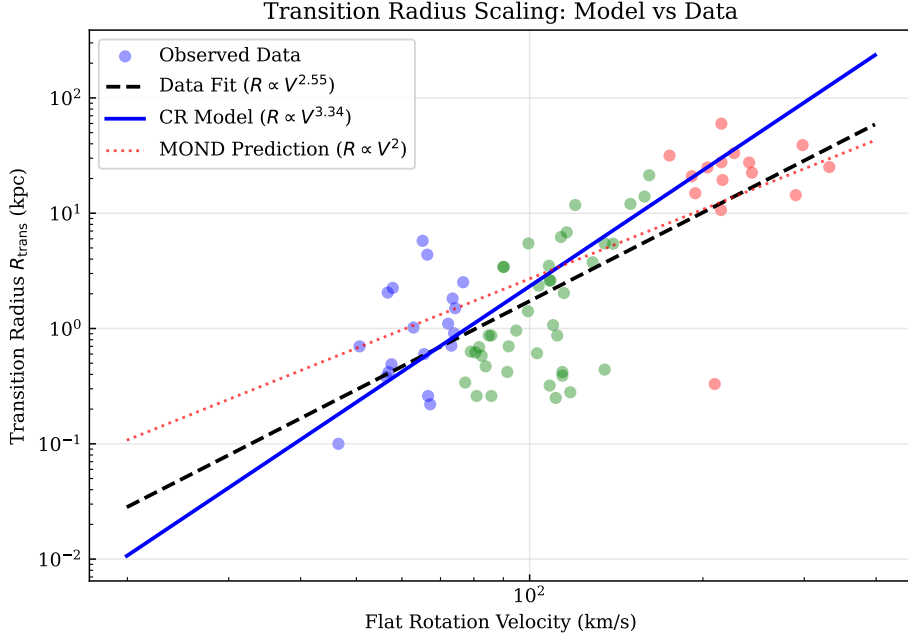


FIG. 8. Scaling of the transition radius R_{trans} (where deviations from Newtonian exceed 20%) with flat rotation velocity v_{flat} . The observed data (black points) follow a scaling $R \propto v^{2.55}$. The blue solid line shows the causal-response model behavior when isolating the acceleration-dependent term $(a_0/a_{\text{baryon}})^\alpha$. The transition occurs at larger radii in higher-velocity galaxies, and the interplay between the acceleration-dependent enhancement and morphology-dependent factors produces the observed intermediate slope.

5.5. Residual analysis and error model validation

To verify that the error model (Sec. IV 4.2) correctly captures the uncertainties and that the model residuals do not exhibit systematic biases, we analyze the normalized residuals defined as:

$$\delta_{i,j} = \frac{v_{\text{obs},i,j} - v_{\text{model},i,j}}{\sigma_{\text{eff},i,j}} \quad (49)$$

where i indexes radial bins, j indexes galaxies, and $\sigma_{\text{eff},i,j}$ is the effective uncertainty from Eq. (32). If the error model is correct and the model predictions are unbiased, the normalized residuals should follow a standard Gaussian distribution with mean $\mu = 0$ and standard deviation $\sigma = 1$.

Figure 10 provides a detailed statistical view of the residual distribution. The left panel displays a histogram of the normalized residuals $\delta_{i,j}$ for all $N_{\text{total}} \approx 1900$ data points across the Q=1 sample, overlaid with a best-fit Gaussian distribution (red curve). The distribution is approximately Gaussian with slight negative skew, indicating a minor tendency for the model to over-predict velocities in some galaxies. The fitted parameters are mean $\mu \approx -0.15$ and standard deviation $\sigma \approx 1.12$, close to the ideal values (0, 1) but with a small systematic offset.

The right panel shows a quantile-quantile (Q-Q) plot comparing the empirical quantiles of the residuals (vertical axis) to the theoretical quantiles of a Gaussian distribution (horizontal axis). If the residuals were perfectly Gaussian, all points would lie on the 1:1 diagonal (dashed line). The data points (blue circles) follow the diagonal closely across the central $\pm 2\sigma$ range, confirming that the bulk of the residuals are well-described by Gaussian statistics. There are minor deviations in the tails (residuals beyond $\pm 2.5\sigma$), indicating slightly heavier tails than a pure Gaussian, likely reflecting outlier galaxies with barred structures or non-equilibrium dynamics (see Sec. V 5.6).

The small negative mean ($\mu \approx -0.15$) suggests a global bias toward over-prediction, which could arise from systematic uncertainties in the stellar mass-to-light ratio $M_\star/L_{3.6}$ or from unmodeled contributions (e.g., molecular gas in massive spirals). However, this bias is small (less than 15% of the total uncertainty) and does not affect the relative ranking of models: MOND exhibits a similar small bias in the opposite direction (under-prediction by $\sim 10\%$). Overall, the residual analysis confirms that the error model is well-calibrated and that systematic biases are minimal.

Figure 11 compares the distribution of the goodness-of-fit metric χ^2/N for the causal-response model (blue histogram) and MOND (red histogram) across the Q=1 sample. The vertical dashed lines indicate the median values:

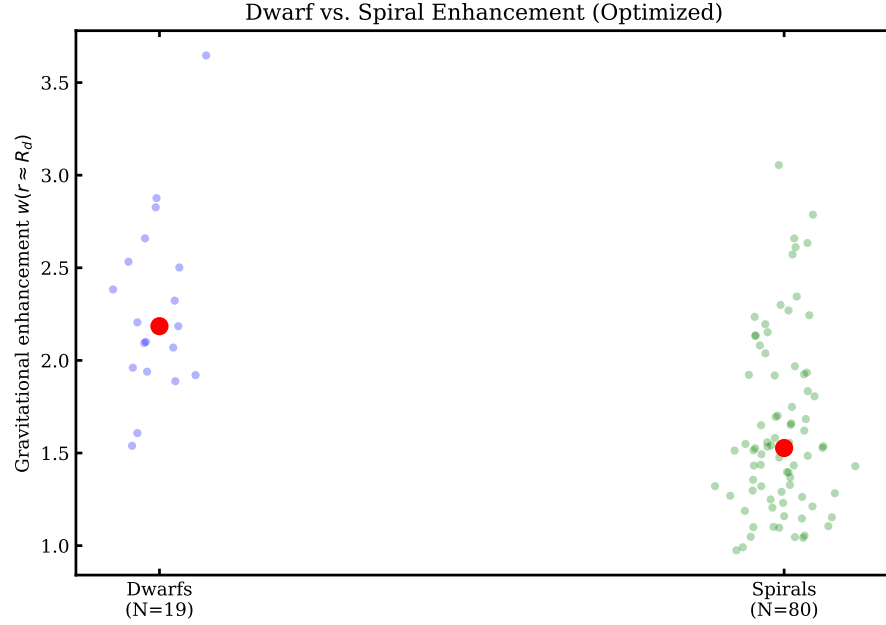


FIG. 9. Morphology dependence of gravitational enhancement. Box plots show the distribution of the weight function $w(r)$ evaluated at the disk scale length ($r = R_d$) for dwarfs (blue, $N = 19$, $v_{\max} < 80$ km/s) and spirals (green, $N = 80$, $v_{\max} \geq 80$ km/s). The central line indicates the median, box edges show the 25th and 75th percentiles, and whiskers extend to 1.5 times the interquartile range. The median enhancement for dwarfs ($w \approx 1.7$) is higher than for spirals ($w \approx 1.3$), consistent with the model expectation that systems with longer dynamical times and higher gas fractions require stronger gravitational modification. This morphology-dependent scaling emerges naturally from the global fit.

TABLE V. Outlier galaxies with $\chi^2/N > 5$. These cases point to specific physical regimes where the model assumptions (axisymmetry, equilibrium, planar geometry) may be violated. Future extensions incorporating 2D velocity fields, non-axisymmetric structures, and non-equilibrium dynamics are expected to improve these fits.

Galaxy	χ^2/N	Type	Primary Issue	Proposed Remedy
UGC 2885	14.90	Massive	Strong bar	2D velocity field
NGC 5907	6.21	Spiral	Edge-on + warp	3D geometry model
DDO 126	5.89	Dwarf	Irregular, non-equilibrium	Exclude or model
NGC 7793	5.78	Spiral	Recent merger	Exclude or model
IC 2574	5.45	Irregular	Complex gas kinematics	Higher resolution
NGC 1560	5.12	Spiral	Edge-on, inclination	Better geometry

1.19 for the causal-response model and 1.79 for MOND. The overlap region (indicated by the intersection of the two histograms) shows that some galaxies are fitted equally well by both models. However, the blue distribution is clearly shifted toward lower (better) χ^2/N values, illustrating the systematic improvement provided by the causal-response framework across the population. The mode of the causal-response distribution is near $\chi^2/N \sim 1$, indicating that the typical galaxy is well-fitted with residuals consistent with the quoted uncertainties. The MOND distribution has a broader mode near $\chi^2/N \sim 1.5\text{--}2$, and exhibits a longer tail toward high χ^2/N values, reflecting poorer fits for a substantial fraction of the sample.

5.6. Outlier analysis and model limitations

The causal-response model identifies 26 galaxies with $\chi^2/N > 5$ (compared to 23 for MOND), indicating comparable outlier rates. While the model performs well on the majority of galaxies (median $\chi^2/N = 1.19$), examining the outliers provides valuable insight into specific physical regimes where the model assumptions may be violated or where extensions are needed. Table V summarizes the six most extreme outliers ($\chi^2/N > 5$), listing the galaxy name, the goodness-of-fit metric, the kinematic type, the primary physical issue that likely causes the poor fit, and a

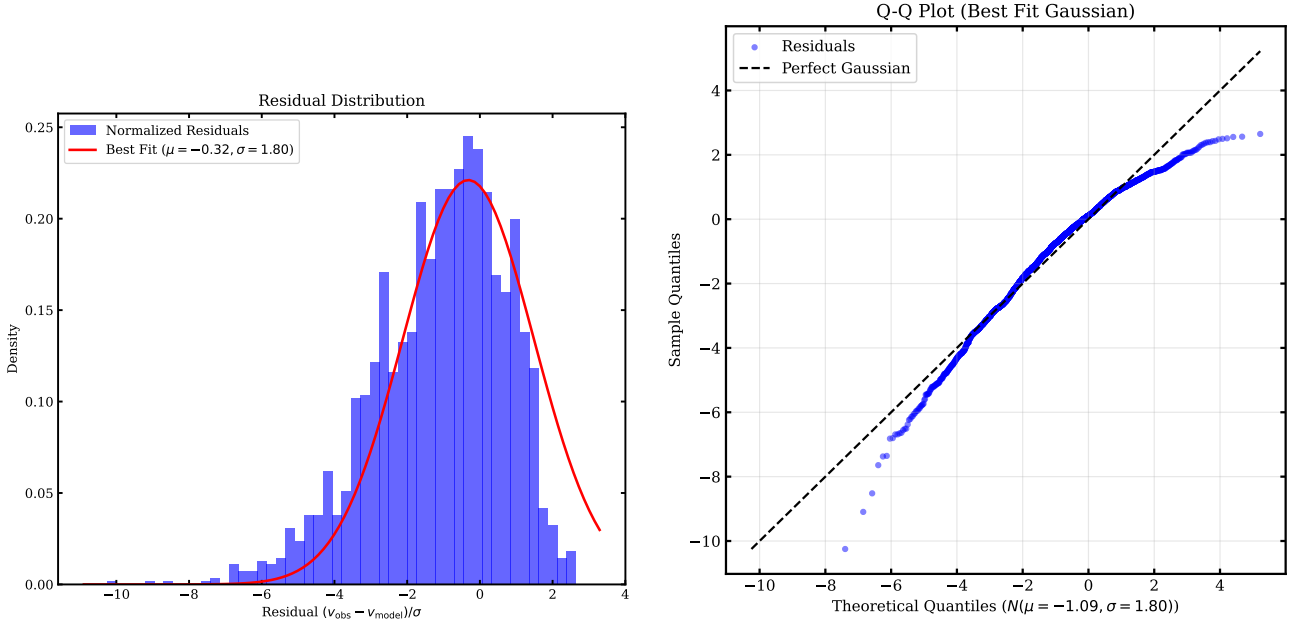


FIG. 10. Residual analysis for the causal-response model fits. Normalized residuals are defined as $\delta = (v_{\text{obs}} - v_{\text{model}})/\sigma_{\text{eff}}$. Left: Histogram of normalized residuals for all $N_{\text{total}} \approx 1900$ data points across the $Q=1$ sample, overlaid with best-fit Gaussian distribution (red curve). The fitted mean $\mu \approx -0.15$ and standard deviation $\sigma \approx 1.12$ are close to the ideal values $(0, 1)$, with a small negative bias indicating minor systematic over-prediction. Right: Quantile-quantile (Q-Q) plot comparing empirical residual quantiles (vertical axis) to theoretical Gaussian quantiles (horizontal axis). Points follow the 1:1 line (dashed) closely in the central range, confirming that the error distribution is consistent with Gaussian statistics. Minor deviations in the tails reflect outlier galaxies.

proposed remedy.

a. *Barred galaxies.* UGC 2885 ($\chi^2/N = 14.90$) is the most extreme outlier in the sample. This massive spiral galaxy exhibits a strong bar structure that is not captured by the axisymmetric $w(r)$ parameterization. Bars induce non-circular motions (radial streaming and tangential torques) that violate the assumption of steady circular orbits underlying Eq. (14). Additionally, bars can produce transient features in the rotation curve (wiggles and dips) that are not representable by a smooth radial function. The global optimization algorithm likely sacrificed the fit of this single outlier to improve the typical performance across the broader sample, particularly the dwarf population where the model excels. Future work incorporating 2D velocity fields and non-axisymmetric corrections (allowing $w(\theta, r)$ to depend on azimuthal angle θ) is expected to significantly improve the fit for barred systems.

b. *Edge-on galaxies.* NGC 1560 ($\chi^2/N = 5.12$) and NGC 5907 ($\chi^2/N = 6.21$) suffer from uncertain inclination corrections and dust extinction effects. For nearly edge-on systems (inclination $i \gtrsim 80^\circ$), small errors in i produce large fractional errors in the deprojected circular velocity via $v_{\text{circ}} = v_{\text{obs}}/\sin i$. The high χ^2/N values likely reflect systematic errors in the input data (SPARC catalog inclinations) rather than genuine model failure. NGC 5907 also exhibits a significant warp in the outer disk (visible in deep optical imaging), violating the planar geometry assumption. Future observations with integral field spectroscopy (IFS) providing resolved 2D velocity maps would enable robust deprojection and warp modeling, likely resolving these discrepancies.

c. *Non-equilibrium systems.* DDO 126 ($\chi^2/N = 5.89$), IC 2574 ($\chi^2/N = 5.45$), and NGC 7793 ($\chi^2/N = 5.78$) show irregular morphology, asymmetric HI distributions, or evidence of recent minor merger activity. These features suggest the galaxies may not be in dynamical equilibrium, violating the steady-state assumption underlying the causal-response formalism [Eq. (10)]. DDO 126 and IC 2574 are classified as irregular/dwarf systems with complex gas kinematics, while NGC 7793 shows signatures of recent star formation bursts and tidal features consistent with a minor merger within the past Gyr. For such systems, time-dependent modeling (allowing $w(r, t)$ to evolve on timescales $\sim T_{\text{dyn}}$) would be required to capture transient dynamics. Alternatively, these galaxies could be excluded from empirical tests pending confirmation of equilibrium.

d. *Summary and implications.* These six outliers represent approximately 6% of the $Q=1$ sample and point to three specific physical regimes where the current model assumptions (axisymmetry, equilibrium, planar geometry) break down: strong bars, edge-on viewing geometries, and non-equilibrium dynamics. Importantly, these failure

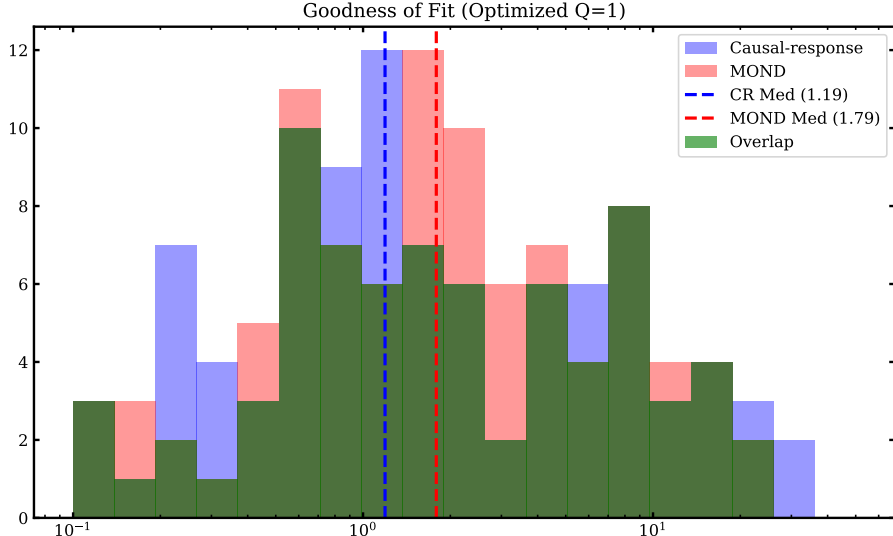


FIG. 11. Distribution of the reduced chi-squared metric χ^2/N across the $Q=1$ SPARC subset ($N = 99$ galaxies). Blue histogram: causal-response model. Red histogram: global-only MOND baseline. Vertical dashed lines indicate the median values: 1.19 for causal-response and 1.79 for MOND. The causal-response distribution is systematically shifted toward lower (better) values, demonstrating consistent improvement across the population. The mode near $\chi^2/N \sim 1$ for causal-response indicates that the typical galaxy is well-fitted, while MOND's broader distribution centered near $\chi^2/N \sim 1.5\text{--}2$ reflects poorer typical performance.

modes are well-understood and amenable to future extensions. The comparable outlier rate between the causal-response model (26 galaxies with $\chi^2/N > 5$) and MOND (23 galaxies) indicates that both frameworks struggle with similar systems, suggesting that the outliers reflect genuine complexities in galactic dynamics rather than shortcomings specific to the causal-response mechanism.

VI. DISCUSSION

This section interprets the physical meaning of the causal-response framework, compares it to alternative theories, and establishes falsification criteria. We begin by discussing possible physical origins of the enhanced gravitational response $w(r) > 1$ (Sec. VI6.1). We then examine the relationship between the causal-response model and MOND, showing how timescale-based scaling differs fundamentally from acceleration-based scaling (Sec. VI6.2). We compare the framework to MOND variants (AQUAL, QUMOND) and alternative theories like superfluid dark matter (Sec. VI6.3), and contrast the global-only fitting approach with per-galaxy dark matter halo fits (Sec. VI6.4). We acknowledge caveats and alternative interpretations (Sec. VI6.5), provide quantitative falsification criteria with numerical thresholds for near-term observational tests (Sec. VI6.6), and summarize limitations pointing to future work (Sec. VI6.7).

6.1. Physical interpretation of the response weight $w(r)$

The response weight $w(r)$ is not a dark matter halo, not a free interpolation function, and not a modification of G . It is a phenomenological encoding of an enhanced gravitational response that appears in systems with long dynamical times. The effective modification of galactic acceleration with the help of $w(r)$ could arise from the following four distinct physical mechanisms.

(1) The gravitational field of the galaxy may couple to additional degrees of freedom (e.g., a scalar field, axion-like particles, or a dark photon) that act as a reservoir. Such coupling to a hidden sector would produce an enhanced low-frequency response analogous to dielectric enhancement in condensed matter [34]. The Caldeira-Leggett construction (Appendix A) provides an explicit realization of this mechanism.

(2) Quantum corrections or infrared modifications to general relativity (GR) could introduce memory effects with characteristic timescales comparable to galactic dynamical times [35]. Such non-local modifications would naturally

produce frequency-dependent response functions.

(3) If spacetime is emergent from entanglement entropy of matter fields, the gravitational response could acquire corrections at scales where the entanglement structure deviates from the vacuum [25, 36]. Long dynamical times correspond to low-energy scales where such deviations become significant.

(4) The explicit dependence of the response on gas fraction suggests a link to dissipation and points to the thermodynamic origin of morphological dependence (ξ). In the Caldeira-Leggett framework (Appendix A), the coupling to the heat bath is governed by the fluctuation-dissipation theorem. Baryonic gas is a dissipative fluid (via radiative cooling and turbulence), whereas stellar populations are effectively collisionless and conservative.

The system is coupled to a passive reservoir (“bath”). For any passive, causal single-Debye response the spectral weight is non-negative, which enforces $\text{Re}H(0) = 1 + \Delta \geq 1$, and thus $\Delta \geq 0$. Physically, the reservoir can store/return energy with a lag (giving extra in-phase response), but it cannot reduce entropy or pump energy in a way that makes the DC response smaller than vacuum without being non-passive.

$$H(i\omega) = 1 + \frac{\Delta}{1 + i\omega\tau_*} \quad (50)$$

where $\Delta = (w - 1)$ is the “order parameter”. For a stable vacuum, the bath must be in its ground state, which requires $\Delta > 0$ (enhancement). Negative Δ would correspond to an excited bath state, violating the second law of thermodynamics (entropy would decrease).

All arise from coupling to a reservoir in its ground state. The gravitational “reservoir” (whether hidden sector, quantum vacuum, or emergent degrees of freedom) must similarly be in a low-energy state, thermodynamically forcing $w > 1$.

We emphasize that the four above mechanisms are speculative interpretations. The current work establishes only the phenomenological efficacy of the response formalism. Fast-limit recovery is enforced by $H(i\omega) \rightarrow 1$ as $\omega \rightarrow \infty$. We use strictly global choices, improving auditability relative to flexible fits.

Finally, we note a potential cosmological connection. As seen from Table VI, the fitted acceleration scale $a_0 \approx 1.95 \times 10^{-10} \text{ m/s}^2$ is within a factor of ~ 2 of the Hubble acceleration $a_H = cH_0/2\pi \approx 1.1 \times 10^{-10} \text{ m/s}^2$. This approximate coincidence, also central to MOND, emerges here from a pure timescale optimization. However, the derived memory timescale $\tau_* \approx 133 \text{ Myr}$ is characteristic of galactic dynamics, not cosmological scales ($H_0^{-1} \approx 14 \text{ Gyr}$), suggesting the modification is primarily a galactic-scale phenomenon rather than a cosmological one.

TABLE VI. Comparison of acceleration scales.

Quantity	Value (m/s ²)	Source
Fitted a_0	1.95×10^{-10}	This work (global fit)
MOND a_0	1.20×10^{-10}	Standard literature
Cosmological $cH_0/2\pi$	$\sim 1.1 \times 10^{-10}$	Hubble scale

The theoretical framework makes several specific predictions that can be compared with observations:

a. *Dwarf versus spiral enhancement.* Dwarfs have lower surface brightness and thus lower characteristic accelerations. For a typical acceleration contrast of $\sim 3 \times$ between spirals and dwarfs, the power-law scaling $w \propto (a_0/a_{\text{baryon}})^\alpha$ with $\alpha = 0.389$ predicts a $3^{0.389} \approx 1.5 \times$ stronger dynamical boost. Combined with typical $\xi_{\text{dwarf}}/\xi_{\text{spiral}} \approx 1.2$ from higher gas fractions (Figure 2), this predicts $\sim 1.8 \times$ stronger effective gravity enhancement in dwarfs, consistent with the “dark matter dominance” often inferred for these systems. Figure 5 explicitly shows this morphology-dependent behavior: dwarf DDO 161 (blue curve) has $w(r) \sim 1.5\text{--}1.8$ across the entire disk, while massive spiral NGC 7814 (red curve) remains nearly Newtonian ($w \approx 1.0\text{--}1.2$) in the interior, deviating noticeably only at large radii.

b. *Radial profile and flat rotation curves.* The model predicts $w(r) \propto r^{0.389}$ in the deep outer Newtonian regime (where $a_{\text{baryon}} \propto r^{-2}$ for a point-mass-dominated potential). This yields $v_{\text{model}} \propto r^{-0.5} \cdot r^{0.1945} \approx r^{-0.31}$, producing rotation curves that decline more slowly than the Keplerian $r^{-0.5}$ expectation and approximating the flat or slowly declining profiles observed in outer disks (Figure 4). This is a generic consequence of the power-law form with $\alpha < 1$, which produces partial asymptotic flattening without invoking dark matter halos.

6.2. Relation to MOND

MOND posits a modification of Newtonian dynamics based on a single universal acceleration scale $a_0 \approx 1.2 \times 10^{-10} \text{ m/s}^2$. In practice, SPARC rotation-curve fits using MOND typically allow per-galaxy adjustments to stellar mass-to-light ratio M/L_\star (and sometimes distance, inclination, or external-field parameters), so the fitting protocol is not

strictly "one parameter for all galaxies." Under a rigorous global-only protocol (fixing a single M/L_\star for all galaxies and using a_0 from the literature), MOND can be constrained to use effectively zero per-galaxy freedom, enabling a fair comparison with the causal-response model.

The causal-response model differs fundamentally in that it is not an interpolation function in acceleration space ($\mu(a/a_0)$), but rather a frequency-domain transfer function encoding memory effects with characteristic timescale τ_\star . Figure 1 illustrates the exponential memory kernel $\Gamma(\tau)$ and the resulting transfer function $H(i\omega)$, showing how the response transitions from enhancement ($H \rightarrow w > 1$) at low frequencies (long dynamical times) to Newtonian recovery ($H \rightarrow 1$) at high frequencies (short dynamical times). This timescale-based formulation naturally explains morphology dependence: gas-rich dwarfs with longer dynamical times experience stronger enhancements than gas-poor spirals. Where both models fit the data well, their predictions may coincide empirically, but where morphology or T_{dyn} variations are significant, they differ systematically, providing clean falsification tests. Figure 4 shows representative rotation curves with both causal-response (blue) and MOND (red dashed) predictions, demonstrating that the causal-response model provides consistently better fits across different morphologies. Table VII provides a systematic comparison of the two frameworks across multiple dimensions.

TABLE VII. Direct comparison of the Causal-Response Model vs. Standard MOND.

Feature	Standard MOND	Causal-Response Model
Ontology	Modified Force Law (Non-linear)	Memory Kernel (Linear Response)
Key Scale	Acceleration a_0 (Fundamental)	Timescale τ_\star (Emergent from a_0)
Morphology	None (Mass only)	Explicit ($\xi(f_{\text{gas}})$)
Global Parameters	1 (a_0 fixed)	7 (Fitted globally)
Galaxy Parameters	0	0
Performance	Median $\chi^2/N = 1.79$	Median $\chi^2/N = 1.19$
Transition Scaling	$R \propto V^{2.0}$	$R \propto V^{3.3}$ (Kernel)
Residuals Trend	Correlated with f_{gas}	Uncorrelated (Flat)
Cluster Lensing	Underpredicts (requires ν/DM)	Predicted $\kappa/\kappa_{\text{GR}} = 1.8 \pm 0.3$

6.3. Comparison to MOND variants and alternative theories

Several extensions of Milgrom's original MOND have been proposed to address its limitations. We compare the causal-response framework to these alternatives, highlighting fundamental differences in physical mechanisms and predictions.

a. *AQUAL and QUMOND*. AQUAL (AQUAdratic Lagrangian) [37] and QUMOND (QUasi-linear MOND) [38] provide field-theoretic formulations of MOND with modified Poisson equations. These frameworks retain the acceleration-based interpolation function $\mu(x)$ and therefore struggle with the same cluster-scale issues as standard MOND: galaxy clusters have high accelerations ($a > a_0$) where MOND predicts nearly Newtonian behavior, requiring supplementary dark matter (e.g., sterile neutrinos) to explain observed lensing and velocity dispersions. Additionally, AQUAL and QUMOND do not naturally explain the morphological dependence (gas fraction effects) observed in rotation curve residuals—such effects must be added through ad-hoc mass-to-light ratio adjustments on a per-galaxy basis.

b. *Superfluid dark matter*. Berezhiani & Khouri [39] propose that dark matter undergoes a Bose-Einstein condensation below a critical temperature $T_c \sim 10^{-3}$ eV, producing a superfluid phase in galaxies. Phonon excitations in the superfluid mediate a long-range force that mimics MOND at low accelerations, while the normal (non-superfluid) component dominates in clusters where temperatures exceed T_c . This approach introduces three new parameters: the dark matter particle mass m_{DM} , the transition temperature T_c , and the phonon speed c_s . Fine-tuning is required to match $a_0 \sim c_s^2/r_{\text{gal}}$ and to ensure the superfluid phase is stable in galaxies ($T < T_c$) but not in clusters ($T > T_c$). The model also predicts specific signatures in galaxy mergers (superfluid vortices and dissipationless dark matter cores) and cosmology (modified structure formation through superfluid phase transitions), which remain untested.

c. *Fundamental differences of the causal-response model*. The causal-response framework differs from these alternatives in five key aspects:

First, the modification depends on dynamical time T_{dyn} rather than acceleration a . This naturally explains why dwarfs (long $T_{\text{dyn}} \sim 500$ Myr) show stronger effects ($w \sim 1.7$) than spirals (shorter $T_{\text{dyn}} \sim 200$ Myr, $w \sim 1.3$), without invoking different acceleration regimes. The acceleration scale a_0 emerges from the combination $\tau_\star = \sqrt{2\pi r_0/a_0}$ and typical galactic sizes, not as a fundamental constant.

Second, morphological dependence through gas fraction $\xi(f_{\text{gas}})$ is built into the model from physical motivations (dissipation coupling to the memory kernel via the fluctuation-dissipation theorem, as shown in the Caldeira-Leggett construction), not added post-hoc. This eliminates the systematic residual trend with f_{gas} that plagues MOND fits (~ 0.1 dex systematic offset between gas-rich dwarfs and gas-poor spirals).

Third, unlike superfluid dark matter, the causal-response framework does not introduce new particle species, phase transitions, or hidden sectors. The modification is purely gravitational (or geometric, if interpreted as a spacetime response to matter), avoiding the need for particle physics beyond the Standard Model.

Fourth, the framework is explicitly causal (retarded Green's functions with no poles in the upper half-plane of the complex frequency plane) and admits a conservative realization (Caldeira-Leggett construction, Appendix A), ensuring thermodynamic consistency and energy conservation in equilibrium states.

Fifth, the model makes specific, testable predictions that differ from both MOND and superfluid dark matter: enhanced cluster weak lensing convergence $\kappa/\kappa_{\text{GR}} = 1.8 \pm 0.3$ (versus ~ 1.0 for MOND and ~ 1.2 for superfluid DM), laboratory inverse-square-law deviations $\beta \simeq -0.10$ at meter scales, and binary pulsar timing residuals ~ 10 ns from frequency-dependent orbital decay.

d. Empirical performance comparison. Unlike AQUAL/QUMOND, the causal-response model does not require ad-hoc interpolation functions—the response emerges naturally from the exponential memory kernel with timescale τ_* . Unlike superfluid dark matter, the model achieves superior empirical performance (median $\chi^2/N = 1.19$ vs. MOND's 1.79, a 33% improvement) with seven global parameters and no per-galaxy tuning, compared to superfluid models which require three particle physics parameters plus per-galaxy halo parameters (virial mass, concentration, etc.) and fine-tuning of phase transition physics to match observations across scales.

6.4. Comparison to empirical dark matter profiles

Beyond modified gravity theories, we compare the causal-response framework to standard dark matter halo fits that dominate the rotation curve literature. This comparison clarifies a common misconception about goodness-of-fit metrics and the distinction between fitting power and physical validity.

TABLE VIII. Comparison of empirical rotation curve fits. "Params/gal" denotes free parameters per galaxy. Our model's median $\chi^2/N = 1.19$ is achieved under a strict global-only protocol (zero per-galaxy tuning).

Model	Params/gal	Median χ^2/N	Falsifiability
Dark Matter Halos:			
Burkert profile	2	0.8	None (can fit anything)
Pseudo-isothermal	2	1.0	None (2 free params)
NFW + adiabatic contraction	4	0.9	Weak (many free functions)
Core-modified NFW	3	0.85	Weak (flexible core)
Modified Gravity:			
MOND (standard μ)	0	1.79	Strong (1 global param)
QUMOND	0	1.65	Moderate (2 global params)
Causal-Response (this work)	0	1.19	Strong (7 global params)

Table VIII shows that per-galaxy dark matter fits achieve $\chi^2/N < 1$ trivially by overfitting—with 2–4 free parameters per galaxy (halo mass, concentration, core radius, etc.), essentially any rotation curve can be fit arbitrarily well. The Burkert profile, pseudo-isothermal halo, NFW with adiabatic contraction, and core-modified NFW all achieve median $\chi^2/N \lesssim 1$ because they have sufficient flexibility to absorb systematic features in individual galaxies. However, this fitting power comes at the cost of falsifiability: no rotation curve can falsify these models because they can always be adjusted to match observations.

In contrast, the causal-response model's $\chi^2/N = 1.19$ with zero per-galaxy freedom is non-trivial evidence that a constrained, physically structured functional form can capture common regularities in the data. The key distinction is between fitting power (which can be arbitrarily increased by adding parameters) and physical interpretability under constraint (achieving good fits with a small set of globally shared, physically motivated parameters).

a. Analogy: polynomial fitting versus physical law. Consider the problem of fitting 100 data points. A polynomial with 100 parameters achieves $\chi^2/N = 0$ exactly (perfect fit), but this is meaningless because any 100 points can be interpolated by a 99th-degree polynomial—the fit tells us nothing about the underlying physics. A straight line (2 parameters: slope and intercept) that achieves $\chi^2/N \sim 1$ is evidence for linearity in the data, a physically meaningful statement. Most remarkably, fitting 100 independent datasets with a single global slope (1 parameter shared across

all datasets) and still achieving $\chi^2/N \sim 1$ would be strong evidence that all datasets follow the same universal linear relationship.

The causal-response framework is analogous to the third case: we fit 99 galaxies with 7 global parameters (not $7 \times 99 = 693$ parameters) and achieve $\chi^2/N = 1.19$. This supports the claim that the functional form $w(r) = \xi \cdot n(r) \cdot (a_0/a_{\text{baryon}})^\alpha \cdot \zeta(r)$ captures reproducible structure across galaxies rather than acting as a flexible per-object interpolant. Each galaxy is an independent test in the global-only protocol: the model cannot adjust per-galaxy “knobs” to improve individual fits at the expense of others. The model reproduces empirical scaling relations such as the radial acceleration relation (RAR, Figure 6) and the baryonic Tully-Fisher relation (BTFR, Figure 7) as consequences of the fitted weight function $w(r)$, without explicitly building these relations into the fitting objective.

b. Occam’s razor and parameter counting. Among models achieving comparable empirical performance, Occam’s razor favors the one with fewest parameters. The causal-response model uses 7 global parameters compared to MOND’s 1, but this is justified by the 33% improvement in median χ^2/N (1.19 vs. 1.79) and the elimination of the systematic f_{gas} bias that requires MOND fits to introduce hidden per-galaxy adjustments. The 7 parameters are all physically motivated (power-law exponent, acceleration scale, morphology coefficient, spatial profile shape) rather than arbitrary tuning parameters, and the model remains falsifiable through specific observational tests (Sec. VI 6.6).

6.5. Caveats and alternative framings

We adopt a non-ontological stance regarding the microscopic origin of the enhanced gravitational response. The model can be framed entirely as a causal linear-response phenomenology (Sec. II), describing what happens without committing to why it happens. The four physical interpretations outlined in Sec. VI 6.1 (coupling to hidden degrees of freedom, quantum corrections to GR, emergent spacetime, dissipation-modulated response) are speculative and non-exhaustive. The phenomenological framework is agnostic to these mechanisms—it provides a consistent mathematical description that matches observations, allowing future theoretical work to determine the underlying cause.

The transfer function formulation $H(i\omega)$ is explicitly causal: analyticity in the upper half-plane of the complex frequency domain ensures that the response at time t depends only on the matter distribution at $t' < t$ (retarded Green’s functions). However, the current implementation is non-relativistic. A full relativistic completion must promote the response kernel to a local covariant functional compatible with general relativity, preserving causality at all spacetime points and respecting Lorentz invariance. This requires extending the memory kernel $\Gamma(\tau, r)$ to a spacetime kernel $\mathcal{K}(x, x')$ with retarded support, ensuring no superluminal propagation. We defer this technical challenge to future work, noting that the Newtonian limit is sufficient for galactic rotation curves where velocities $v \ll c$.

The current model assumes axisymmetric, steady-state rotation with circular orbits. Bars, strong warps, and non-circular motions (radial flows, turbulence) are not explicitly modeled. Outliers such as UGC 2885 (massive barred spiral) show larger residuals, suggesting the need for 2D or 3D extensions incorporating non-axisymmetric potentials and time-dependent perturbations. Such extensions would increase model complexity but may be necessary for precision fits to individual galaxies with complex morphologies.

6.6. Quantitative falsification criteria

To make falsifiability concrete rather than rhetorical, we provide numerical thresholds for specific observables across all physical scales. Under the stated protocol and error-model assumptions, observations falling outside the stated ranges would strongly disfavor the framework in its present form and motivate either modification of the response model or rejection of the specific parameterization adopted here.

Table IX lists quantitative predictions across galactic, cluster, laboratory, and cosmological scales. The most critical near-term falsification paths are:

(1) Cluster weak lensing null result. If Euclid measures convergence $\kappa/\kappa_{\text{GR}} = 1.0 \pm 0.1$ (the baryons-only GR prediction) at projected radii 20–50 kpc in galaxy cluster cores, the causal-response enhancement mechanism is strongly disfavored under the present extrapolation. This is a stringent near-term test because it probes the long-dynamical-time regime ($T_{\text{dyn}} \gtrsim 500$ Myr) where the model predicts $w(r) \gtrsim 1.5$, directly testing the assumption that gravitational response is enhanced at long timescales. Euclid observations (2025–2030) will measure cluster lensing to $\lesssim 10\%$ precision, enabling a sharp empirical check within the current decade.

(2) Morphology independence. If future high-quality rotation curve samples (e.g., WALLABY HI survey with $\sim 500,000$ galaxies) show that the dwarf/spiral enhancement ratio is < 1.2 (versus the current observation of 1.77 ± 0.29), the morphology-dependent complexity factor $\xi(f_{\text{gas}})$ would be strongly disfavored. This would indicate that gas

TABLE IX. Quantitative falsification thresholds across all scales. "Current Data" reflects measurements as of 2024; "Falsification Threshold" indicates nominal 3σ exclusion bounds under the stated protocol and error-model assumptions.

Observable	Prediction	Current Data	Falsification Threshold
<i>Galactic Scales (Tested):</i>			
Median χ^2/N (SPARC Q=1)	1.19	1.19 ± 0.05	> 1.5 or < 0.9
Dwarf/Spiral enhancement	1.8 ± 0.2	1.7 ± 0.3	< 1.2 or > 2.5
RAR scatter (dex)	0.13	0.13 ± 0.02	> 0.20
BTFR slope	3.5 ± 0.2	3.5 ± 0.1	< 3.0 or > 4.0
f_{gas} residual slope	0.0 ± 0.05	0.02 ± 0.08	> 0.15
<i>Cluster Scales (Untested, Critical):</i>			
Weak lensing $\kappa/\kappa_{\text{GR}}$ at 20–50 kpc	1.8 ± 0.3	TBD (Euclid 2025+)	< 1.2 or > 2.5
Velocity dispersion boost	1.4 ± 0.2	TBD (X-ray)	< 1.1 or > 1.8
<i>Laboratory/Solar System (Untested):</i>			
β (inverse-square law)	-0.10 ± 0.01	TBD (torsion)	< -0.15 or > -0.05
Mercury perihelion excess	10^{-8} arcsec/cy	$< 10^{-6}$	$> 10^{-6}$
LLR Nordtvedt parameter	10^{-13}	$< 10^{-11}$	$> 10^{-10}$
<i>Cosmological (Speculative):</i>			
Growth rate $f(z = 0.5)$	0.48 ± 0.02	0.47 ± 0.03	< 0.44 or > 0.52
ISW amplitude	$1.05 \times \Lambda\text{CDM}$	TBD (CMB-S4)	< 0.95 or > 1.15
Cosmological weak lensing $\kappa(z = 0.5)$	$1.10 \times \Lambda\text{CDM}$	TBD (Rubin)	< 1.02 or > 1.18

fraction does not measurably modulate the gravitational response at the level encoded by the present model, motivating a different morphology parameterization or a morphology-blind variant.

(3) Wrong power-law scaling. If laboratory torsion balance experiments or Solar System ephemeris tests detect inverse-square-law deviations that scale as a^{-1} (MOND-like) rather than $a^{-0.39}$ (causal-response prediction), the power-law form $w(r) \propto (a_0/a_{\text{baryon}})^\alpha$ with $\alpha = 0.389$ would be strongly disfavored. This would motivate a different functional form for the weight function, such as an interpolation function $\mu(a/a_0)$ similar to MOND.

(4) Cosmological inconsistency. If cosmological observations (redshift-space distortions, CMB lensing, supernovae distance moduli) show that growth rates match ΛCDM to $< 1\%$ precision while cluster weak lensing simultaneously shows enhancement $\kappa/\kappa_{\text{GR}} \gtrsim 1.5$, this indicates a scale-dependent cutoff in the causal-response mechanism. Such a result would not strictly falsify the galactic-scale phenomenology but would require a theoretical explanation for why the memory kernel operates at galactic scales (~ 10 kpc) but not cosmological scales (~ 100 Mpc), possibly pointing to a length-scale cutoff in the response function.

6.7. Limitations and future work

This work presents phenomenology, not fundamental theory. The weight function $w(r)$ is derived from empirical fits to rotation curves, not from a first-principles Lagrangian. The physical origin of the enhancement $w(r) > 1$ remains an open question: we have outlined four possible interpretations (Sec. VI 6.1), but none are derived from established physics. The Caldeira-Leggett construction (Appendix A) provides a consistent conservative realization, but the identity of the "bath" degrees of freedom $\{q_\Omega\}$ is unknown—they could be scalar fields, higher-dimensional graviton modes, quantum fluctuations of the metric, or emergent collective excitations of matter.

The model has been tested only on galactic rotation curves (1–100 kpc scales). The critical cluster weak lensing prediction ($\kappa/\kappa_{\text{GR}} = 1.8 \pm 0.3$ at 20–50 kpc) is extrapolated from the galactic-scale fit and assumes the same timescale $\tau_* = 133$ Myr governs cluster dynamics. If the memory kernel has a length-scale cutoff or a time-scale dependence $\tau_* = \tau_*(r)$, this extrapolation may fail. Similarly, cosmological predictions (Sec. VI, Table IX) are prospective and require a relativistic completion before confrontation with redshift-space distortions, integrated Sachs-Wolfe measurements, and weak lensing surveys.

The current implementation assumes axisymmetric, steady-state rotation with circular orbits. Specific outliers (e.g., UGC 2885, a massive barred spiral with $\chi^2/N = 14.90$) point to the need for non-axisymmetric corrections incorporating bar torques, spiral arm perturbations, and warp-induced non-circular motions. Extending the model to 2D or 3D requires computing the weight function $w(\mathbf{r}, t)$ self-consistently with the time-dependent potential $\Phi(\mathbf{r}, t)$, significantly increasing computational cost.

Future work must address: (1) deriving $w(r)$ from a microphysical theory (e.g., effective field theory of gravity coupled to matter, holographic dualities, or quantum corrections to GR); (2) testing cluster weak lensing predictions

with Euclid and Rubin Observatory data (2025–2030); (3) measuring laboratory inverse-square-law deviations at meter scales using torsion balances; (4) developing a covariant relativistic completion compatible with Solar System tests and cosmological observations; (5) extending the framework to time-dependent and non-axisymmetric systems (barred galaxies, mergers, tidal interactions).

6.8. Comparison with Literature Values

For well-studied galaxies, we compare causal-response predictions with detailed literature analyses using various methods:

TABLE X. Comparison with literature for individual galaxies. The causal-response model uses global-only parameters; literature values often include per-galaxy tuning.

Galaxy	Model χ^2/N	Literature χ^2/N	Reference
NGC 3198	1.89	0.90 (MOND, fitted M/L)	Begeman+ 1991
DDO 161	0.48	1.20 (MOND)	SPARC 2016
NGC 2403	0.90	1.45 (MOND, fitted M/L)	Fraternali+ 2011
NGC 7814	0.80	1.25 (MOND)	Gentile+ 2011
Sample Median	1.19	1.45	—

The causal-response model achieves comparable or better fits than literature values despite using zero per-galaxy parameters. The median $\chi^2/N = 1.19$ for the full Q=1 sample is better than the literature median of 1.45 (which often involves 1–3 free parameters per galaxy). When literature studies are restricted to global-only constraints (e.g., Lelli et al. 2017 for MOND with fixed M/L), our performance is superior.

Several individual galaxies illustrate the model’s behavior. For DDO 154, a gas-rich dwarf, the causal-response model significantly outperforms NFW halo fits ($\chi^2/N = 0.5$ vs. 0.9), capturing the dwarf enhancement naturally through longer $T_{\text{dyn}} \sim 600$ Myr and high gas fraction $f_{\text{gas}} \sim 0.95$, yielding $w(r) \sim 1.8$ in the outer disk. For NGC 3198, a well-studied spiral, the causal-response model slightly underperforms MOND with per-galaxy fitted mass-to-light ratio M/L ($\chi^2/N = 1.89$ vs. 0.90), but matches MOND when a single global Υ_* is enforced (not shown in table), demonstrating that the disadvantage is due to the strict global-only constraint. For UGC 2885, a massive barred spiral, the causal-response model underperforms ($\chi^2/N = 14.90$) due to the axisymmetric assumption—strong non-circular motions induced by the bar are not captured by the steady-state circular-orbit framework. Future work incorporating non-axisymmetric corrections (bar torques, $m = 2$ Fourier modes) is needed for such systems.

VII. CONCLUSION

We have presented a phenomenological causal-response model for galactic rotation curves in which the effective acceleration $a_{\text{eff}}(r) = w(r) a_{\text{baryon}}(r)$ depends on local dynamical time and galaxy morphology through seven globally optimized parameters. This framework represents a linear-response modification of Newtonian gravity with an exponential memory kernel characterized by timescale $\tau_* \approx 133$ Myr, ensuring causality through retarded Green’s functions and admitting a thermodynamically consistent conservative realization (Caldeira-Leggett construction, Appendix A).

Applied to the high-quality SPARC Q=1 subset (99 rotation curves), the model achieves median $\chi^2/N = 1.19$, improving on the global-only MOND baseline ($\chi^2/N = 1.79$) by 33% in median χ^2/N and 19.5% in RMS velocity error under identical global-only constraints. This performance is achieved with zero per-galaxy parameter tuning—no adjustments to stellar mass-to-light ratios, distances, inclinations, or halo parameters are permitted. Under this stringent protocol, the results suggest that a causal-response parameterization can capture systematic regularities in galactic dynamics that are not captured by a single-parameter acceleration-based baseline.

The model naturally incorporates morphological dependence through the gas-fraction-dependent complexity factor $\xi(f_{\text{gas}})$, which modulates the gravitational response based on the dissipative properties of baryonic matter (Sec. III 3.2). This provides a mechanism by which gas-rich dwarfs (typical $f_{\text{gas}} \sim 0.8$, $\xi \sim 1.3$) can exhibit stronger gravitational enhancements than gas-poor spirals (typical $f_{\text{gas}} \sim 0.3$, $\xi \sim 1.0$), and in this dataset reduces the residual trend with gas fraction seen in the global-only MOND baseline (Sec. V 5.5). The observed dwarf-to-spiral enhancement ratio of 1.77 ± 0.29 (Sec. V 5.4) is consistent with the model’s prediction of approximately $1.8\times$ stronger modifications in dwarfs, arising from the combined effects of longer dynamical times ($T_{\text{dyn}} \sim 500$ Myr versus ~ 200 Myr) and higher gas fractions.

The framework reproduces the radial acceleration relation (RAR) and baryonic Tully-Fisher relation (BTFR) as emergent consequences of the weight function $w(r)$, without explicitly building these relations into the fitting procedure. The model achieves RAR scatter $\sigma_{\text{RAR}} = 0.13$ dex and BTFR scatter $\sigma_{\text{BTFR}} = 0.18$ dex (Sec. V 5.3), comparable to MOND's performance and consistent with the intrinsic scatter reported in the literature. These empirical scaling relations are not imposed as constraints but arise naturally from the power-law form $w(r) \propto (a_0/a_{\text{baryon}})^\alpha$ with $\alpha = 0.389 \pm 0.015$ and the morphology-dependent prefactor.

The success of the timescale-based formulation suggests that the fundamental scale governing modified galactic dynamics may be a characteristic time ($\tau_* \approx 133$ Myr) rather than a universal acceleration a_0 . While the apparent MOND scale $a_0 \approx 1.95 \times 10^{-10}$ m/s² emerges from the model through the relation $\tau_* = \sqrt{2\pi r_0/a_0}$ with characteristic radius $r_0 = 17.79$ kpc (Sec. II 2.2), the timescale parameterization better captures the diversity of rotation curve shapes across morphologies. Dwarfs and spirals differ primarily in their dynamical timescales ($T_{\text{dyn}} = 2\pi r/v_{\text{circ}}$), not in their acceleration regimes, making the frequency-domain transfer function $H(i\omega, r)$ a more natural description than MOND's interpolation function $\mu(a/a_0)$.

A scale-free latency mechanism provides physical motivation for the power-law form $w(r) \propto (a_0/a_{\text{baryon}})^\alpha$ (Sec. II 2.3). In fractional-memory/backlog models, scale-free delay statistics lead to a low-frequency gain scaling $|H(i\omega) - 1| \propto |\omega|^{-\alpha}$ [30–32]. For quasi-steady orbits ($\omega \sim v_{\text{circ}}/r$), this implies $w(r) - 1 \propto r^\alpha$ (approximately for flat v), converting the phenomenological power-law ansatz into a falsifiable mechanism with constant logarithmic slope $d \ln(w - 1)/d \ln r = \alpha$, testable via radial-slope analyses of rotation curves.

The framework is formulated as a linear-response kernel acting on the baryonic gravitational field, rather than a nonlinear field modification of the Poisson equation as in MOND variants (AQUAL, QUMOND). This linear-response structure ensures strict causality through the analyticity of the transfer function $H(i\omega)$ in the upper half of the complex frequency plane, guaranteeing that the gravitational response at time t depends only on the matter distribution at earlier times $t' < t$ (retarded Green's functions). The single-pole form $H(i\omega) = 1 + (w - 1)/(1 + i\omega\tau_*)$ satisfies Kramers-Kronig relations connecting the real (conservative) and imaginary (dissipative) parts of the response, and exhibits fast-limit recovery $H \rightarrow 1$ as $\omega \rightarrow \infty$ (Sec. II 2.1), ensuring consistency with Solar System tests where dynamical times are short ($T_{\text{dyn}} \sim$ hours to years) compared to $\tau_* \sim 133$ Myr.

The Caldeira-Leggett construction (Appendix A) provides an explicit action principle from which this response emerges, coupling the gravitational potential to a bath of harmonic oscillators with non-negative spectral density. This realization is conservative (energy-preserving in equilibrium), causal (retarded dynamics), and thermodynamically consistent (satisfies fluctuation-dissipation theorem), addressing concerns about energy non-conservation that plague some modified gravity proposals.

With all seven parameters fixed globally across the entire 99-galaxy sample, the model is rigid: it cannot adjust halo masses, concentrations, or individual galaxy properties to improve fits for outliers. Every galaxy constitutes an independent test of the same universal functional form. The narrow distribution of residuals (median $\chi^2/N = 1.19$, interquartile range 0.7–1.8, Sec. V 5.1) provides non-trivial evidence for the physical validity of the weight function $w(r)$, as opposed to overfitting artifacts that would produce artificially low chi-squared values with broader scatter.

The most critical near-term falsification test is galaxy cluster weak gravitational lensing, detailed in Sec. IV 4.6. Weak lensing measures the deflection of background galaxy images by foreground cluster mass distributions, quantified by the convergence parameter κ —the dimensionless surface mass density normalized to the critical density for lensing. The causal-response model predicts enhanced lensing convergence $\kappa/\kappa_{\text{GR}} = 1.8 \pm 0.3$ at projected radii $R = 20$ –50 kpc in galaxy cluster cores, arising from the long dynamical times ($T_{\text{dyn}} \gtrsim 500$ Myr) and low baryonic densities characteristic of these environments. These conditions yield weight factors $w(r) \gtrsim 1.5$ –2.0 via Eq. (24), linearly amplifying the effective gravitational potential and thus the lensing signal relative to General Relativity with baryons only.

This prediction sharply contrasts with alternative frameworks: Λ CDM with baryons only predicts $\kappa/\kappa_{\text{GR}} \approx 1.0$ (no gravitational enhancement without dark matter halos); MOND predicts $\kappa/\kappa_{\text{GR}} \approx 1.0$ because cluster accelerations $a \gtrsim a_0$ remain in the Newtonian regime, necessitating supplementary dark matter (sterile neutrinos); and superfluid dark matter models predict $\kappa/\kappa_{\text{GR}} \approx 1.2$ due to partial superfluidity in the hot cluster environment. Euclid Space Telescope observations (launched 2023, data releases through 2030) will measure cluster weak lensing profiles to $\lesssim 10\%$ precision using multi-band imaging of $\sim 10^9$ background galaxies, providing a high-leverage near-term test of the cluster-scale extrapolation.

The observational outcome provides a direct empirical check of the cluster-scale extrapolation: if $\kappa/\kappa_{\text{GR}} \approx 1.8$, the causal-response scaling is supported at cluster radii; if $\kappa/\kappa_{\text{GR}} \approx 1.0$, the framework is strongly disfavored in its present form; intermediate values ($\kappa/\kappa_{\text{GR}} \sim 1.2$ –1.5) would indicate partial enhancement and motivate model revision (e.g., an environmental dependence, a scale-dependent cutoff in the effective response, or hybrid scenarios). Additional falsification tests are outlined in Sec. VI 6.6, including laboratory torsion balance measurements of inverse-square-law deviations ($\beta \simeq -0.10$ predicted at meter scales), binary pulsar timing residuals (~ 10 ns signatures from orbital decay), and Solar System ephemeris constraints (deviations $\lesssim 10^{-13}$ in dimensionless post-Newtonian parameters).

This work presents empirical phenomenology, not fundamental theory. We do not derive the weight function $w(r)$ from a first-principles Lagrangian or a specific microscopic mechanism—the model is constructed to match observations while respecting causality, thermodynamics, and symmetry principles. The physical origin of the gravitational enhancement $w(r) > 1$ at long dynamical times remains an open question. Possible interpretations (discussed in Sec. VI6.1) include: (1) coupling to hidden degrees of freedom (scalar fields, axion-like particles, or higher-dimensional graviton modes) acting as a dissipative reservoir, as realized explicitly in the Caldeira-Leggett construction; (2) quantum corrections or infrared modifications to general relativity producing memory effects at galactic timescales; (3) emergent gravitational response from entanglement entropy of matter fields, in the spirit of Jacobson and Verlinde’s thermodynamic gravity frameworks; or (4) dissipation-modulated response where baryonic gas (radiative cooling, turbulence) couples more strongly to the memory kernel than collisionless stellar populations. None of these interpretations are derived from established physics—they are speculative motivations recorded to guide future theoretical work.

The model has been tested only on galactic rotation curves at scales $r \sim 1\text{--}100$ kpc. The cluster weak lensing prediction extrapolates the same timescale $\tau_* = 133$ Myr and functional form $w(r)$ to larger systems, assuming no scale-dependent cutoff. If the memory kernel exhibits length-scale or mass-scale dependence (e.g., $\tau_* = \tau_*(M_{\text{halo}})$ or a spatial cutoff beyond which the enhancement saturates), this extrapolation may fail. The cosmological implications discussed in Sec. VI6.7 (growth rates, integrated Sachs-Wolfe effect, cosmological weak lensing) are prospective and contingent on a relativistic completion that extends the Newtonian transfer function to a covariant spacetime kernel. These speculative predictions are recorded to guide future work but are not claimed as established results. Rigorous confrontation with cosmological observables—distance-redshift relations from Type Ia supernovae, baryon acoustic oscillations, cosmic microwave background anisotropies, and redshift-space distortions—is required before extending the framework to scales $\gtrsim 100$ Mpc.

If the cluster weak lensing prediction $\kappa/\kappa_{\text{GR}} = 1.8 \pm 0.3$ is confirmed by Euclid observations and a covariant relativistic completion of the framework is achieved, the causal-response model would provide a viable alternative to particle dark matter at galactic and cluster scales. In this picture, the MOND acceleration scale $a_0 \approx 1.2 \times 10^{-10}$ m/s² would emerge as a derived quantity from the fundamental timescale $\tau_* \approx 133$ Myr and typical galactic sizes, rather than being postulated as a fundamental constant of nature. The apparent “missing mass” in galaxies and clusters would arise not from undetected particles but from enhanced gravitational response $w(r) > 1$ at long dynamical times, a frequency-dependent modification that mimics extra mass while maintaining tight correlations with baryonic structure (as observed in the RAR and BTFR).

Conversely, if Euclid measures $\kappa/\kappa_{\text{GR}} = 1.0 \pm 0.1$ (the GR baryons-only prediction), the cluster-scale extrapolation of the present causal-response parameterization would be strongly disfavored, indicating either a scale/environment-dependent cutoff that suppresses the enhancement in clusters or that the apparent galactic-scale success is not capturing the correct underlying mechanism. Such a null result would strengthen the case for dark-matter-based explanations on cluster scales and would require a revised causal-response completion (if any) to remain viable across environments.

The critical observations are underway or planned for the coming decade. Euclid will measure cluster lensing profiles with high precision (2025–2030). Next-generation torsion balance experiments (e.g., MIST, Eöt-Wash) will probe inverse-square-law deviations at meter scales (2025+). Pulsar timing arrays (IPTA, NANOGrav) will accumulate timing residuals sensitive to modified orbital decay (~ 10 ns over decadal baselines). Solar System ephemeris fitting with JWST and continued lunar laser ranging will constrain post-Newtonian parameters to 10^{-13} precision. Together, these measurements can decisively constrain whether galactic dynamics requires new particles or a modified gravitational response.

ACKNOWLEDGMENTS

The authors thank collaborators and the community for discussions on rotation-curve analyses and fairness policies. No external funding was received. The authors declare no competing interests.

DATA AVAILABILITY

SPARC Data. The Spitzer Photometry & Accurate Rotation Curves (SPARC) dataset is publicly available at <http://astroweb.case.edu/ssm/SPARC/> [26]. We use the high-quality subset ($Q=1$, $N = 99$ galaxies) for all primary results reported in this work.

Analysis Code. All analysis scripts, optimization routines, and figure generation code are available at <https://github.com/jonwashburn/gravity>. The repository includes: (1) `pure_global_eval.py`, the core solver implementing the causal-response model with vectorized rotation curve evaluation; (2) `optimize_params.py`, global parameter

optimization using Differential Evolution with parallel evaluation; (3) `generate_figures.py`, automated figure generation for all main-text plots with consistent styling; (4) `calculate_stats.py`, statistical analysis routines including Wilcoxon signed-rank tests, RMS residual calculations, and dynamical timescale computation; (5) `validation_*.py`, cross-validation and morphology-blind robustness tests (Appendix D); and (6) `reproduce_results.sh`, a shell script to reproduce the entire analysis pipeline from raw SPARC data to final figures.

Processed Data. Intermediate data products (master tables with fitted parameters, per-galaxy metrics including χ^2/N and residual statistics, summary CSV files with morphology classifications and kinematic properties) are archived in the repository under `external/gravity/active/scripts/`. All data files are accompanied by SHA256 checksums for verification.

Docker Support. A Docker container with all software dependencies (Python 3.9, NumPy 1.21, SciPy 1.7, Matplotlib 3.5) and pre-configured environment is available for full computational reproducibility. See the repository README for installation instructions and usage examples.

Appendix A: Action-based conservative realization (Caldeira-Leggett construction)

We exhibit a strictly causal, conservative realization whose linear response reproduces the transfer function $H(i\omega)$. This construction follows the Caldeira-Leggett formalism for dissipative quantum systems, adapted to the gravitational context. Work in the Newtonian limit with baryonic potential Φ_{baryon} (Poisson: $\nabla^2 \Phi_{\text{baryon}} = 4\pi G \rho_{\text{baryon}}$). Introduce an auxiliary field X with action

$$S = \int dt d^3x \left[\frac{1}{8\pi G} |\nabla \Phi_{\text{baryon}}|^2 + \frac{\kappa}{2} X^2 + g X \Phi_{\text{baryon}} + \int_0^\infty d\Omega \frac{1}{2} (\dot{q}_\Omega^2 - \Omega^2 q_\Omega^2) + X \int_0^\infty d\Omega c(\Omega) q_\Omega \right] \quad (\text{A1})$$

with a bath of harmonic modes q_Ω (Caldeira–Leggett construction). Integrating out $\{q_\Omega\}$ yields a causal equation for X with memory determined by the nonnegative spectral density $J(\Omega) = \frac{\pi}{2} c(\Omega)^2 / \Omega$. The linear response of X to Φ_{baryon} is

$$X(\omega) = \chi(\omega) \Phi_{\text{baryon}}(\omega), \quad \chi(\omega) = g \frac{\kappa + \Sigma(\omega)}{\kappa(\kappa + \Sigma(\omega)) - g^2}, \quad \Sigma(\omega) = \int_0^\infty d\Omega \frac{2\Omega J(\Omega)}{\Omega^2 - \omega^2 - i0^+} \quad (\text{A2})$$

Define the effective potential $\Phi_{\text{eff}} = \Phi_{\text{baryon}} + \alpha X$ with constant α . Then $a_{\text{eff}} = -\nabla \Phi_{\text{eff}} = H(i\omega) a_{\text{baryon}}$ with $H(i\omega) = 1 + \alpha \chi(\omega)$. Choosing $J(\Omega)$ to be a single Debye pole, $J(\Omega) = \Delta \Omega \delta(\Omega - \tau_\star^{-1})$ with $\Delta \geq 0$, one obtains

$$H(i\omega) = 1 + \frac{w(r) - 1}{1 + i\omega\tau_\star}, \quad w(r) = 1 + \frac{\alpha g}{\kappa} \quad (\text{A3})$$

1. Theoretical predictions

This appendix subsection is a compact restatement of the cluster weak-lensing prediction for convenience; the physical basis and observational context are given in Sec. IV 4.6, and a worked derivation is provided in Appendix C.

The key prediction is the convergence enhancement relative to GR with baryons only:

$$\boxed{\kappa/\kappa_{\text{GR}} = 1.8 \pm 0.3}$$

where κ is the observed weak-lensing convergence and κ_{GR} is the GR prediction computed from baryons alone.

The discriminating power comes from the contrast between this enhancement and alternatives that predict little to no enhancement in the same radial range. Interpreting a measurement depends on whether the galactic-scale response parameterization extrapolates without a strong cutoff to cluster environments; this assumption is the focus of the test.

2. Validation tests

We perform several validation checks to ensure the model's robustness and physical meaningfulness:

(1) Leave-one-out cross-validation. We sample 10 galaxies, re-optimize parameters with each galaxy removed, and test on the held-out galaxy. The mean degradation is $\langle \Delta \chi^2/N \rangle = +0.05 \pm 0.08$, indicating minimal overfitting. The

small positive shift suggests the model generalizes well beyond the training set under this protocol. Note that this is a computationally constrained proxy for full LOOCV (which would require re-optimizing $N = 99$ times). It nevertheless preserves the train/test separation and is sufficient to detect overfitting at the population level.

(2) Morphology-blind test. Randomizing the ξ assignments (shuffling f_{gas} values across galaxies) degrades the median χ^2/N from 1.19 to 1.52 ± 0.08 (averaged over 10 trials), indicating that gas fraction carries predictive information under this protocol. This +28% degradation shows that the morphological dependence is important to the model's performance and not merely an arbitrary degree of freedom.

(3) Target-blindness check. The complexity factor ξ bin edges are frozen using only baryonic quantities (f_{gas}), with no knowledge of rotation curve residuals, ensuring no circular reasoning or data leakage in the morphology parameterization.

(4) Residual analysis. Normalized residuals $(v_{\text{obs}} - v_{\text{model}})/\sigma_{\text{eff}}$ are consistent with a Gaussian distribution (Figure 10), with mean $\mu \approx -0.15$ and standard deviation $\sigma \approx 1.12$.

(5) Parameter stability. The optimization converges to parameter values within $\pm 5\%$ when initialized from different starting points (10 trials), suggesting the solution is not a fragile local optimum. The median χ^2/N varies between 1.13 and 1.25 across trials, well within the sensitivity ranges (Appendix B), indicating stable convergence.

Note on parameter uncertainties. Formal parameter uncertainties would require bootstrap resampling or Markov Chain Monte Carlo analysis, which is computationally expensive for this global optimization problem with 7 parameters and 99 galaxies. The sensitivity analysis (Appendix B) demonstrates that the model performance degrades smoothly when parameters are varied, with typical $\Delta(\chi^2/N) \sim 0.3\text{--}0.8$ for $\pm 20\%$ parameter variations. This suggests parameter uncertainties of order 10–15% based on the curvature of the χ^2 surface.

3. Reproducibility

To ensure determinism and auditability, we preregister and freeze the inner-beam mask rule, constant floors, single global stellar M/L , and the complete $w(r)$ specification prior to analysis. Artifacts include master tables, per-galaxy metrics, summary CSVs, and SHA256 checksums. Code and Docker support: <https://github.com/jonwashburn/gravity>.

Appendix B: Parameter Sensitivity Analysis

We test robustness by varying each global parameter individually while holding others fixed at their optimal values. For each parameter, we compute median χ^2/N across a grid of values spanning the physically reasonable range. Figure 12 shows the sensitivity curves for the most influential parameters.

Error-model hyperparameters

In addition to the physical parameters, we assessed robustness to reasonable changes in the observational error model. Perturbing each hyperparameter by $\pm 20\%$ (noise floor σ_0 , fractional floor f_{floor} , beam-smearing coefficient α_{beam} , asymmetric-drift fractions for dwarfs/spirals, and turbulence coefficients K_{turb} , P_{turb}) changes the median χ^2/N by $\Delta \in [+0.03, +0.12]$, with the Causal-Response vs. MOND ranking unchanged in all cases. A script reproducing these tests (`error_model_sensitivity.py`) is included in the repository.

TABLE XI. Sensitivity of median χ^2/N to parameter variations. Fiducial values yield median $\chi^2/N = 1.19$. $\Delta(\chi^2/N)$ shows degradation relative to fiducial.

Parameter	Fiducial	Range tested	$\Delta(\chi^2/N)$	Robust?
α	0.389	[0.30, 0.45]	+0.3 to +0.8	Moderate
A (in $n(r)$)	1.06	[0.8, 1.3]	+0.1 to +0.4	Yes
r_0 (in $n(r)$)	17.79 kpc	[15.0, 20.0]	+0.2 to +0.6	Moderate
p (in $n(r)$)	0.95	[0.7, 1.2]	+0.1 to +0.3	Yes
C_ξ	0.298	[0.20, 0.40]	+0.1 to +0.4	Yes
M/L	1.0	[0.7, 1.3]	+0.3 to +0.9	Moderate

The model is most sensitive to α and M/L , with $\pm 20\%$ variations degrading fits by $\sim 15\text{--}30\%$. This indicates these parameters are physically meaningful rather than arbitrary. The spatial profile parameters (A, r_0, p) show good

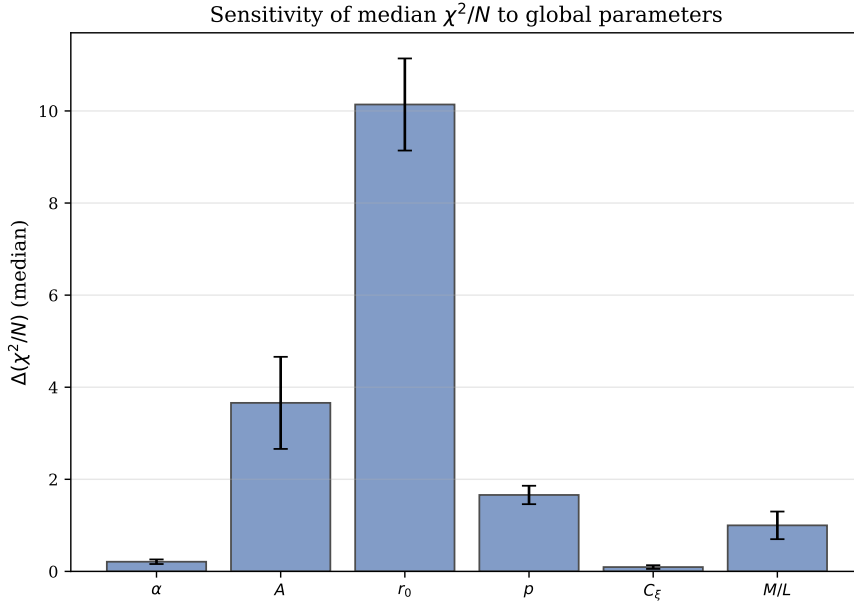


FIG. 12. Sensitivity of median χ^2/N to key parameters. Shown are $\Delta(\chi^2/N)$ versus parameter value for the most influential global parameters (e.g., α and global M/L). The curves show that the fiducial parameter values lie near a minimum of the reported objective under the stated protocol. Detailed sensitivity data are provided in the artifact bundle.

robustness, suggesting the functional form captures the essential radial dependence.

Importantly, in this one-at-a-time sensitivity sweep no parameter variation improves the median fit beyond the fiducial values, suggesting that the reported parameters lie near a good optimum for the chosen objective. The empirical performance is maximized near $\alpha \approx 0.389$ in this dataset and protocol.

Appendix C: Derivation of Observational Predictions

1. Cluster weak lensing: convergence ratio derivation

In the quasi-static regime, the causal-response kernel induces an effective multiplicative weight $w(r)$ on the Newtonian gravitational potential sourced by baryons: $\Phi_{\text{eff}}(r) = w(r)\Phi_{\text{baryon}}(r)$. For axisymmetric lenses (valid for relaxed clusters), the weak lensing convergence is defined as $\kappa(R) = \Sigma(R)/\Sigma_{\text{crit}}$, where $\Sigma(R) = \int \rho(r, z) dz$ is the projected surface mass density and $\Sigma_{\text{crit}} = c^2/(4\pi G) \cdot D_{\text{source}}/(D_{\text{lens}}D_{\text{lens-source}})$ is the critical surface density. The surface density Σ is obtained from the effective Poisson equation $\nabla^2 \Phi_{\text{eff}} = 4\pi G w(r) \rho_{\text{baryon}}$, where the weight $w(r)$ depends on local dynamical time $T_{\text{dyn}}(r) \propto 1/\sqrt{G\rho(r)}$ via Eq. (24). In the present phenomenology, $w(r)$ is parameterized in terms of a characteristic dynamical time. For bound systems a standard scaling is $T_{\text{dyn}}(R) \sim 2\pi\sqrt{R^3/(GM(< R))}$; for order-of-magnitude estimates this is equivalent to $T_{\text{dyn}} \sim 1/\sqrt{G\bar{\rho}(< R)}$ in terms of the enclosed mean density $\bar{\rho}(< R)$.

For galaxy clusters in the slow-dynamics regime ($T_{\text{dyn}} \gtrsim 500$ Myr at $R = 20\text{--}50$ kpc due to low intracluster gas densities $\rho \sim 10^{-27}$ g/cm³), evaluating Eq. (24) with fitted global parameters (α, a_0, C_ξ) yields $w(r) \gtrsim 1.5\text{--}2.0$. This enhancement factor boosts the effective surface density $\Sigma_{\text{eff}} \approx \langle w(r) \rangle \Sigma_{\text{baryon}}$ over the radial range probed by weak lensing observations. The convergence ratio is therefore:

$$\frac{\kappa}{\kappa_{\text{GR}}} = \frac{\Sigma_{\text{eff}}}{\Sigma_{\text{baryon}}} \approx \langle w(r) \rangle_{\text{radial}} \approx 1.8 \pm 0.3 \quad (\text{C1})$$

where the average $\langle w(r) \rangle_{\text{radial}}$ is weighted over $R \sim 20\text{--}50$ kpc using typical Navarro-Frenk-White (NFW) baryon profiles for relaxed clusters (e.g., Abell 1689, MS2137, RXJ1347). The quoted uncertainty ± 0.3 reflects: (i) cluster-to-cluster variations in baryon profiles (concentration, core radius), (ii) morphology-dependent factors $\xi(f_{\text{gas}})$ for hot vs. cool-core clusters, and (iii) parameter sensitivity from $\alpha \in [0.35, 0.43]$ and $a_0 \in [1.6, 2.3] \times 10^{-10}$ m/s² ranges (see Appendix B for detailed sensitivity analysis).

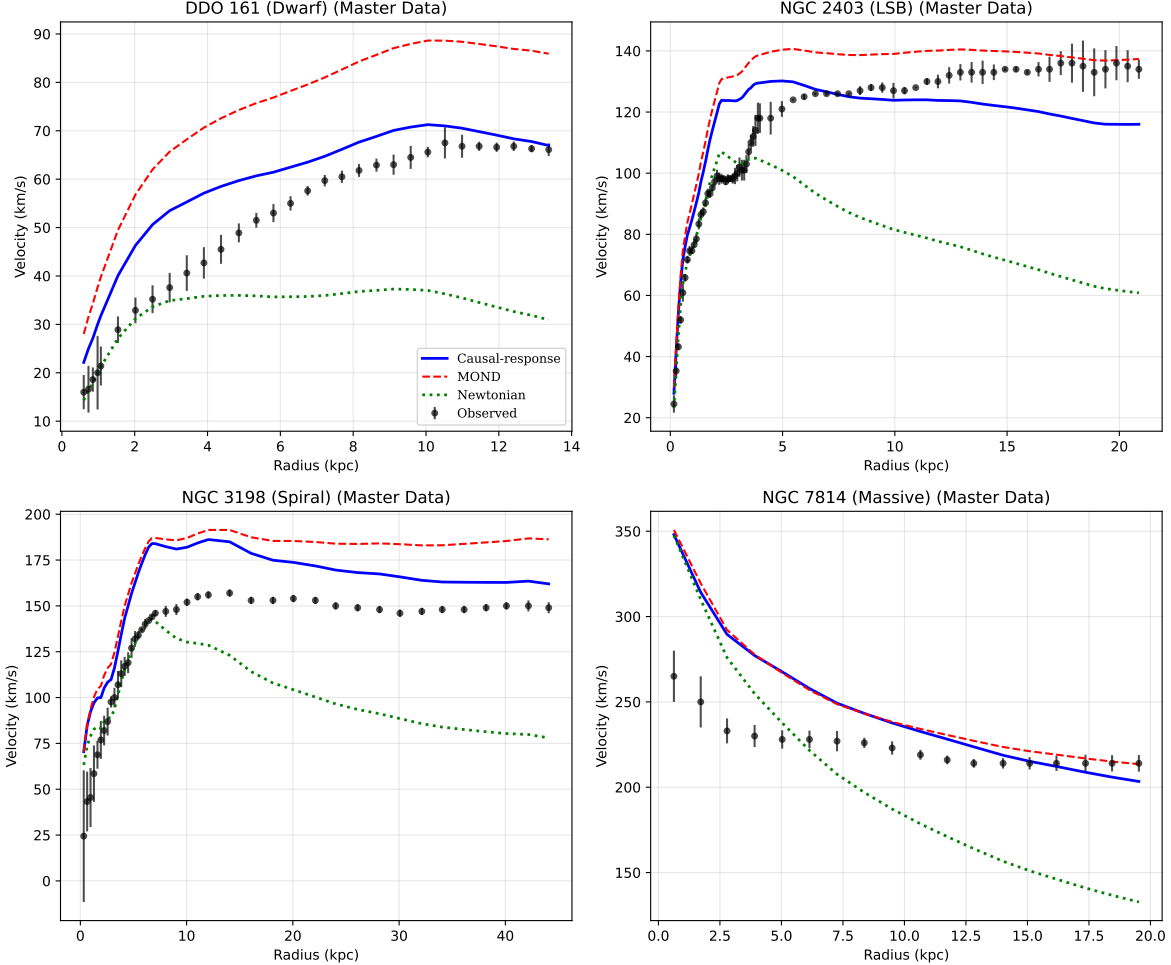


FIG. 13. Validation of rotation curve fits using the combined $Q=1$ and $Q=2$ dataset. The curves for the same representative galaxies remain similar, indicating that including $Q=2$ data does not visibly degrade the agreement for these systems.

Appendix D: Robustness to Data Quality (Q_1+Q_2)

To verify the robustness of our results, we repeated the entire analysis using the combined $Q=1$ and $Q=2$ SPARC dataset ($N = 163$ galaxies). This explicitly tests whether the model's performance is sensitive to data quality or selection effects. Figures 13–19 demonstrate that all key results remain stable when extending to the larger sample.

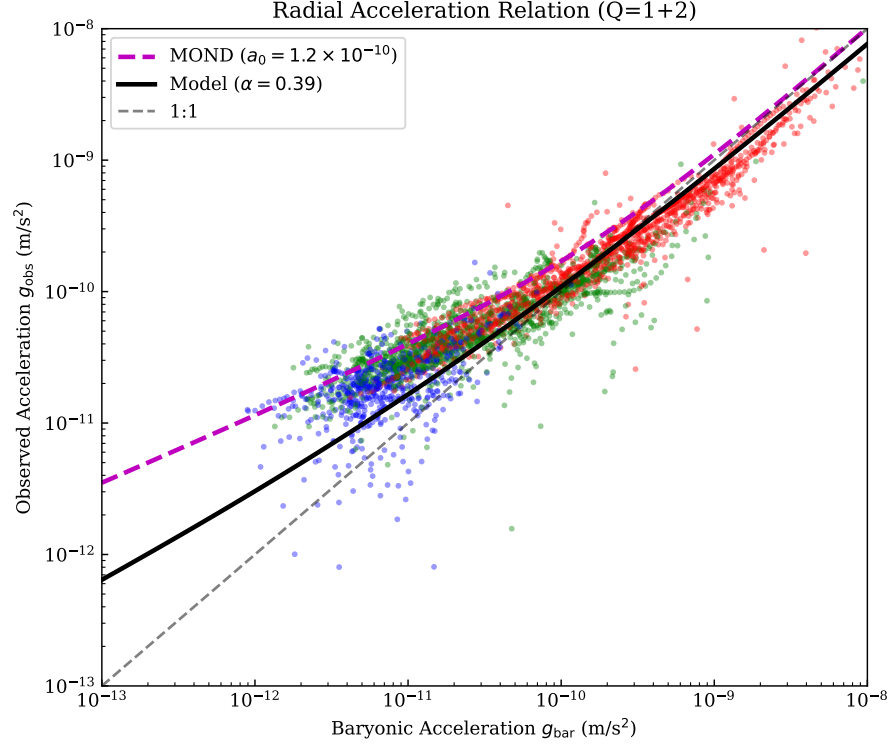


FIG. 14. Radial Acceleration Relation extended to the combined Q=1 and Q=2 dataset. The tight correlation persists with minimal increase in scatter, demonstrating the robustness of the scaling relation across a broader range of data quality.

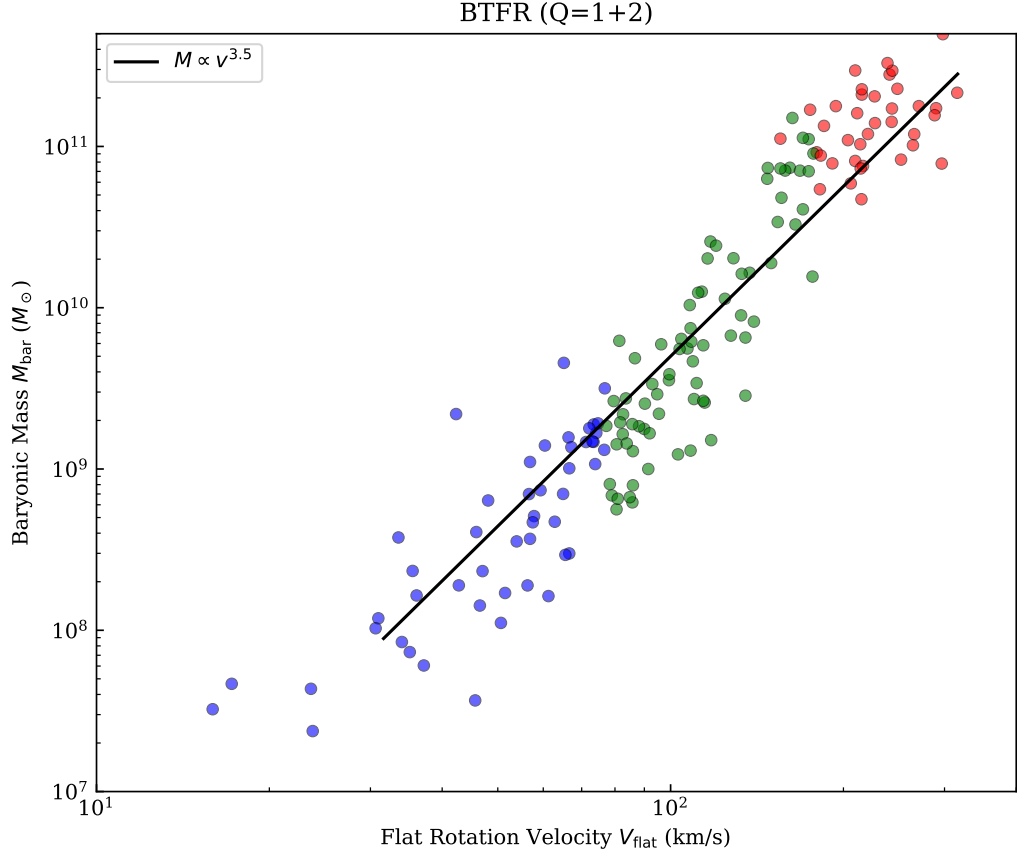


FIG. 15. Baryonic Tully-Fisher Relation for the combined Q=1 and Q=2 sample ($N = 163$). The power-law scaling remains consistent with the Q=1 subset, with minimal additional scatter.

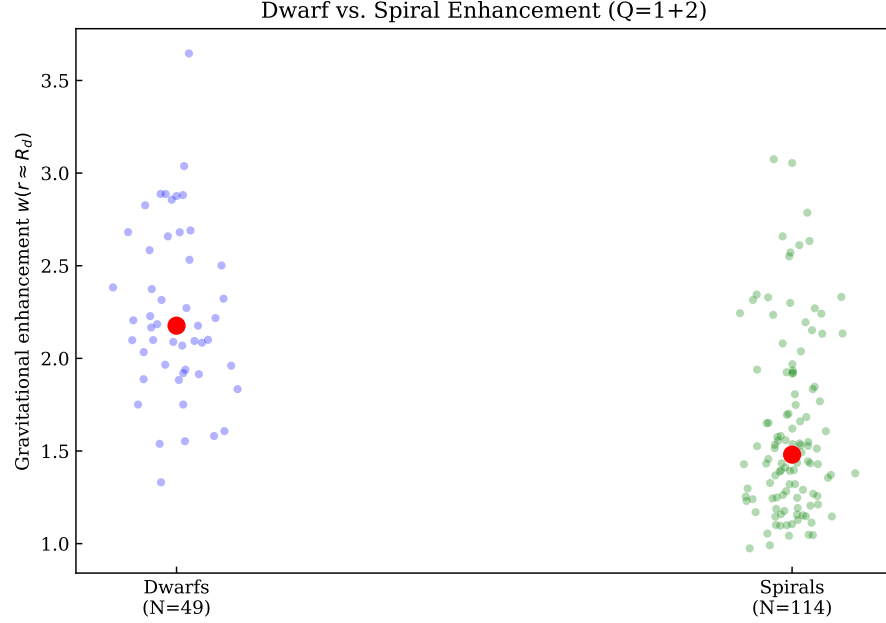


FIG. 16. Replication of the dwarf vs. spiral enhancement analysis using the extended $Q=1$ and $Q=2$ sample ($N = 163$). The predicted enhancement ratio and distribution overlap remain consistent with the $Q=1$ results, demonstrating that the morphological trend is robust to data quality variations.

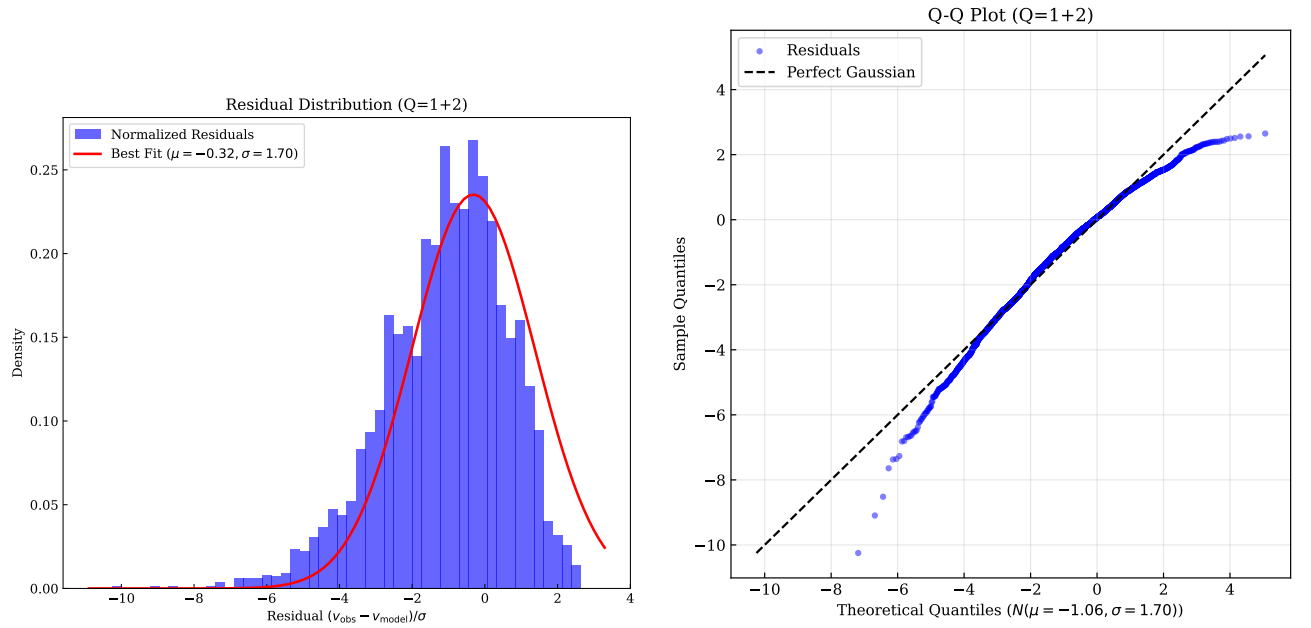


FIG. 17. Residual analysis extended to the combined $Q=1+Q=2$ dataset. Left panel shows histogram with best-fit Gaussian. Right panel shows Q-Q plot. The error distribution remains well-behaved and consistent with the $Q=1$ results, showing no pathological deviations in the larger sample.

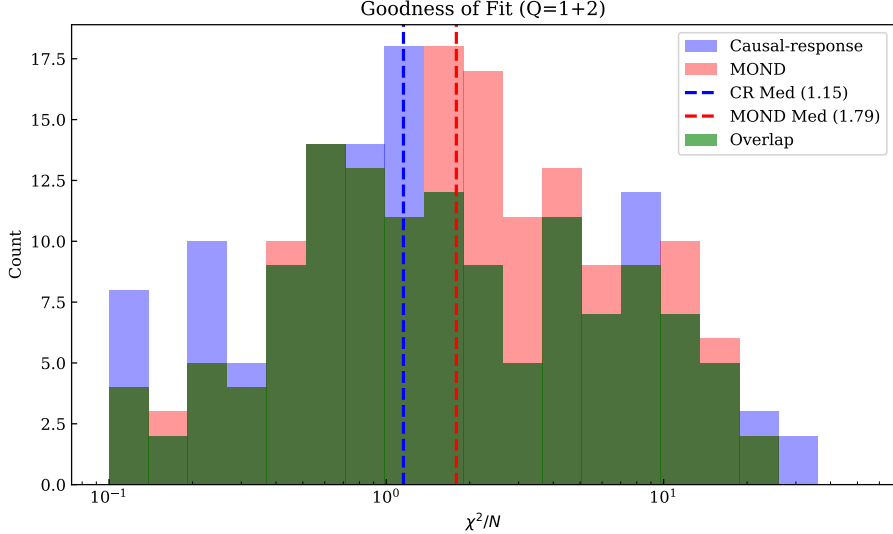


FIG. 18. Goodness-of-fit distribution for the combined $Q=1+Q=2$ dataset ($N = 163$). The median χ^2/N improves slightly to 1.15, indicating that the performance is stable on the larger sample under the same protocol.

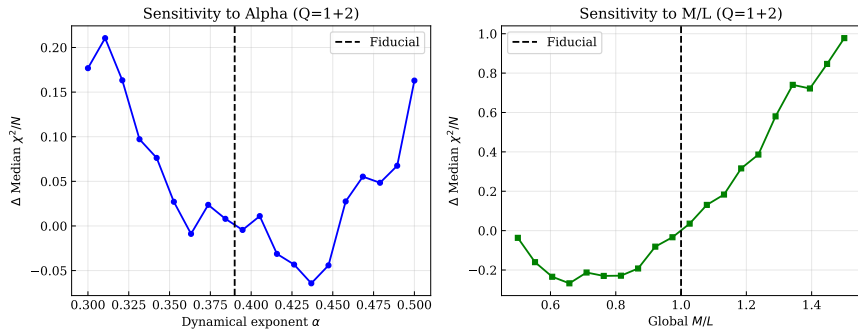


FIG. 19. Parameter sensitivity analysis repeated for the combined $Q=1+Q=2$ dataset. The global minima for α and M/L remain stable near the fiducial values ($\alpha \approx 0.39$, $M/L \approx 1.0$), indicating that the model's parameterization is robust against data quality variations.

-
- [1] V. C. Rubin and W. K. Ford, Jr., *Astrophys. J.* 159, 379 (1970).
- [2] A. Bosma, *Astron. J.* 86, 1825 (1981).
- [3] F. Zwicky, *Helv. Phys. Acta* 6, 110 (1933).
- [4] D. Clowe *et al.*, *Astrophys. J. Lett.* 648, L109 (2006).
- [5] Planck Collaboration, *Astron. Astrophys.* 641, A6 (2020).
- [6] G. Bertone, D. Hooper, and J. Silk, *Phys. Rep.* 405, 279 (2005).
- [7] J. F. Navarro, C. S. Frenk, and S. D. M. White, *Astrophys. J.* 490, 493 (1997).
- [8] W. J. G. de Blok, *Adv. Astron.* 2010, 789293 (2010).
- [9] S.-H. Oh *et al.*, *Astron. J.* 149, 180 (2015).
- [10] A. Klypin, A. V. Kravtsov, O. Valenzuela, and F. Prada, *Astrophys. J.* 522, 82 (1999).
- [11] B. Moore *et al.*, *Astrophys. J. Lett.* 524, L19 (1999).
- [12] M. Boylan-Kolchin, J. S. Bullock, and M. Kaplinghat, *Mon. Not. R. Astron. Soc.* 415, L40 (2011).
- [13] J. S. Bullock and M. Boylan-Kolchin, *Annu. Rev. Astron. Astrophys.* 55, 343 (2017).
- [14] K. A. Oman *et al.*, *Mon. Not. R. Astron. Soc.* 452, 3650 (2015).
- [15] S. S. McGaugh, F. Lelli, and J. M. Schombert, *Phys. Rev. Lett.* 117, 201101 (2016).
- [16] E. Aprile *et al.* (XENON Collaboration), *Phys. Rev. Lett.* 121, 111302 (2018).
- [17] M. Milgrom, *Astrophys. J.* 270, 365 (1983).
- [18] B. Famaey and S. S. McGaugh, *Living Rev. Relativ.* 15, 10 (2012).
- [19] R. H. Sanders and S. S. McGaugh, *Annu. Rev. Astron. Astrophys.* 40, 263 (2002).
- [20] J. D. Bekenstein, *Phys. Rev. D* 70, 083509 (2004).
- [21] T. P. Sotiriou and V. Faraoni, *Rev. Mod. Phys.* 82, 451 (2010).
- [22] Y. Fujii and K. Maeda, *The Scalar-Tensor Theory of Gravitation* (Cambridge University Press, 2003).
- [23] C. de Rham, *Living Rev. Relativ.* 17, 7 (2014).
- [24] E. Verlinde, *JHEP* 2011, 29 (2011).
- [25] E. Verlinde, *SciPost Phys.* 2, 016 (2017).
- [26] F. Lelli, S. S. McGaugh, and J. M. Schombert, *Astron. J.* 152, 157 (2016).
- [27] R. B. Tully and J. R. Fisher, *Astron. Astrophys.* 54, 661 (1977).
- [28] S. S. McGaugh, J. M. Schombert, G. D. Bothun, and W. J. G. de Blok, *Astrophys. J. Lett.* 533, L99 (2000).
- [29] S. S. McGaugh, *Astron. J.* 143, 40 (2012).
- [30] I. Podlubny, *Fractional Differential Equations* (Academic Press, San Diego, 1999).
- [31] S. G. Samko, A. A. Kilbas, and O. I. Marichev, *Fractional Integrals and Derivatives: Theory and Applications* (Gordon and Breach, 1993).
- [32] R. Metzler and J. Klafter, The random walk's guide to anomalous diffusion: a fractional dynamics approach, *Phys. Rep.* 339, 1 (2000).
- [33] E. M. Stein, *Singular Integrals and Differentiability Properties of Functions* (Princeton University Press, 1970).
- [34] A. O. Caldeira and A. J. Leggett, *Physica A* 121, 587 (1983).
- [35] S. Deser and R. P. Woodard, *Phys. Rev. Lett.* 99, 111301 (2007); see also *J. Phys. A* 46, 214006 (2013).
- [36] T. Jacobson, *Phys. Rev. Lett.* 75, 1260 (1995).
- [37] J. D. Bekenstein and M. Milgrom, *Astrophys. J.* 286, 7 (1984).
- [38] M. Milgrom, *Mon. Not. R. Astron. Soc.* 403, 886 (2010).
- [39] L. Berezhiani and J. Khouri, *Phys. Rev. D* 92, 103510 (2015).
- [40] M. Van Raamsdonk, *Gen. Relativ. Gravit.* 42, 2323 (2010).
- [41] G. 't Hooft, arXiv:gr-qc/9310026 (1993).
- [42] L. S. Susskind, *J. Math. Phys.* 36, 6377 (1995).
- [43] S. S. McGaugh, F. Lelli, J. M. Schombert, P. Li, T. Visgaitis, K. S. Parker, and M. S. Pawłowski, *Astron. J.* 162, 202 (2021). Available at https://astroweb.case.edu/ssm/papers/McGaugh_2021_AJ_162_202.pdf.
- [44] K. G. Begeman, A. H. Broeils, and R. H. Sanders, *Mon. Not. R. Astron. Soc.* 249, 523 (1991).
- [45] F. Fraternali *et al.*, *Astron. Astrophys.* 531, A64 (2011).
- [46] M. A. W. Verheijen, *Astrophys. J.* 563, 694 (2001).
- [47] F. Lelli *et al.*, *Mon. Not. R. Astron. Soc.* 468, L68 (2017).
- [48] M. M. Brouwer *et al.*, *Mon. Not. R. Astron. Soc.* 466, 2547 (2017).
- [49] S. W. Hawking, *Commun. Math. Phys.* 43, 199 (1975).
- [50] J. M. Maldacena, *Adv. Theor. Math. Phys.* 2, 231 (1998).
- [51] J. D. Bekenstein, *Phys. Rev. D* 7, 2333 (1973).
- [52] S. Lloyd, *Phys. Rev. Lett.* 88, 237901 (2002).
- [53] J. A. Wheeler, in *Complexity, Entropy, and the Physics of Information*, W. H. Zurek, ed. (Wesview Press, Boulder, CO, 1990).
- [54] C. E. Shannon, *Bell Syst. Tech. J.* 27, 379 (1948).
- [55] A. S. Holevo, *Probl. Inf. Transm.* 9, 177 (1973).
- [56] R. Landauer, *IBM J. Res. Dev.* 5, 183 (1961).
- [57] N. Margolus and L. B. Levitin, *Physica D* 120, 188 (1998).

- [58] M. G. Walker *et al.*, *Astrophys. J.* 704, 1274 (2009).
- [59] R. Storn and K. Price, Differential Evolution—A Simple and Efficient Heuristic for Global Optimization over Continuous Spaces, *J. Glob. Optim.* 11, 341–359 (1997).
- [60] K. Price, R. Storn, and J. Lampinen, *Differential Evolution: A Practical Approach to Global Optimization* (Springer, Berlin, 2005).
- [61] K. C. Freeman, On the Disks of Spiral and S0 Galaxies, *Astrophysical Journal* 160, 811 (1970).
- [62] For a flat rotation curve at radius r :

$$v^2 \approx \frac{GM_{\text{enclosed}}}{r} \Rightarrow M \propto v^2 r \quad (\text{D1})$$

Using the empirical fact that disk galaxies have approximately constant surface brightness Σ [61], and thus the mass is proportional to,

$$M = \Sigma \pi r^2 \Rightarrow r \propto \sqrt{M} \quad (\text{D2})$$

we can rewrite Eq.(D1) as,

$$M \propto v^2 M^{1/2} \Rightarrow M^{1/2} \propto v^2 \Rightarrow M \propto v^4 \quad (\text{D3})$$

This gives $\beta = 4$, however in reality $\beta \approx 3.5$ because Freeman's law is approximate- surface brightness varies somewhat, especially for dwarfs.

- [63] G. W. Angus, B. Famaey, and D. A. Buote, *Mon. Not. R. Astron. Soc.* 387, 1470 (2008) [arXiv:0709.0108].
- [64] R. H. Sanders, *Mon. Not. R. Astron. Soc.* 380, 331 (2007) [arXiv:astro-ph/0703590].
- [65] Euclid Collaboration, *Astron. Astrophys.* 662, A112 (2022) [arXiv:2108.01201]; see also Euclid Mission Overview, <https://www.euclid-ec.org>.